DISS. ETH NO. 22302

MRI USING FIELD DYNAMICS FOR POSITION SENSING AND MOTION CORRECTION

A thesis submitted to attain the degree of

DOCTOR OF SCIENCES of ETH ZURICH

(Dr. sc. ETH Zurich)

presented by

Maximilian Rudolf Gottfried Häberlin (MSc. ITET ETH, ETH Zurich)

born on 05.04.1983

citizen of Amriswil TG and Hefenhofen TG

accepted on the recommendation of

Prof. Dr. Klaas P. Pruessmann, ETH Zurich

Prof. Dr. Oliver Speck, Otto-von-Guericke University Magdeburg

2014

Table of Contents

Abstract

Magnetic resonance imaging (MRI) relies on the superposition of dynamic magnetic gradient fields onto a static, spatially homogeneous background field in order to spatially resolve image information. Image encoding is achieved by gradient coil dynamics that transform the image content into the spatial frequency (Fourier) domain. Exact knowledge of the image encoding terms is essential for the accurate reconstruction of the image content, which would otherwise result in image artifacts or erroneous parameter quantification. Deviations from the modeled image encoding can originate from the MR system itself, e.g. by temperature changes, or it can originate from physiological activity of the subject that is imaged, e.g. due to its heartbeat or breathing activity.

The most severe levels of image degradation, however, are caused by subject motion. In many MRI applications, it is subject motion that limits the utility of MRI for medical diagnostics. In head MRI, such motion is predominantly that of a rigid body, i.e. it can be described by a rotation and a translation, which allows correcting for it by continuously adapting the geometry of the MR imaging experiment to the head position. The six parameters that describe the rigid body motion can be encoded and measured in various different ways with their individual advantages and disadvantages. Prominent recent approaches to address this problem are based on either optical or radio-frequency (RF) methods. Optical methods encode the head position with a marker on the subject's head that is observed by a camera. RF-based methods employ a small NMR sample whose position is encoded by means of static gradient fields and measured by means of a small RF receive coil that is tightly wound around it. Such sensors are termed "field probes" and exploit the fact that the applied gradient fields provide a unique mapping between a coordinate and the carrier frequency of the NMR sample. Compared to RF-based approaches, the main advantage of optical methods is that they require no modification to the MR sequence, rendering the motion correction process completely independent of the MR system activity. However, optical methods require line-of-sight access to the marker, which is often very difficult to obtain in current MR systems that rely on equipment such as tightly fitting imaging coils, narrow magnet bores, or head-mounted goggles for neurological research. RF-based methods are therefore very promising alternatives in terms of MR system compatibility. To this end, however, they have encoded the NMR sample's position by additional sequence modules

inserted between successive image acquisition intervals, which interferes with contrast optimization and prolongs sequence duration.

The core idea explored in this thesis is based on the realization that field probes can be localized not only by static gradient fields but also by gradient fields of arbitrary dynamics if the field probe's phase can be tracked within an appropriate time window.

In a first step, the idea to use sinusoidal gradient field dynamics for field-probe tracking, so-called gradient tones, is presented. It is shown that such oscillations can be orthogonally superimposed onto existing sequence gradients for simultaneous field probe localization and image encoding. Gradient tones come with the additional benefit that their frequency can be chosen such that expected undesired field perturbations do not interfere with the field probe localization, which increases accuracy. An array of four field probes is mounted on a subject's head, which readily allows tracking of the head's rigid body motion. In addition to motion correction, the field probe array is capable of simultaneously measuring the gradient encoding acting on the head, which improves image reconstruction in the presence of undesired field perturbations in the image-encoding task. The concept is successfully implemented into a multi-slice gradient-echo sequence to show its efficacy in both a phantom and in a healthy volunteer. It is found that the field probe can be localized with precisions (measured in standard deviations) in the order of tens of micrometers for observation windows of less than 5 milliseconds while an image encoding sequence was running.

In a second step, the first implementation is developed further in order to make motion correction with gradient tones more accessible to routine clinical head imaging. To facilitate this, the gradient tones are no longer superimposed onto image encoding gradients but on crusher gradients. In this fashion, several simplifications of the first implementation are achieved. Among others, it is possible to use the image reconstruction pipeline provided by the manufacturer and no orthogonalization between sequence and tones gradients are necessary, which greatly simplifies their use. The increased flexibility allowed to use more sensitive gradient tones that achieved precisions of ten micrometers within an observation window of 2 milliseconds.

In a third step, an alternative to gradient tones is developed. In this approach, existing sequence gradient dynamics that already contain substantial intrinsic high-frequency content are exploited to encode the probe position. In contrast to gradient tones, which rely on single frequencies, this approach allows to perform field probe localization based on wide-band spectral information. The required generalization of the calibration method is presented, and the method's efficacy is

demonstrated in volunteer experiments using an echo-planar imaging sequence. The benefit of relying on the intrinsic high-frequency content of a sequence does away with the requirement to add additional gradient waveforms such as tones, which helps in situations where no additional gradient performance is available. In many neuroimaging applications it is of paramount importance that all available gradient performance is available for the imaging task and not traded for probe localization with additional gradient dynamics.

It is concluded that the proposed methods are feasible and work in vivo. Successful rigid body motion correction is demonstrated by means of continuously updating the sequence geometry based on the proposed methods. The obtained precisions and accuracies are high enough for typical imaging situations.

Zusammenfassung

Die Magnetresonanztomographie (MRI) überlagert dynamische Gradientenfelder einem statischen, räumlich homogenen Magnetfeld, um räumliche Bildinformation aufzulösen. Die Bildkodierung wird erreicht durch dynamisches Schalten von Gradientenspulen, welche den Bildinhalt in den Raumfrequenzbereich transferiert. Die exakte Kenntnis der Bildkodierungsterme ist eine wesentliche Voraussetzung für die genaue Wiederherstellung des Bildinhalts, weil sonst Bildartefakte oder fehlerhafte Quantifizierung von physiologischen Parametern folgen würden. Abweichungen von modellierten Bildkodierungstermen entstehen entweder im MRI-System selbst, z.b. durch Temperaturveränderungen, oder entstehen durch physiologische Aktivität des Subjekts im Scanner, z.b. durch seinen Herzschlag oder als Folge seiner Atmung.

Die auffälligsten Bildartefakte stammen jedoch von der Bewegung des Subjektes. In vielen MRI-Anwendungen ist Subjektbewegung der limitierende Faktor der Qualität von diagnostischen MRI-Untersuchungen. Im Falle von MRI des Kopfes ist diese Bewegung die eines Starrkörpers, d. h. sie kann durch eine Rotation sowie eine Verschiebung beschrieben werden. Dies ermöglicht die Korrektur der Bewegung durch kontinuierliche Anpassung der Geometrie des laufenden MRI-Experimentes an die aktuelle Kopfposition. Die sechs Parameter, welche die Kopfbewegung beschreiben, können mit unterschiedlichen Mitteln bestimmt werden, welche jede ihre individuellen Vor- und Nachteile aufweisen. Bekannte Ansätze, die in den letzten Jahren unternommen wurden, das Bewegungsproblem zu lösen, basieren entweder auf optischen oder Radiofrequenzmethoden. Optische Methoden kodieren die Kopfposition mittels eines Markers, der auf dem Kopf des Subjektes befestigt wird, und beobachten diesen mit einer Kamera. Radiofrequenzmethoden benutzen einen kleinen Tropfen mit NMR-aktivem Kern, wessen Position mit statischen Gradientenfeldern kodiert wird. Das Signal des Tropfens wird mit einer kleinen Radiofrequenzspule gemessen, welche möglichst eng um den Tropfen gewunden wird. Solche Sensoren werden "Magnetfeldsonden" genannt und nützen die Tatsache, dass das angewendete Gradientenfeld eine eindeutige Zuordnung einer Tropfenkoordinate und der Resonanzfrequenz des Tropfens ermöglicht. Im Vergleich zu Radiofrequenzmethoden haben optische Methoden den Vorteil, dass sie keine Modifizierungen der MRI-Sequenz benötigen, was es ermöglicht, die Bewegungskorrektur völlig unabhängig davon durchzuführen. Optische Methoden benötigen jedoch Sichtkontakt mit dem Marker, was in modernen MRI-Scannern oft sehr schwierig zu erreichen ist, weil diese mit sehr engen Empfangsspulen, engen

Magnetbohrungen oder Brillen für die neurologische Forschung ausgestattet sind. Radiofrequenzmethoden sind deshalb eine sehr vielversprechende Alternative bezüglich MR-Systemkompatibilität. Bisher haben solche Methoden jedoch die Position von Magnetfeldsonden mittels zusätzlichen Sequenzmodulen bestimmt, welche zwischen aufeinanderfolgenden Bildgebungsintervallen eingefügt werden und deshalb die Kontrastoptimierung stören und die Sequenzdauer verlängern.

Die Kernidee, die in dieser Forschungsarbeit verfolgt wird, basiert auf der Erkenntnis, das Magnetfeldsonden nicht nur mit statischen Gradientenfeldern kodiert werden können, sondern auch mit Gradientenfeldern von beliebiger Dynamik, wenn die Phase der Magnetfeldsonde über ein geeignetes Zeitfenster beobachtet werden kann.

In einem ersten Schritt wird die Idee vorgestellt, sinusoidale Gradientenfelddynamiken, sogenannte Gradiententöne, für die Lokalisierung von solchen Sonden zu verwenden. Es wird dabei gezeigt, dass solche Einzelfrequenzoszillationen orthogonal zu existierenden Sequenzgradienten überlagert werden können, welche simultane Sondenlokalisierung und Bildkodierung ermöglicht. Gradiententöne haben den zusätzlichen Vorteil, dass ihre Frequenz so gewählt werden kann, dass unerwünschte Störungen des Magnetfeldes die Sondenlokalisierung nicht beeinflussen, was der Genauigkeit der Methode zugute kommt. Vier Sonden werden auf dem Kopf eines Subjektes befestigt, welches es ermöglicht, dessen Starrkörperbewegung zu verfolgen. Zusätzlich zur Bewegungskorrektur sind die vier Magnetfeldsonden in der Lage, simultan die Bildkodierung des Kopfes durch Gradientenfelder zu beobachten, was die Bildrekonstruktion verbessert, wenn unerwünschte Feldstörungen präsent waren. Das Konzept ist in eine Gradientenechosequenz implementiert worden, um ihre Wirksamkeit im Phantom und in einem gesunden Volontär zu zeigen. Es stellte sich heraus, dass die Magnetfeldsondenlokalisierung in der Grössenordnung von einigen zehn Mikrometern erreicht werden kann (gemessen in Standardabweichungen von mehreren Messungen), wobei dazu Beobachtungszeiträume von weniger als 5 Millisekunden benötigt wurden während der Ausführung einer Bildkodierungssequenz.

In einem zweiten Schritt wurde diese erste Implementation weiterentwickelt, um die Anwendung der Gradiententöne für die Bewegungskorrektur von klinischen Routinescans einfacher zu machen. Im dies zu erreichen werden die Gradiententöne nicht mehr nicht länger der Bildkodierungssequenz überlagert, sondern auf den Crushergradienten platziert. Dies ermöglicht mehrere Vereinfachungen des ursprünglichen Designs. Unter anderem ist es mit der neuen Implementation möglich, die Scanner-eigene Bildrekonstruktionspipeline zu benutzten,

was die praktische Anwendung stark vereinfacht. Zudem muss keine orthogonalisierung zwischen exisitierenden Sequenzgradiaenten und den Gradiententönen mehr vorgenommen werden, was deren Benutzung stark vereinfacht. Die verbesserte Flexibilität ermöglicht Sondenlokalisierung mit einer Präzision von zehn Mikrometer in einem Zeitraum von 2 Millisekunden.

In einem dritten Schritt wurde eine Alternative zu den Gradiententönen entwickelt. In diesem Ansatz Sequenzgradientendynamiken, welche bereits über substantielle Hochfrequenzanteile verfügen, ausgenutzt um die Sondenposition zu kodieren. Im Unterschied zu Gradiententönen, welche auf Einzelfrequenzen beruhen, ermöglicht dieser Ansatz die Sondenlokalisierung basierend auf spektraler Breitbandinformation. Es wird gezeigt, wie die Erweiterung der Kalibrierung erreicht wird, und die Methode wird in Volontärexperimenten validiert am Beispiel einer echo-planaren Bidgebungssequenz. Der Vorteil, sich auf intrinsische Hochfrequenzinformation von existierenden Sequenzgradientendynamiken zu verlassen ermöglicht es, ohne zusätzliche Gradientendynamiken wie Tones auszukommen, welches ein entscheidender Vorteil ist, wenn keine Leistung vom Gradientensystem mehr zu Verfügung steht. Dies ist von höchster Wichtigkeit in vielen neurologischen Anwendungen, welche die maximal zu Verfügung stehende Leistung von Gradientensystem zur Bildkodierung benötigt und es sich nicht leisten kann, solche für Sondenlokalisierung zu verwenden.

Die Schlussfolgerungen dieser Arbeit sind, dass die neu vorgeschlagenen Methoden machbar sind und an Volontären funktionieren. Starrkörperbewegung wurde erfolgreich korrigiert durch das kontinuierliche Nachführen der Sequenzgeometrie basierend auf den Methoden, die hier entwickelt wurden. Die erreichten Genauigkeiten und Präzisionen sind hoch genug für typische Bildgebungssituationen.

Introduction

Basics of magnetic resonance imaging

Magnetic resonance imaging (MRI) is an imaging technique that is widely used in a large variety of biomedical applications. In clinical medicine, for instance, it allows the depiction of anatomical and physiological abnormalities in the central nervous system, the cardiovascular system and the musculoskeletal system, among others. In neurological research, MRI is used to resolve brain connectivity and activity both spatially and temporally.

MRI relies on the phenomenon of nuclear magnetic resonance (NMR), discovered by Rabi, Bloch and Purcell (Rabi 1937; Bloch 1946; Purcell, Torrey, and Pound 1946), and describes the phenomenon that atomic nuclei with a magnetic moment absorb electromagnetic radiation at well-defined, single resonance frequency if they are exposed to an external magnetic vector field $\boldsymbol{B}_0$. The direction of the magnetic field vector is called the longitudinal direction, and the plane perpendicular to it is called the transversal plane. The resonance condition is given by the energy difference ΔE between the two spin states that atomic nuclei can assume in such a scenario

$$\Delta E = \gamma\hbar|\boldsymbol{B}_0|. \qquad [1]$$

$\hbar$ denotes Planck's constant, and γ is the nucleus-specific proportionality factor, called "gyromagnetic ratio". $|\boldsymbol{B}_0|$ is a scalar and denotes the magnitude of the magnetic field at the nucleus, which depends on the externally applied magnetic field and the magnetic shielding by the electrons surrounding the nucleus. The latter causes small shifts in the resonance condition of the nuclei depending on their molecular environment, the so-called "chemical shift". Hence, the resonance condition is not only, but still dominantly, determined by the intrinsic properties of the nucleus but also by its chemical environment. To understand the NMR signal generation and detection, however, the chemical shift is not central and will not be discussed any further. NMR occurs when the photon energy E_{photon} of the irradiated electromagnetic wave equals the energy difference between the two spin states:

$$E_{photon} = \hbar\omega = \gamma\hbar|\boldsymbol{B}_0|. \qquad [2]$$

ω is the angular frequency of the electromagnetic wave. The left-hand equality, $E_{photon} = \hbar\omega$, is the Planck relation, and the right-hand side equality, $\hbar\omega = \gamma\hbar B_0$, is the Larmor equation. The frequency that fullfills the Larmor equation is called the Larmor frequency and denoted by ω_l. The transition process induced by the electromagnetic wave at the Larmor frequency can be described macroscopically by the Bloch equations. They state that a macroscopic magnetization is built up in the transversal plane if the amplitude vector of the irradiating electromagnetic

wave, $\boldsymbol{B}_1^+$, is not parallel to $\boldsymbol{B}_0$. That process is most effective when $\boldsymbol{B}_1^+$ is perpendicular to $\boldsymbol{B}_0$, and entirely ineffective if they are aligned in parallel. Two processes establish the macroscopic magnetization in the transversal plane. In one, the macroscopic magnetization's longitudinal component is reduced by the induction of transitions between the two spin states, thus reducing its component in the longitudinal direction. In another, phase coherence among the individual nuclear spins is established, which results in a precession of the macroscopic magnetization's transversal component at the Larmor.

The resulting nuclear precession then causes an oscillating magnetic flux, which induces a detectable voltage in an induction coil that integrates contributions from all precessing spins within its sensitive volume as follows:

$$v(t) \sim \int_{Volume} \rho(\boldsymbol{r}) s(\boldsymbol{r}) \cos(\omega_l(\boldsymbol{r})t)\ d\boldsymbol{r}. \qquad [3]$$

ρ denotes the spin density within an infinitesimal volume element $d\boldsymbol{r}, s(\boldsymbol{r})$ denotes the complex-valued sensitivity of the receive coil, and $v(t)$ denotes the induced voltage in the coil, and $\sim$ denotes proportionality.

In most NMR experiments, the electromagnetic irradiation is stopped after a desired time (1^{-6} s), which results in well-defined magnetization components in both the longitudinal direction and the transversal plane, respectively, and separates the experiment into two distinct periods, the excitation (the period prior to the end of the pulse) and the free induction decay (FID). During the FID, the magnetization component in the transversal plane decays exponentially with a time constants that depend on the various interactions of the precessing nuclei with their environment (T_2, T_2^*). Simultaneously, the magnetization component in the longitudinal direction is re-established to its thermal equilibrium value following an exponential curve with a different time constant (T_1).

These first principles can be used to perform imaging by varying ω_l spatially and temporally to encode the image information. The idea was first devised by Lauterbur (Lauterbur 1973) and will be referred to as gradient encoding. The signal in a receive coil generated by a stationary object in the imaging volume with initial magnetization $\rho(\boldsymbol{r})$ is defined as follows:

$$m(t) = \int_{Volume} \rho(\boldsymbol{r}) s(\boldsymbol{r}) e^{i \int_0^t \omega_l(r,\tau)d\tau} d\boldsymbol{r} + \eta(t). \qquad [4]$$

The transverse magnetization $\rho(\boldsymbol{r})$ is generated by a set of preparation pulses, reflects its spatially dependent history of excitation and FID periods and is generally complex-valued. In an MRI experiment, spatiotemporal variations of ω_l are realized with gradient coils surrounding the object to be imaged. This has two relevant consequences: First, the dynamics

of the temporal field variations is limited to a few tens of kHz, which sets the electrodynamics of MR image encoding in the quasi-static regime. This allows considering the temporal and spatial components of ω_l separately. Second, the spatial variations of ω_l will be of low spatial order in terms of spherical harmonic coefficients. As a result, the resulting spatiotemporal model for ω_l can be expanded as follows:

$$\omega_l(\boldsymbol{r},t) = \gamma \sum_{n=0}^{N_p-1} c_n(t) f_n(\boldsymbol{r}) + \omega^{static}(\boldsymbol{r}). \qquad [5]$$

$f_n(\boldsymbol{r})$ denotes the nth spherical harmonic basis function evaluated at the position $\boldsymbol{r}$ and ω^{static} denotes the spatially dependent static off-resonance frequency. ω^{static} reflects the effective magnetic field seen by the nucleus and γ denotes the nucleus' gyromagnetic ratio. N_p denotes the number of basis functions in which the field is expanded.

Inserting [5] into [4] and rearranging terms yields

$$m(t) = \int_{Volume} \rho(\boldsymbol{r}) s(\boldsymbol{r}) e^{i\gamma \int_0^t \sum_{n=0}^{N_p-1} c_n(\tau) f_n(r) d\tau + i\omega^{static}(r)t} d\boldsymbol{r} + \eta(t). \qquad [6]$$

Another spatial encoding mechanism is provided by the complex-valued sensitivity profile of the receive coil, $s(\boldsymbol{r})$. It provides a spatial encoding mechanism that is complementary to gradient encoding and depends on the relative position between receive coil and the object to be imaged. This allows to acquire additional image information with receive coils placed at different locations, which can be achieved concurrently if arrays of receive coils are used. This reduces the amount of information to be encoded by gradient encoding, which, due to its sequential nature, reduces scan time. This forms the basis of parallel MR imaging. As the two encoding mechanisms co-encode the image information, it is unclear a priori which combination of the two is the most sensitive in terms of thermal noise in an MR image reconstruction. Chapter 5 of this thesis deals with optimizing gradient encoding for a given set of sensitivity profiles of an MR receive array to manipulate propagation of thermal noise in parallel image reconstruction.

Reconstruction of the image content $\rho(\boldsymbol{r})$ relies on the accurate knowledge of its encoding terms. Reflecting different degrees of magnetic susceptibility-induced tissue magnetization, $\omega^{static}(\boldsymbol{r})$ can vary strongly over short distances in space so that it needs to be determined for each position at which the image content is to be reconstructed, which requires additional encoding with at least the desired image resolution. Approaches to address this problem include field mapping and point-spread-function mapping methods (Jezzard and Balaban 1995; Zaitsev, Hennig, and Speck 2004). The sensitivity profiles $s(\boldsymbol{r})$ reflect electric interactions between the receiver coils and the tissue, which is less structured in space and thus can be obtained with additional encoding below the desired image resolution and be interpolated to the desired image

resolution (Pruessmann et al. 1999). Sensitivity profiles can also be obtained if fully-sampled low-resolution information is available in a partially undersampled image encoding scheme (Griswold et al. 2002; Ying and Sheng 2007; Uecker et al. 2014). The gradient encoding terms $c_n(\tau)$, and their time integral $\boldsymbol{k}_n(t)$, reflect the realization of the gradient encoding in the actual experiment, which is often calibrated (Duyn et al. 1998; Addy, Wu, and Nishimura 2012; Tan and Meyer 2009). Such methods are inherently limited as they are not able to capture the actual gradient encoding in the experiment of interest. In particular, they are not able to capture slow main field drifts or field perturbations due to physiological activity during the experiment. A prominent example includes field perturbations due to subject breathing (Versluis et al. 2010; Van de Moortele et al. 2002), which results in image artifacts due to unaccounted image encoding terms.

To overcome the intrinsic limitations of calibration-based gradient encoding estimation methods, Barmet et al. have recently proposed to measure the integral of the gradient encoding terms $c_n(\tau)$ during the experiment of interest (Barmet, Zanche, and Pruessmann 2008). Their approach allows to determine the spatiotemporal field evolution within the field-of-view (FOV) by means of miniature induction coils that observe the phase of an NMR sample, so-called "field probes" (De Zanche et al. 2008), subject to the gradient encoding. If the volume occupied by such a field probe is very small compared to the imaging volume of the imaging experiment, its signal density can be approximated by a Dirac pulse at the probe position $\boldsymbol{r}_p$, i.e. $\rho(\boldsymbol{r}) = \delta(\boldsymbol{r} - \boldsymbol{r}_p)$. Neglecting thermal noise, the complex-valued field probe signal $m_p(t)$ is given as follows:

$$m_p(t) = \int_{Volume} \delta(\boldsymbol{r} - \boldsymbol{r}_p)s(\boldsymbol{r})e^{i\gamma \int_0^t \Sigma_{n=0}^{Np-1} c_n(\tau)f_n(\boldsymbol{r})d\tau + i\omega^{static}(\boldsymbol{r})t}d\boldsymbol{r}. \quad [7]$$

Exploiting the filter property of the Dirac pulse, it becomes clear that $m_p(t)$ is a direct measure of the gradient encoding terms:

$$m_p(t) = s(\boldsymbol{r}_p)e^{i\gamma \int_0^t \Sigma_{n=0}^{Np-1} c_n(\tau)f_n(\boldsymbol{r}_p)d\tau + i\omega^{static}(\boldsymbol{r}_p)t}. \quad [8]$$

In reality, the probe dimensions are a finite approximation of the Dirac pulse, which requires precise manufacturing the of field probes in order to ensure that $s(\boldsymbol{r}) \approx s(\boldsymbol{r}_p)$, and $\omega^{static}(\boldsymbol{r}) \approx \omega^{static}(\boldsymbol{r}_p)$ over the region that contributes to the induction signal. Under these constraints, the phase $\phi_p(t)$ of the measured field probes signal $m_p(t)$ directly reflects the gradient encoding at the probe location. The frequency offset $\omega^{static}(\boldsymbol{r}_p)$ can easily be calibrated by performing a measurement without gradient activity (De Zanche et al. 2008). The probe phase $\phi_p(t)$ is given by (Barmet, Zanche, and Pruessmann 2008):

$$\phi_p(t) = \gamma \int_0^t \sum_{n=0}^{N_p-1} c_n(\tau) f_n(\boldsymbol{r}_p) \, d\tau + \omega^{static}(\boldsymbol{r}_p)t. \tag{9}$$

Defining $k_n(t) = \gamma \int_0^t c_n(\tau) d\tau$ further simplifies Eq. [9] to

$$\phi_p(t) = \sum_{n=0}^{N_p-1} k_n(t) f_n(\boldsymbol{r}_p) + \omega^{static}(\boldsymbol{r}_p)t. \tag{10}$$

The N_p unknown coefficients $k_n(t)$ can be computed for a suitably chosen set of spatial basis functions $f_n(\boldsymbol{r}_p)$ evaluated at the probe position. The basis functions are typically chosen to be spherical harmonics whose 0th and 1st order terms are as follows:

$$f_0(\boldsymbol{r}_p) = 1, f_1(\boldsymbol{r}_p) = x_p, f_2(\boldsymbol{r}_p) = y_p, f_3(\boldsymbol{r}_p) = z_p. \tag{11}$$

where $\boldsymbol{r}_p = (x_p, y_p, z_p)^T$. The determination of $k_n(\tau)$ is achieved by a linear least-squares inversion of Eq.[10]; details are described in (Barmet, Zanche, and Pruessmann 2008). The correct assessment of the three different image-encoding factors, coil sensitivity profiles, off-resonance frequencies, and gradient encoding, allows for well-informed image reconstruction. Formally, image reconstruction described solving Eq. [6] for the image signal density $\rho(\boldsymbol{r})$. Image reconstruction in Chapter 5 relied on all three of them, and Chapters 2 – 4 relied on gradient encoding only.

Position encoding for motion tracking

The above considerations are based on the assumption that the subject does not move. In practice, this is often not the case. In many applications, motion is very complex and cannot be avoided as it serves vital physiological functions. Prominent examples are the beating heart during a cardiac imaging examination, organ and thorax motion due to breathing, or blood flow in arteries and veins. In other cases, motion is due to circumstantial reasons such as nervousness, discomfort, or anxiety. The effects of motion include, among others, image artifacts and erroneous determination of physiological parameters.

Formally, motion causes modifications of the signal equation (Eq. [6]) as the signal density $\rho(\boldsymbol{r})$ becomes a function of the time-dependent position, i.e. $\rho(\boldsymbol{r}) = \rho(\boldsymbol{r}(t))$. Accounting for motion means fixing the relation among all position-dependent variables in the signal equation over the course of the data acquisition. Due to the complexity of that problem, proposed solutions always address a specific imaging scenario and model motion with a manageable number of degrees of freedom. Temporal degrees of freedom can be reduced by assumptions on the motion's bandwidth, temporal occurrence, or maximum velocity. Spatial degrees of freedom can be reduced by assumptions on its spatial origin, its direction, and spatial correlations. The focus of this thesis is on the case of rigid body motion. Motion is rigid if its

time-dependent position $r(t)$ of tissue magnetization $\rho\big(r(t)\big)$ can be described by one rotation and one translation of a reference position for each time point, i.e. $r(t) = R(t)r_0 + q(t)$, where R denotes a 3x3 orthogonal rotation matrix, q denotes a 3x1 translation vector, and r_0 denotes a reference position. In rigid body motion, the above relation holds true for all positions of tissue magnetization. The task of correcting for rigid body motion reduces to applying the rigid body parameters, $R(t), q(t),$ to the position-dependent variables in the signal equation. This is achieved by adapting the excitation volume in to conserve ρ, and adapting the gradient encoding to ensure its encoding consistency. These measures, once the rigid body parameters are known, are relatively easily implemented by software modifications. The rotation of the excitation volume and the gradient encoding can be simply rotated by multiplying their input with the rotation matrix, the translation of the excitation volume is adapted by changing the center frequency of the excitation pulse, and translation in the gradient encoding can be accounted for by adapting the demodulation frequency and phase.

The difficult part in correcting for rigid body motion is measuring the rigid body parameters in the first place. A variety of different approaches have been proposed to obtain them directly from the MR experiment. If, for example, the experiment is such that an entire image volume is encoded within one excitation, the rigid body parameters could be obtained by comparing simply co-registering images of two subsequent acquisitions. Such image-space approaches are limited, however, to 3D single-shot acquisitions, which are rarely done due to the imaging problems associated with their long readout duration. In the case of multi-shot sequences, image-based motion correction is only possible after a 3D estimate of the imaging volume has been obtained (Thesen et al. 2000). Such methods suffer from a very long temporal delay, which limits their effectiveness in practice.

In order to increase the update rate in image-based motion correction methods for multi-shot imaging sequences, it has been proposed to insert additional sequence parts capable of encoding an estimation of the 3D image content within a very narrow time window (White et al. 2010; Tisdall et al. 2012).

Another category of approaches, so-called k-space navigators, rely on additional sequence parts optimized to encode the object's position instead of its image content. They exploit the fact that rigid body motion is directly encoded into the magnitude and phase of the object's k-space signal according to well-known Fourier theorems, which allows obtaining the rigid body parameters with substantially less acquisition time compared to image-space methods. Such navigators rely on low flip-angle re-excitations of the entire object, or parts thereof, and analyze

image information in k-space (Ehman and Felmlee 1989; Fu et al. 2005; Welch et al. 2001; van der Kouwe, Benner, and Dale 2006).

Both image space and k-space navigator methods have struggled to gain widespread popularity due to several shortcomings. They disturb the steady state of the object's magnetization and require modifications to the timing of the actual imaging sequence, which can substantially prolong scan time. Furthermore, they assume that the only image encoding mechanism acting on the image is gradient encoding and neglect the other encoding mechanisms, which may cause systematic errors, particularly in k-space navigators. Finally, the precision of navigator methods depends on the available structure in the object's k-space and image space, respectively, and is thus situation specific.

It is therefore desirable to encode the rigid body parameters without disturbing the object's steady state, without interfering with the sequence timing and without the influencing the encoding mechanisms of receiver sensitivities and spatially varying off-resonance frequencies. These issues can be addressed by replacing the source of the rigid body parameter computation, previously the object to be imaged, by NMR field probes whose motion mimics the object's rigid body motion. Occupying separate receive channels and reflecting signal from a small, localized volume that does not move with respect to the coil receiving its signal, field probe signals do not contain position-dependent signal modulations due to relative motion between the NMR sample and its receiver coil. Recalling Eq. [10] and limiting the spatial basis functions to 0th and 1st order terms as defined in Eq. [11], the field probe's phase reads

$$\phi_p(t) = k_0(t) + k_1(t)x_p + k_2(t)y_p + k_3(t)z_p + \omega^{static}(\boldsymbol{r}_p)t. \qquad [12]$$

Retrieving the probe's coordinates form its phase is a linear problem in the coordinates, which is offset by the gradient encoding's coupling into the homogeneous field component, $k_0(t)$, and the probe's static off-resonance frequency $\omega^{static}(\boldsymbol{r}_p)$. Dumoulin et al. proposed to determine the coordinates by performing a sequence of four measurements, each determining one of the four unknowns, $x_p, y_p, z_p, \omega^{static}(\boldsymbol{r}_p)$, while assuming that $k_0(t) = 0$ (Dumoulin, Souza, and Darrow 1993). The mathematical model for their method looks as follows:

$$\begin{aligned}
\phi_p^x(t) &= k_1(t)x_p + \omega^{static}(\boldsymbol{r}_p)t, \\
\phi_p^y(t) &= k_2(t)y_p + \omega^{static}(\boldsymbol{r}_p)t, \\
\phi_p^z(t) &= k_3(t)z_p + \omega^{static}(\boldsymbol{r}_p)t, \\
\phi_p^\omega(t) &= \omega^{static}(\boldsymbol{r}_p)t.
\end{aligned} \qquad [13]$$

$\phi_p^i(t)$ denotes the probe phase evolution for the experiment to determine the variable $i = \{x_p, y_p, z_p, \omega^{static}(r_p)\}$. Three static gradients were chosen for the position encoding, i.e. $k_{1-3}(t) = \gamma G_{x,y,z}t$. Mathematically, this constitutes an orthogonal system of linear equations that allows the probe's coordinates to be obtained very simply by determining its resonance frequency. Furthermore, the localization is independent of its static off-resonance frequency. The most recent implementation of this concept was presented by Ooi et al., reporting a module duration of 15 ms (Melvyn B. Ooi et al. 2011).

However, this method still requires an additional sequence module, which prolongs scan time. Another important shortcoming of the above method is that the static gradient model is in fact implemented by trapezoids. This causes undesired gradient dynamics due to mechanical oscillations of the gradient system and residual ringing due to the gradient system's finite bandwidth. These effects result in a varying frequency at the probe's position that is not accounted for.

Thesis outline

The present thesis presents the development of an original concept that avoids the shortcomings of aforementioned approach. It is demonstrated that arbitrary gradient dynamics, as opposed to a sequence of non-overlapping static gradients, can be used to determine the probe's coordinates. This novel approach allows avoiding the insertion of additional sequence modules and enables simultaneous probe position encoding and execution of sequence tasks such as image encoding or gradient spoiling. In this way, field-probe based prospective motion correction can be achieved without modifications to sequence timing. A key insight presented in the present thesis is that it is possible to rely on selected high-frequency content of gradient waveforms, which renders the probe localization robust against expected field perturbations stemming from the gradient system or from physiological activity of a subject. Two different aspects are investigated. Chapter 2 treats the case when existing gradient waveforms allow the insertion of single-frequency oscillations in the kilohertz range, dubbed "tones". Chapter 3 considers the case when the existing sequence gradients allow no additional gradient tones and its intrinsic broadband high-frequency content needs to be exploited to allow probe localization. Chapter 4 presents an innovative software and hardware design of the gradient tones concept that facilitates its use in clinical imaging scenarios.

Real-time motion correction using gradient tones and head-mounted NMR field probes

Introduction

During an MRI examination, patients often move for reasons including discomfort, restlessness, nervousness, or pain. Such motion can cause various image artifacts such as ghosting, blurring and ringing as well as cause erroneous quantification of anatomical and physiological properties such as diffusion parameters, tissue volumes and BOLD activation (Brown et al. 2010; Ling et al. 2012). Motion hampers the application of MR to large groups of subjects with difficulty to keep still such as children, elderly, and patients with neurological conditions. Even in compliant subjects involuntary motion still limits imaging accuracy (Maclaren et al. 2012a) and achievable resolution and can be exacerbated in fMRI with certain paradigms such as motor tasks (Seto et al. 2001; J. Schulz et al. 2014; Speck, Hennig, and Zaitsev 2006).

Motion can be accounted for retrospectively upon image reconstruction relying on different estimation methods (Batchelor et al. 2005; Atkinson et al. 1999), which have been applied to correct cardiac (Schmidt et al. 2011; Odille et al. 2008; Odille et al. 2010), respiratory (Buerger, Schaeffter, and King 2011; Filipovic et al. 2011), head, and shoulder motion. However, retrospective motion correction fails in the case of inconsistent selective excitation, which leads to image artifacts or slice misalignment, and in the case of signal dropouts, which are a problem, e.g., in DWI. To overcome this problem the imaging sequence needs to be dynamically adjusted based on information about the motion state. Such information is challenging to retrieve and use for non-rigid motion patterns as encountered, for instance, in the heart and abdomen. It is more amenable, however, for rigid-body motion such as that of the head, which can be parameterized with few degrees of freedom and readily addressed by re-orientation of imaging gradients and adjustment of the excitation and demodulation frequencies (Nehrke and Börnert 2005).

Early approaches for tracking head position were reported in Refs. (Lee et al. 1996; Lee et al. 1998) based on the navigator technique proposed in Ref. (Ehman and Felmlee 1989). Extensions thereof to 2D and 3D led to the development of orbital, spherical and cloverleaf navigators (Fu et al. 2005; van der Kouwe, Benner, and Dale 2006; Welch et al. 2001). One downside of navigator techniques, however, is that they require additional sequence modules, which constrain contrast optimization and increase overall scan duration particularly for short-TR sequences, which are widely used in clinical practice. Furthermore, relying on MR signal from the head itself navigators may alter the magnetization state of tissue to be imaged, which additionally complicates sequence design.

Interference with tissue magnetization can be overcome by external NMR markers based on small samples in miniature RF coils (Derbyshire et al. 1998; Krueger et al. 2006) as originally proposed for catheter tracking (Dumoulin, Souza, and Darrow 1993). However, these methods still require a sequence overhead and additional scan time as they rely on a localization module applied between imaging readouts (M. B. Ooi et al. 2009; Melvyn B. Ooi et al. 2011). Interference with sequence design has been overcome by optical motion tracking (Zaitsev et al. 2006; Aksoy et al. 2008; Andrews-Shigaki et al. 2011), using a camera to observe a marker attached to the head. A range of implementations of this concept have been proposed using different types of markers such as self-encoded checkerboard markers (Aksoy et al. 2008; Forman et al. 2011), retro-reflective markers (Zaitsev et al. 2006), and retro-grade reflective Moiré patterns (Andrews-Shigaki et al. 2011) as well as different camera locations inside (Aksoy et al. 2008; Maclaren et al. 2012a) and outside the magnet bore (Zaitsev et al. 2006; Andrews-Shigaki et al. 2011). Optical motion tracking works independently of the MR experiment and thus demands neither sequence alterations and scan time overhead nor any manipulation of tissue magnetization. Unlike current NMR marker approaches it permits motion detection during arbitrary time windows. A remaining drawback of optical motion tracking, however, is that it requires line-of-sight access to the marker, which can interfere with other demands such as tight-fitting receiver arrays or fMRI equipment like mirrors or goggles.

The goal of the present work is to reconcile the advantages of the aforementioned approaches while avoiding their individual limitations. To this end, we revert to the concept of position tracking with external NMR probes yet avoid sequence overhead and timing issues. This is achieved by the use of high-sensitivity ^{19}F NMR probes localized by gradient tones, i.e., high-frequency gradient oscillations, which are superimposed to a given sequence without affecting its timing. Tones of different frequency are played out via each gradient coil to establish a unique relationship between the position of a probe and the amplitudes of its respective signal phase modulations. High tone frequencies in the kilohertz range are used to achieve robustness against thermal, physiological and ambient field fluctuations and to preserve effective image encoding. In this way, the localization and imaging tasks are separated in the frequency domain rather than in time, which permits their simultaneous execution.

Spectral separation also enables continuous field-probe localization and is not limited to certain sequence windows. In particular, freedom of probe timing permits exactly simultaneous acquisition of probe and imaging signals. This option is of added interest because it promises utility beyond mere prospective sequence adjustment. When operating head-mounted NMR probes simultaneously with periods of image data acquisition they capture not only position

information encoded via the gradient tones but also all other field dynamics that contribute to image encoding. These include potential low-frequency perturbations such as thermal drifts, gradient delays, eddy current effects and field fluctuations due to breathing. Such effects have previously been accounted for by field monitoring with sets of NMR probes mounted in the MR system (Barmet, Zanche, and Pruessmann 2008; De Zanche et al. 2008; Wilm et al. 2011). However, they can equally be extracted from head-mounted probes, which then effectively act as a field monitoring system in the head frame of reference. Conveniently, in the head frame of reference any motion during imaging readouts will appear just as an additional distortion of the field evolution. Therefore, the signals of head-mounted probes form a powerful basis not only of between-TR motion tracking but also of image reconstruction, in which they permit accounting for both low-frequency field imperfections and residual, within-TR motion.

To assess the proposed method in terms of localization precision and accuracy it is first used for tracking of a single probe. In the second part of the study it is then employed for prospective motion correction in brain imaging, using a T_1-weighted gradient-echo sequence in vivo. The potential utility of within-TR field monitoring is tested by comparing image reconstruction based on either the monitoring information or a predetermined reference trajectory.

Methods

Probe tracking with gradient tones

The basic concept pursued in this work is to track magnetic field probes by reliable and reproducible gradient field evolutions that do not alter characteristics of the MR imaging sequence such as the field of view and the resolution. Requirements on a suitable gradient waveform for probe tracking include the ability to uniquely encode coordinates in all 3 spatial dimensions within arbitrarily placed, narrow time windows, an easy response characterization and robustness to external field contaminations. Furthermore, the position-encoding gradient waveform should impose small moments onto image encoding trajectories and be easily separable from typical MR gradient sequences.

Sinusoidal gradient waveforms at kilohertz frequencies meet all these requirements. Operated in parallel at different frequencies on each of the 3 gradient coils, they are able to encode all 3 spatial coordinates synchronously and within arbitrary time windows. It is preferable to choose high oscillation frequencies as it improves the separation between the sinusoids and most

common field contaminations that occur at lower frequencies (e.g., main magnetic field drifts and local field variations due to motion of magnetized tissue). Moreover, gradient system behavior at high frequencies is more stable over time. Being eigenfunctions of linear time invariant systems, sinusoids can be readily characterized in terms of gain, delay, and coupling behavior. The accessible band for sinusoidal gradient tones is lower-bounded by the significant bandwidth of the gradient sequence waveforms and upper-bounded by the gradient system's bandwidth, suggesting frequencies of 5 - 15 kHz on common gradient systems. A triplet of such gradient tones can be formalized as follows:

$$\boldsymbol{G}_{tone}(t) = \left[A_x \sin(2\pi f_x t), \quad A_y \sin(2\pi f_y t), \quad A_z \sin(2\pi f_z t)\right], \qquad [14]$$

where A_l denotes the amplitude of the tone along the spatial dimension l, f_i its frequency and t denotes time.

Determination of probe position

The tones-encoded spatial coordinates of an NMR field probe can be obtained from its phase evolution, which is retrieved by unwrapping the demodulated probe signal (Barmet, Zanche, and Pruessmann 2008). The underlying field evolution is given by the temporal derivative of the probe phase,

$$\frac{1}{\gamma}\frac{d\phi(t)}{dt} = B(t) = \boldsymbol{G}_{tone}(t)\boldsymbol{r} + B_0(\boldsymbol{r}) + \eta(t), \qquad [15]$$

where $B(t)$ denotes the measured magnetic field at the probe's position $\boldsymbol{r}$, $B_0(\boldsymbol{r})$ denotes the static magnetic field at that position, and motion during the probe readout is neglected. t denotes time and $\eta(t)$ denotes real-valued additive Gaussian noise. $\phi(t)$ denotes the unwrapped phase of the demodulated probe signal, as described in Ref. (De Zanche et al. 2008) and γ denotes the gyromagnetic ratio of the field probe's NMR active sample. The noise level of the field measurement depends on the probe signal's time-dependent SNR, which is limited by thermal noise in the field probe's receive chain.

Assembling the sampled field values in the column vector $\boldsymbol{b}$, the field model can be written in matrix-vector notation:

$$\boldsymbol{b} = \boldsymbol{G}_{tone}\boldsymbol{r} + \mathbf{1}B_0(\boldsymbol{r}) + \boldsymbol{\eta}, \qquad [16]$$

where $\boldsymbol{G}_{tone}$ is a matrix whose elements (n, l) denote gradient field values along the spatial dimension $l = x, y, z$ sampled at $t = n\Delta t$. The sampling interval is denoted by Δt and n is an integer counting the samples. $\mathbf{1}$ is a column vector filled with ones and $\boldsymbol{\eta}$ is the vector of sampled noise instances. $\boldsymbol{\eta}$ is of zero mean and time-dependent signal variance $\sigma_b(n\Delta t) = 1/\big(\gamma\Delta t SNR(n\Delta t)\big)$, where $SNR(n\Delta t)$ denotes the signal-to-noise ratio of the complex-valued

probe signal and γ denotes the gyromagnetic ratio of the probe's nucleus. Ψ_b denotes the covariance matrix of $\boldsymbol{\eta}$ with diagonal elements $\Psi_b(n,n) = \sigma_b^2(n\Delta t)$. A more detailed derivation of the noise statistics is given in Ref. (De Zanche et al. 2008).

The probe's coordinates can be obtained in two steps. First, $\boldsymbol{b}$ is projected onto the subspace spanned by the tones:

$$\boldsymbol{G}_{tone}{}^H \boldsymbol{b} = \boldsymbol{G}_{tone}{}^H \boldsymbol{G}_{tone}\boldsymbol{r} + \boldsymbol{G}_{tone}{}^H \mathbf{1} B_0(\boldsymbol{r}),\qquad [17]$$

which reduces to the following normal equation:

$$\boldsymbol{G}_{tone}{}^H \boldsymbol{b} = \boldsymbol{G}_{tone}{}^H \boldsymbol{G}_{tone}\boldsymbol{r}\qquad [18]$$

under the constraint:

$$\boldsymbol{G}_{tone}{}^H \mathbf{1} = \mathbf{0}.\qquad [19]$$

The superscript H is the hermitian adjoint operator. Eq. [19] requires the gradient tone waveform to be of zero mean in the designated time window, which renders position determination independent of the static field. This requirement is fulfilled by small adjustments of the tone frequencies such that they are harmonics of the probe signal's acquisition window. In a second step, the SNR-optimal least-squares estimate of $\boldsymbol{r}$ is obtained by

$$\boldsymbol{r} = \boldsymbol{G}_{tone}{}^{+}\boldsymbol{b},\qquad [20]$$

where $\boldsymbol{G}_{tone}{}^{+} = \left(\boldsymbol{G}_{tone}{}^H \Psi_b{}^{-1}\boldsymbol{G}_{tone}\right)^{-1}\boldsymbol{G}_{tone}{}^H \Psi_b{}^{-1}$ denotes the SNR-optimal Moore-Penrose pseudoinverse of $\boldsymbol{G}_{tone}$.

The precision of the position measurement can be formalized as follows:

$$\Psi_r = \boldsymbol{G}_{tone}{}^{+}\Psi_b\left(\boldsymbol{G}_{tone}{}^{+}\right)^H = \left(\boldsymbol{G}_{tone}{}^H \Psi_b{}^{-1}\boldsymbol{G}_{tone}\right)^{-1},\qquad [21]$$

$$\sigma_{r_i}^2 = (\Psi_r)_{i,i},\qquad [22]$$

where Ψ_r denotes the noise covariance matrix and $\sigma_{r_i}^2$ is the variance of the probe coordinate $\mathbf{r}_i$. Eqs. [21], [22] allow predicting the precision of the position measurement based on its time-dependent SNR (**Figure 3**).

Gradient response and calibration

The considerations above assume ideal gradient performance. To account for real gradient behavior, the field response of a tone was modeled as the output of a linear time-invariant (LTI) system, encompassing linear effects such as amplitude scaling, phase delays and coupling into other field components. The LTI behavior of the gradient system could be determined by measuring its full impulse response function (Signe J. Vannesjo et al. 2013). In this work, however, it is sufficient to know the system response at the 3 tone frequencies and a full LTI

characterization via the impulse response function was not required. Instead, the tones were formalized as complex exponentials, changing Eq. [14] as follows:

$$\boldsymbol{G}_{tone}(t) = \left[A_x e^{i2\pi f_x t}, \quad A_y e^{i2\pi f_y t}, \quad A_z e^{i2\pi f_z t}\right], \qquad [23]$$

The system response was modeled as a multiplication with the complex-valued matrix $(\boldsymbol{C}|\boldsymbol{c}_0)$, which augments Eq. [16] as follows:

$$\boldsymbol{b} = \boldsymbol{G}_{tone}(\boldsymbol{C}|\boldsymbol{c}_0)\binom{\boldsymbol{r}}{1} + \mathbf{1}B_0(\boldsymbol{r}), \qquad [24]$$

where $\boldsymbol{C}$ denotes a complex-valued 3x3 matrix with elements $c_{m,l}$ reflecting the coupling between the applied tone at a frequency f_m and a gradient field component on the l axis. $\boldsymbol{c}_0$ denotes a column vector of coupling factors $c_{m,0}$ from the applied tones to the homogeneous field component and m denotes the frequency index. If one chooses to neglect coupling between different field components $\boldsymbol{C}$ becomes diagonal and $\boldsymbol{c}_0$ vanishes. Analogously to Eq. [20], the probe positions are obtained by a linear inversion of Eq. [24]:

$$\boldsymbol{r} = \boldsymbol{C}^+\left(\boldsymbol{G}_{tone}{}^+\boldsymbol{b} - \boldsymbol{c}_0\right). \qquad [25]$$

Note that the term $\mathbf{1}\,B_0(r)$ vanishes under the constraint described by Eq. [19] and that the position obtained in this way is generally complex, whereas a real value is expected from the physical model in Eq. [15]. Given perfect decoupling, it is sufficient to consider the real part of $\boldsymbol{r}$ as the probe's position. In order to be robust against small variations in the tones phase, however, it is also possible to consider the magnitude of $\boldsymbol{r}$ as the probe's position with the real part of $\boldsymbol{r}$ determining the sign of the position. In this work, the latter method was used to obtain the probe's position.

The individual rows of the system response matrix $(\boldsymbol{C}|\boldsymbol{c}_0)$ can be obtained by measuring tones responses at 4 known positions r_{1-4}, yielding a modification of Eq. [24] as follows:

$$(\boldsymbol{b}_1, \boldsymbol{b}_2, \boldsymbol{b}_3, \boldsymbol{b}_4) = \boldsymbol{G}_{tone}(\boldsymbol{C}|\boldsymbol{c}_0)\begin{pmatrix} \boldsymbol{r}_1 & \boldsymbol{r}_2 & \boldsymbol{r}_3 & \boldsymbol{r}_4 \\ 1 & 1 & 1 & 1 \end{pmatrix}$$
$$+ \mathbf{1}\big(B_0(\boldsymbol{r}_1), B_0(\boldsymbol{r}_2), B_0(\boldsymbol{r}_3), B_0(\boldsymbol{r}_4)\big). \qquad [26]$$

The least-squares estimate of the matrix $(\boldsymbol{C}|\boldsymbol{c}_0)$ is obtained by linear algebra:

$$\boldsymbol{G}_{tone}{}^+(\boldsymbol{b}_1, \boldsymbol{b}_2, \boldsymbol{b}_3, \boldsymbol{b}_4)\begin{pmatrix} \boldsymbol{r}_1 & \boldsymbol{r}_2 & \boldsymbol{r}_3 & \boldsymbol{r}_4 \\ 1 & 1 & 1 & 1 \end{pmatrix}^{-1} = (\boldsymbol{C}|\boldsymbol{c}_0), \qquad [27]$$

where the last term in Eq.[13] again drops out due to condition [6].

Prospective rigid-body motion correction

The capability to localize NMR field probes enables the position tracking of the head if at least 3 such probes are attached to it in a linearly independent rigid-body configuration (M. B. Ooi et al.

2009). In order to both track the head orientation with 6 degrees of freedom and perform field monitoring of 0th and 1st order, a rigid body arrangement of 4 NMR field probes is required. The first objective is to track the positions of the probes during arbitrary MR gradient activity. The superposition of tones and other sequence gradient waveforms causes field evolutions not captured in Eq. [16], which needs to be augmented as follows:

$$\boldsymbol{b} = (\boldsymbol{G}_{sequence} + \boldsymbol{G}_{tone})\boldsymbol{r} + \mathbf{1}B_0(\boldsymbol{r}), \qquad [28]$$

where $\boldsymbol{G}_{sequence}$ is a matrix whose elements (k, l) denote gradient field values along the spatial dimension l sampled at $t = k\Delta t$. The recovery of the probes positions is achieved under an additional constraint,

$$\boldsymbol{G}_{tone}{}^{H}\boldsymbol{G}_{sequence} = \mathbf{0}, \qquad [29]$$

which requires that the tones be orthogonal to the imaging sequence's original gradient waveforms. To estimate $\boldsymbol{r}$ from Eq. [15] it is first left multiplied by $\boldsymbol{G}_{tone}{}^{H}$, resulting in the elimination of two terms according to Eq. [6, 16], and then solved for $\boldsymbol{r}$:

$$\boldsymbol{r} = \boldsymbol{G}_{tone}{}^{+}\boldsymbol{b}, \qquad [30]$$

where $\boldsymbol{G}_{tone}{}^{+} = \left(\boldsymbol{G}_{tone}{}^{H}\boldsymbol{G}_{tone}\right)^{-1}\boldsymbol{G}_{tone}{}^{H}$ denotes the Moore-Penrose pseudoinverse of $\boldsymbol{G}_{tone}$. Note that Eq. [30] differs from Eq. [20] in that it does not apply $\boldsymbol{\Psi}_{\mathrm{b}}{}^{-1}$ to optimize SNR, which would otherwise violate Eq. [29].

The orthogonality between foreground gradient activity and the tones can be achieved in various ways, for example by band-stop filtering the sequence gradient waveforms in the frequency domain around the tones frequencies. For optimal use of the gradient system capabilities, gradient tones need to be co-designed with the temporally overlapping gradient waveforms (**Figure 2**). System characteristics such as maximum gradient strength, slew rate and bandwidth need to be met jointly. In the present work, a spin-warp sequence was chosen for the image encoding and modified to incorporate 3 gradient tones at frequencies $f_x = 6\ kHz, f_y = 7\ kHz,$ and $f_z = 8\ kHz,$ with identical nominal amplitudes $A_x = A_y = A_z = 3.71\ mT/m$. In order to superimpose the tones within gradient specifications, the initial waveform's maximum gradient strength and slew rate were $19\ mT/m,$ and $40\ mT/m/ms,$ respectively, values well below the gradient system limitations of $31\ mT/m,$ and $200\ mT/m/ms$. In a second step, the waveform was band-stop filtered using MATLAB Release 2010a (The MathWorks, Inc., Natick, MA, USA). The band-stop filter was obtained in an equiripple FIR filter design using the MATLAB implementation of the Parks-McClellan algorithm. The desired tones frequencies

were adjusted slightly $(10 - 70\ Hz)$ to make them harmonics of the acquisition window and fulfill Eq. [19].
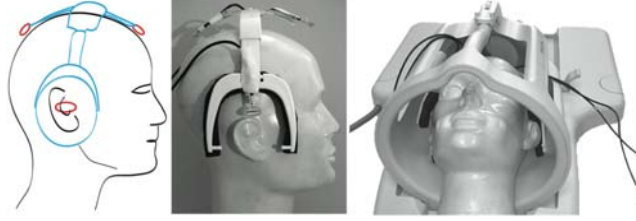
Figure 1: The motion correction setup as used in this work. It consists of an array of four 19F NMR field probes attached to a pair of slightly modified standard MR headphones. The probes are located approximately on the vertices of a tetrahedron for well-conditioned field monitoring and position tracking.

A closed-form solution for the rotation and translation parameters, $\boldsymbol{R}$ and $\boldsymbol{t}$, was derived by Umeyama (Umeyama 1991). It yields the optimal (in the least-squares sense) rotation and translation parameters considering the covariance between a set of updated probe positions and a set of reference coordinates:

$$\boldsymbol{R} = \boldsymbol{USV}^T, \boldsymbol{t} = \boldsymbol{m_y} - \boldsymbol{Rm_x}, \tag{31}$$

with

$$\boldsymbol{m_y} = \frac{1}{N}\sum_{i=1}^{N} \boldsymbol{y_i}, \boldsymbol{m_x} = \frac{1}{N}\sum_{i=1}^{N} \boldsymbol{x_i}, \tag{32}$$

$$\boldsymbol{UDV}^T = \frac{1}{N}\sum_{i=1}^{N} (\boldsymbol{y_i} - \boldsymbol{m_y})(\boldsymbol{x_i} - \boldsymbol{m_x})^T, \tag{33}$$

$$S = \begin{cases} diag(1,1,1) & if \det(\boldsymbol{UDV}^T) \geq 0 \\ diag(1,1,-1) & if \det(\boldsymbol{UDV}^T) < 0 \end{cases} \tag{34}$$

where $\boldsymbol{R}$ and $\boldsymbol{t}$ denote the rotation matrix and the translation vector that map the updated positions $\boldsymbol{y_1}, \dots, \boldsymbol{y_N}$ of N field probes to a set of reference positions $\boldsymbol{x_1}, \dots, \boldsymbol{x_N}$. $\boldsymbol{UDV}^T$ is the result of the singular value decomposition of the position covariance matrix.

The field probe data were processed directly on the MR system's spectrometer. Immediately after each data acquisition, the probes' positions were calculated according to Eq. [25] using the definition of $\boldsymbol{G_{tone}}^+$ as defined in Eq. [30] and compared to a set of reference coordinates obtained with gradient tones during the first interleave of the scan to determine the motion parameters as defined in Eq. [31]. For prospective motion correction the sequence was locked to the patient frame of reference by rotating all gradient waveforms, including the gradient tones, and shifting the RF center frequency prior to each slice excitation.
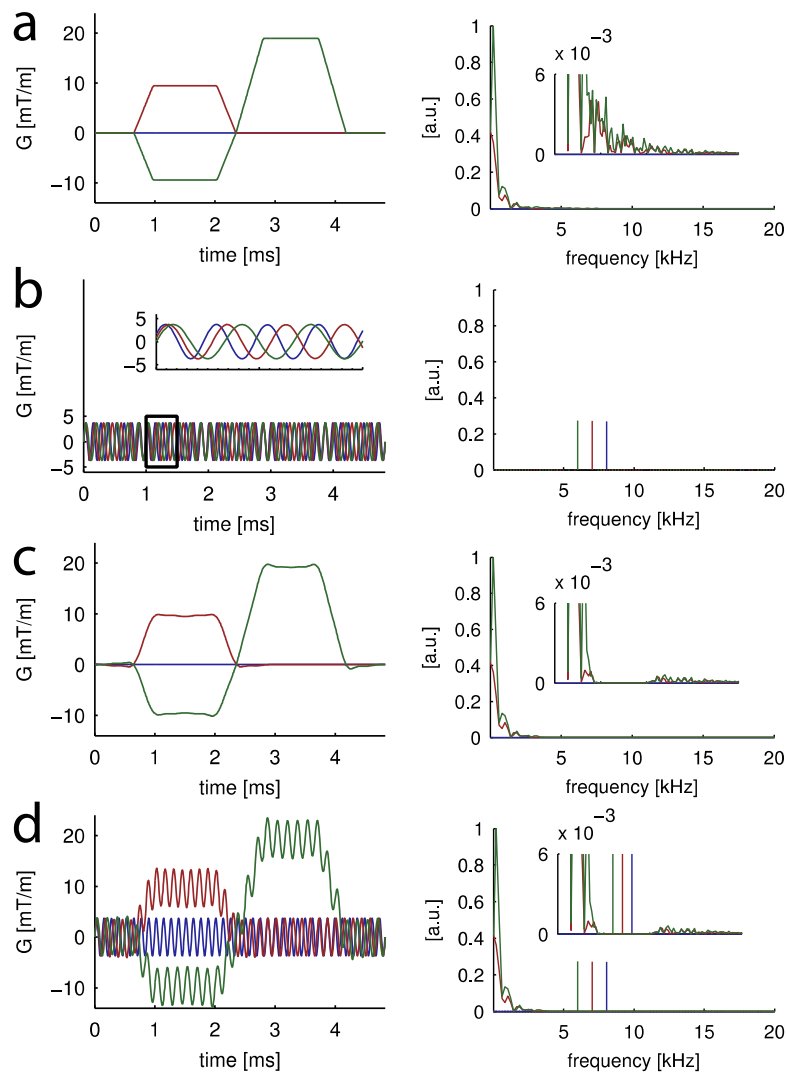
Figure 2: Co-design of the image encoding waveform and gradient tones. (2a) The starting point is the choice of the image encoding waveform, a spin-warp in this case. (2b) In a second step, 3 different frequencies are selected for the gradient tones. The choice has to consider the gradient system's transfer function, which linearly affects the method's sensitivity. (2c) In a third step, the spectrum of the image encoding waveform is filtered at or around the tones frequencies to orthogonalize the image encoding from the tones. To minimize the filter's effect on the image encoding in the time domain, it is beneficial for the gradient tones to lie in spare bands of the image encoding gradients' spectrum. The superposition of the two is depicted in 2d. The resulting waveform is capable to synchronously perform MR image encoding as well as field probe localization.

NMR field probe interface and operation

All experiments were done using NMR field probes as described in Refs. (De Zanche et al. 2008; Barmet et al. 2010). To avoid RF interference between the monitoring and the imaging experiment, perfluoropinacol-based ^{19}F NMR field probes were used with a droplet diameter of 1

mm and a Larmor frequency of 120.2 MHz. The probe sensitivity is reflected by the criterion ξ (De Zanche et al. 2008), which denotes the product of the probe SNR and the square root of the acquisition bandwidth. For the probes used in the motion correction experiment ($T_2^* = 4\ ms$) it amounted to $\xi = 7.9 \cdot 10^4 \sqrt{Hz}$. The signal characteristics of the probe used in the benchmarking measurements were $T_2^* = 9\ ms$ and $\xi = 8.1 \cdot 10^4 \sqrt{Hz}$. The field probes were connected to the spectrometer of a 3T Philips Achieva system, which was used for all experiments described in the following. The field probes were excited immediately before the start of the data acquisition with a hard excitation pulse (duration 5 µs, nutation frequency 50 kHz, power ≈ 5 W) triggered by separate hardware. The custom-built hardware interface included separate excitation chains, preamplifiers and booster stages as well as PIN diode switches for independent transmit-receive operation (Barmet et al. 2009).

Data Acquisition

Gradient response and calibration

To obtain the coupling coefficients, a single NMR field probe was rigidly attached to a homemade acrylic glass (PMMA) scaffold placed inside the bore of the MR system. The experiment consisted of 255 repetitions of a gradient sequence consisting of 3 synchronous tones and was performed for 4 different positions of the NMR field probe, forming approximately a tetrahedron. The tone frequencies were $f_x = 6\ kHz, f_y = 7\ kHz$, and $f_z = 8\ kHz$, with nominal amplitudes $A_x = A_y = A_z = 3.71\ mT/m$. The acquisition bandwidth was $439\ kHz$, the time window used for the localization was $4.8\ ms$ and $T_R = 100\ ms$. The reference coordinates used in Eq. [26] were determined by measuring the field probes' NMR frequency shifts under static gradients of $2.5\ mT/m$ in the x, y and z directions, respectively (Dumoulin, Souza, and Darrow 1993).

Performance of probe localization and rigid-body tracking

To assess the performance of tone-based field probe localization and rigid-body tracking, accuracy and precision measurements were performed using the same experimental setup as for the gradient response calibration experiment. One field probe was placed at two opposing ends of the field of view (start and end position) and both tones-based localizations as well as reference position measurements were performed at each position using the same tones frequencies, amplitudes, acquisition bandwidth, T_R and time window as in the previous experiment. The probe's reference coordinates were obtained by measuring its NMR frequency

shift under three sequential static field gradients (Dumoulin, Souza, and Darrow 1993). The reference experiment was repeated 20 times for both positions in order to estimate its sensitivity as well as controlling for undesired minute probe displacements. Positions obtained from both methods were compared for consistency (root-mean-square discrepancy) and their precision (standard deviation) was computed. Additionally, the precision was predicted with Eq. [22]. The field probe was then moved by hand from the start to the end position while the tones-based tracking sequence was running. Finally, the effect of field coupling on the tones-based localization was quantified by computing the probe coordinates with a purely diagonal system response matrix C and comparing with probe coordinates computed using the full system response obtained in the previous experiment. The matrix elements used in this case were obtained from a single calibration measurement at the start position, as opposed to the 4 positions required for the previous case.

To estimate error in rigid-body tracking, the stationary calibration setup was used for 255 successive instances of determining translation and rotation parameters in the absence of motion.

Motion correction experiments

The field probe array was mounted on a pair of standard MR head phones to perform the prospective motion correction experiment. The only two modifications to the headphones were the removal of the housing around the ears to maximize freedom of motion and the attachment of a short beam orthogonal to the frame connecting the two sides (**Figure 1**). Both functions of the field probe array, field monitoring and the determination of head orientation, are well conditioned if the field probes are placed at the vertices of a tetrahedron. The field probe arrangement was chosen accordingly. Comprising 4 field probes, the headphone setup can readily be used for gradient system response calibration when the head setup is stationary. This was achieved by rigidly placing it in the center of the MR system's field of view. Fixation was achieved by attaching the setup to a static spherical water phantom.

In the in vivo experiment, a healthy volunteer was equipped with the headphone setup and put into the MR system. In the phantom experiment, the head setup was taped to a structured water phantom that was rigidly placed inside the MR system. All experiments in this section, i.e. the calibration, the phantom, and the motion correction experiments, were done using an 8-channel Philips SENSE head coil. An RF-spoiled T_1-weighted multi-slice gradient echo sequence was chosen with the following parameters: field of view 23 cm, resolution 0.9 mm, 7 axial slices, slice

thickness 5 mm, TR = 40.1 ms, flip angle 80° and total imaging time = 71 s. The tones frequencies, amplitudes, acquisition bandwidth and time window were identical those of the previous experiments.

Five phantom experiments were conducted: In the first phantom experiment, the setup was put in position 1 and the imaging sequence was played out twice, once with sequence update based on motion tracking and once without update to assess potential image artifacts induced by the tracking system. In the second phantom experiment, sequence update was again suppressed and the imaging sequence was played out without the gradient tones to assess their potential impact on image quality. In the third experiment the imaging sequence including tones was played out without sequence update to obtain a reference trajectory for calibrated image reconstruction. In the fourth experiment, sequence update was performed during repeated imaging under the influence of motion. In the first repetition, an image was obtained while the setup was stationary at position 1. The phantom was rotated by hand about the z-axis to position 2 in the second repetition, followed by a third repetition in which a second image was taken again in stationary conditions. For the fifth experiment the setup was left stationary in position 2 and imaged without sequence update to illustrate the actual position change. Reference probe coordinates were acquired prior to the first experiment for position 1 and after the fourth experiment for position 2.

Two in-vivo experiments were carried out as follows: In the first the volunteer was asked to perform a head rotation around the magnet's main axis and then return to the initial position. In the second one the volunteer was asked to perform a shift along the magnet's main axis orthogonal to the imaging slice, also returning to the initial position. Both scenarios were performed twice with and with without motion tracking, respectively.

Field monitoring and image reconstruction

Dynamic magnetic fields of 0th and 1st spatial order were computed from the same field probe data as used for slice tracking and a set of reference positions and static off-resonance frequencies acquired at the beginning of the scan session. In the experiments with motion correction, 2D image reconstruction was done based on the concurrently monitored dynamic field data with an iterative conjugate-gradient algorithm using gridding. Note that the concurrently monitored dynamic fields are inherently measured in the subject's frame of reference (**Figure 6**, right-most column). In the experiments without motion correction, image reconstruction was done based on a previously monitored k-space trajectory of 0th and 1st spatial order. Phase evolutions in the object caused by the tone orthogonal to the imaging slice

were a function of the time-dependent off-center position of each slice and were taken into account throughout.

Results

Gradient response and calibration

Table 1 shows the gradient system response matrix. The desired field components along each axis amounted to 0.66 (G_x, 6 kHz), 0.59 (G_y, 7 kHz), and 0.53 (G_z, 8 kHz), respectively. The cross-term magnitudes were naturally much smaller, ranging between $4.7\cdot10^{-4}$ and $6.9\cdot10^{-3}$. The phase values of the diagonal elements were determined with precisions around 0.014º. The phases of the small cross-terms could not be determined with high precision and are hence put in brackets. In order to compare contributions of field terms of different spatial orders the elements were normalized such that they reflected field values on a sphere around the gradient isocenter with a diameter of 20 cm.

Performance of probe localization with gradient tones

The left-hand column of **Figure 3** shows the standard deviations (SD) of the probe localization measurement and their theoretical predictions in the absence of sequence gradient activity. The gray horizontal lines denote the sample SD of the data points plotted by the green (x), red (y), and blue (z) dots. The shaded areas reflect predicted SD for each interleave (not of the measured sample). The measured SD amounted to 25 µm (x), 35 µm (y), and 41 µm (z). The predicted SDs were consistent with the measured ones and amounted to 24 µm (x), 31 µm (y), and 40 µm (z). The probe's SNR used for the predictions is illustrated at the top of **Figure 3**. The right-hand column in **Figure 3** shows both the measured (gray line) and the predicted (gray area) SD in the presence of the imaging sequence. As can be seen by the shape of the gray area and the probe's SNR at the top, the predicted sensitivity reflects the dependence on the applied phase encoding gradient, whose 0th-order moment defines the field probe's SNR as illustrated at the top of **Figure 3**. Note that the measured precision reflects the sample's SD whereas the gray area reflects the predicted SD for each time point. Also note that the sample noise is free of systematic errors that could have been induced by incomplete separation between tones and sequence gradient waveforms, for example.

Figure 4 shows the coordinates of the probe as it was moved from the start to the end position. The insets at the start position show very good agreement between the tones coordinates and the reference coordinates. The root-mean-square (RMS) and maximum (max) difference between the positions obtained with tones and the reference positions amounted to 33 µm (x,

RMS), 151 µm (x, max), 33 µm (y, RMS), 233 µm (y, max), 42 µm (z, RMS), and 251 µm (z, max). The RMS difference between the two methods at the end position amounted to 583 µm (*x, RMS*), 771 µm (x, max), 595 µm (*y, RMS*), 822 (y, max) and 131 µm (*z, RMS*), and 358 µm (z, max). The RMS error of the coordinates at the end position computed with the simplified system model, which disregards both the off-diagonal elements of C and the vector c_0, amounted to 480 µm (*x*), 2.53 mm (*y*), and 2.66 mm (*z*), respectively.

The subsequent experiment concerning the consistency of rigid-body parameters in the absence of motion yielded standard deviations of translation of 13 µm (x), 20 µm (y), and 25 µm (z) with maximal excursions of 55 µm (x), 83 µm (y), and 114 µm (z) and standard deviations of rotation of 0.01° (x), 0.009° (y), and 0.01° (z) with maximal excursions of 0.031° (x), 0.025° (y), and 0.038°.

Motion correction experiments

Phantom imaging

Figure 5a-c show the phantom in position 1 as obtained in the first phantom experiment. The image in **Figure 5**b was reconstructed with concurrently monitored dynamic field data and the image in **Figure 5**c with the reference trajectory. The result of the second phantom experiment is illustrated in **Figure 5**(d,g). **Figure 5**d shows the image acquired without gradient tones and **Figure 5**g its difference to the image acquired with tones, which is very minor in the range of a percent. The image artifacts induced by the tracking system are illustrated in **Figure 5**f, showing small artifacts at the edges and a clear image background with very subtle ghosting. Concurrent dynamic field monitoring reduces these artifacts, as illustrated in **Figure 5**e. The results from the fourth phantom experiment are illustrated in **Figure 5**(i,k,m,n). **Figure 5**m shows the residual difference between the image data obtained at positions 1 and 2 with motion tracking and image reconstruction based on concurrent field monitoring. **Figure 5**n shows the same data but reconstructed with the reference trajectory. The residual differences in the order of a few percent reflect changes in transmit and receive B_1 fields due to the altered geometric relationship between the phantom and the coils. The actual rotation of the setup amounted to approximately 11.2 degrees and is illustrated in **Figure 5**h and **Figure 5**l (difference image).
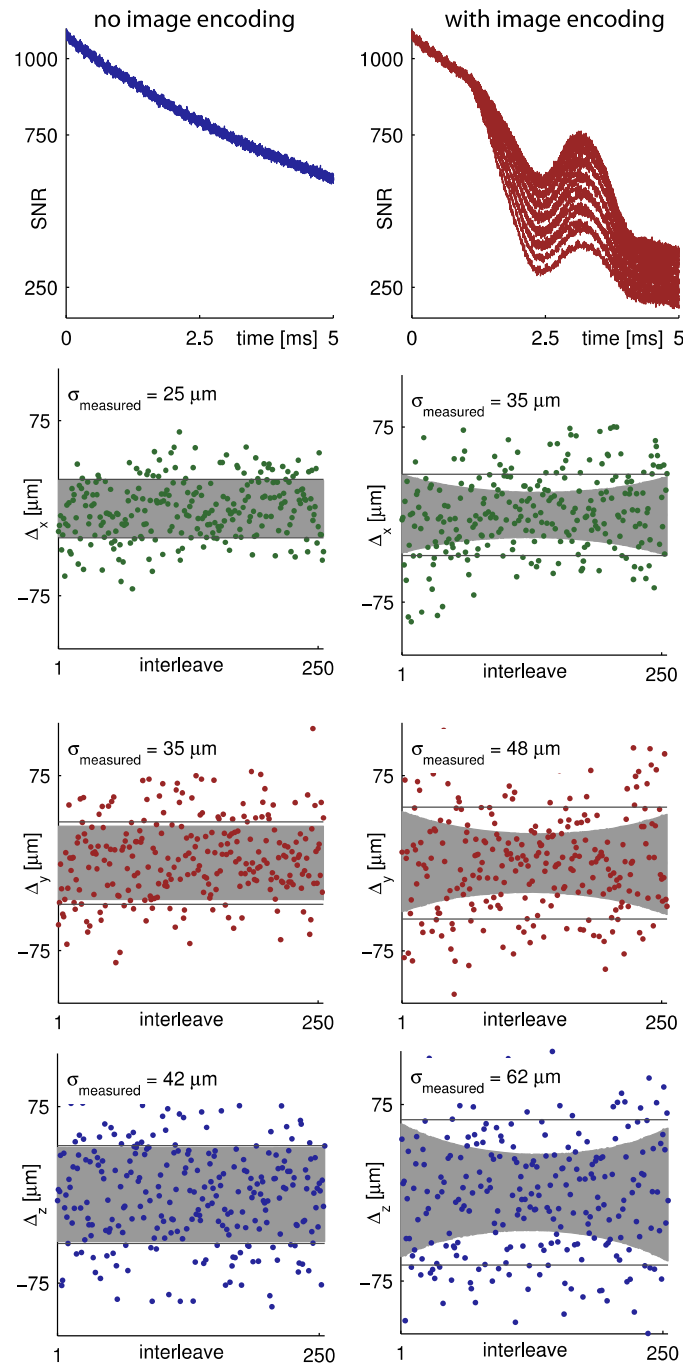
Figure 3: Left column: SNR (top) and sensitivity of tones-based probe localization without image encoding for the x (green), y (red), and z (blue) axis. The difference between the standard deviation of the sample and the prediction is below the figure's pixel resolution. The largest outliers are not shown due to scaling and amounted to 69 μm (x), 115 μm (y), and 129 μm (z). Right column: SNR and tones-based localization sensitivity during a spin-warp image encoding. The prediction (light gray) shows an interleave-dependence (interleaves 1 and 255 are farthest out in k-space, interleave 127 crosses the k-space center). The gradient system's transfer function renders the sensitivity frequency dependent, which is reflected in different precisions for each spatial dimension. The largest outliers in the right-hand column are not shown due to scaling and amounted to 111 μm (x), 220 μm (y), and 180 μm (z).
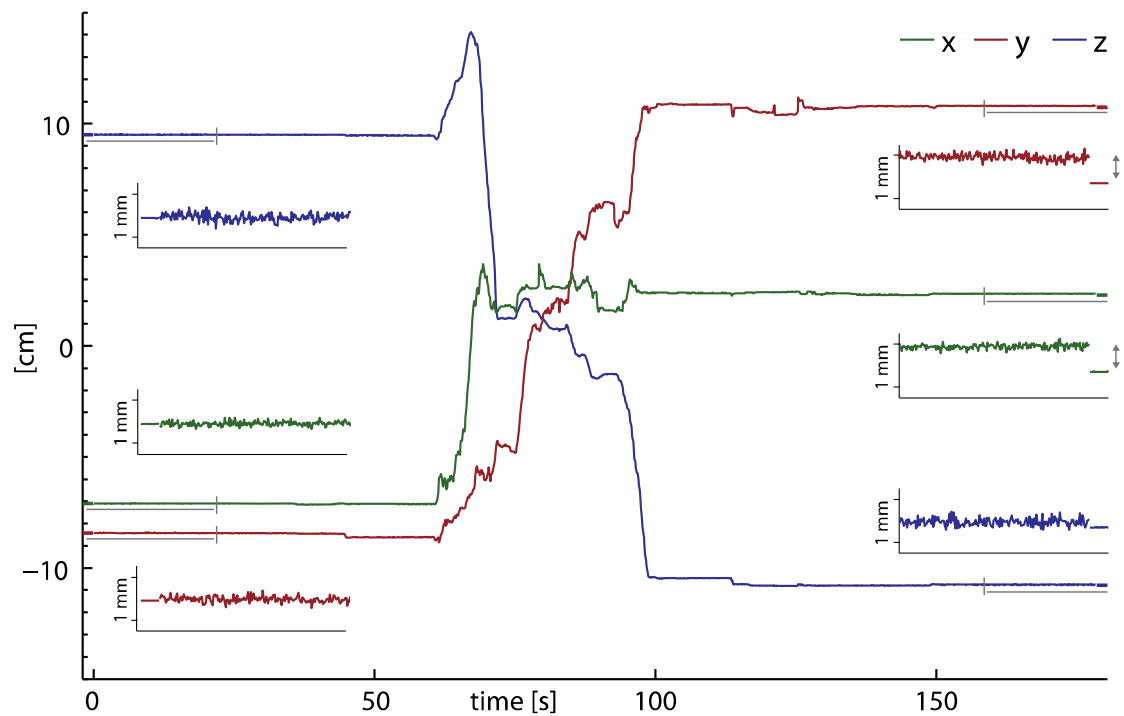
Figure 4: Localization of a moving NMR field probe with gradient tones. The field probe was moved from a start position to an end position during a gradient tones sequence. At t = 0 s, the 20 reference position measurements, indicated in the close-up plots on the left-hand side, are consistent with the positions obtained with gradient tones. At the end position at around t = 170 s, the discrepancy between the 20 reference position measurements and the tones-based positions amounts to 583 µm (x), 595 µm (y), and 131 µm (z), respectively. The insets illustrate data from the first 20 s (left-hand side) and last 20 s (right-hand side) of the experiment, respectively.

In-vivo imaging

Figure 6(a-b) shows the rotation and translation parameters observed in the in-vivo experiment targeting in-plane rotation. The prescribed rotation around the magnet's main axis (*z*) is visible in the leftmost column. Translation along the y-axis shows that the prescribed head rotation was performed as a rolling motion, which is reflected in a rotation-correlated shift of the head's center of mass. Motion in the case where motion correction was applied is illustrated in **Figure 6**b and is in good agreement with both the prescribed rotation and the motion in the control experiment.

The right hand side in **Figure 6**a shows the k-space trajectory of one slice as monitored by the field probe array during the same experiments. The corresponding case with sequence update is illustrated in **Figure 6**b. Correction of the head motion by sequence update resulted in parallel phase encoding lines. It can further be seen that the tones amount to small deviations from the underlying Cartesian k-space sampling pattern yet do not cause violations of the Nyquist

sampling criterion throughout the k-space area used for image reconstruction. The slight compression of the tone pattern around k_x = ± 3.5 rad/mm reflects ramping of the readout gradient.

Figure 6(c-f) shows the resulting reconstructed images. Without correction all 7 slices are corrupted by motion artifacts (**Figure 6**c, **Figure 6**d). **Figure 6**e and **Figure 6**f show the effect of motion correction, which removed virtually all motion artifacts. There are no ghosting artifacts, which is reflected in the clear background of the scaled images. In the scaled images, residual blurring is still apparent at the edges of the head and flow artifacts are visible along the phase encoding direction. Please see **Figure 7** for a close-up view of two selected slices.

For the in-vivo experiment with deliberate translation the observed Euler angles and translation are shown in **Figure 8**a,b. The prescribed shift along the magnet's main axis (*z*) is shown in the right-hand column of **Figure 8**a,b and amounted to ± 1 cm. The left-hand columns of **Figure 8**a,b illustrate that the shift was accompanied by a small correlated rotation around the y-axis (red graph). Motion in the corrected and the non-corrected case was in good agreement.

Figure 8c,d show image reconstructions for two slices without motion correction, again exhibiting severe motion artifacts. **Figure 8**e and **Figure 8**f, respectively, show the corresponding results with motion correction.

Figure 9 shows a comprehensive comparison of the different correction options. **Figure 9**(a-d) illustrate their effect on image quality for the prescribed in-plane rotation (top row). **Figure 9**a depicts a slice from the in-plane rotation experiment for which neither field monitoring nor prospective motion correction was applied. **Figure 9**b shows the same slice reconstructed with field monitoring data, which successfully corrects the in-plane motion. **Figure 9**c illustrates that prospective motion correction without field monitoring also yields a good result that was not further visibly improved by applying field monitoring, as illustrated in **Figure 9**d. The only visible difference between **Figure 9**c and **Figure 9**d is a slight rotation, which is due to reconstruction in two different coordinate systems.

Figure 9(e-h) illustrate the effect of the different motion correction options in the experiment with prescribed through-plane motion. **Figure 9**(e,f) show that the image is corrupted by motion artifacts when no prospective motion correction is applied. **Figure 9**f illustrates that field monitoring alone is not effective at addressing through-plane motion. **Figure 9**g shows that prospective motion correction alone is effective at reducing the artifacts due to through-plane motion seen in **Figure 9**e. **Figure 9**h, finally, shows the effect of additionally performing field monitoring, yielding no visible difference in image quality compared to **Figure 9**g. Again, as in

Figure 9(c,d), the only visible difference between **Figure 9**(g,h) is a rotation due to reconstruction in slightly different coordinate systems.
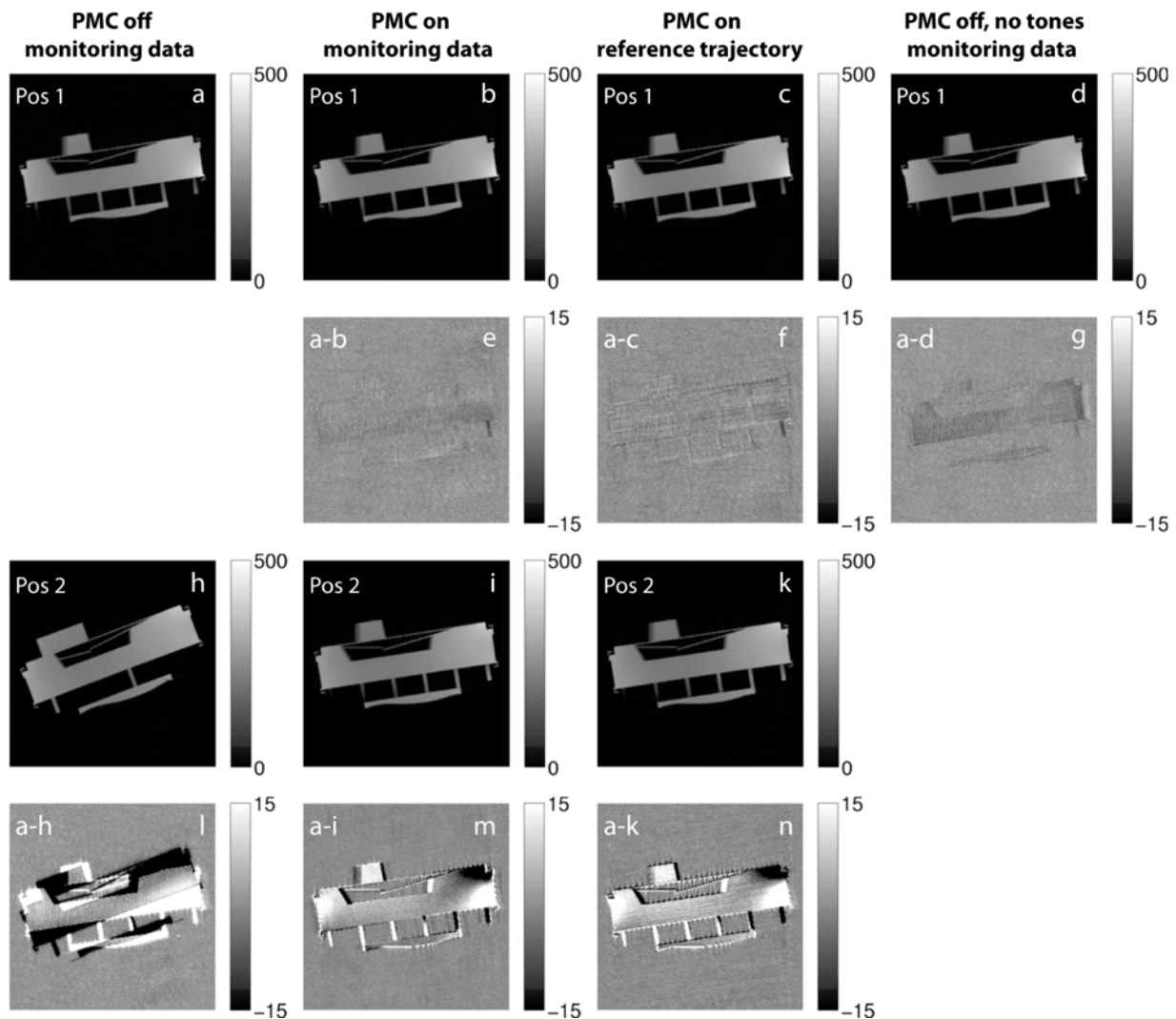

Figure 5: Image reconstruction of the phantom experiments: (a-c) image quality of the stationary phantom in position 1 without motion updates (a), and with motion updates with two different reconstruction methods (b,c). Difference images are shown in (e,f), illustrating the image artifacts induced by the tracking system (f), which is successfully corrected with field monitoring in the head frame (e). (d,g): image reconstruction (d) and difference image (g) for an imaging readout without gradient tones, illustrating their effect on image quality. (i,k,m,n): image reconstructions of the phantom in position 2 with motion correction with concurrent field monitoring-based (i) and reference-trajectory based reconstruction (k). Corresponding difference images are shown in (m,n). A view of the phantom in position 2 is shown in (h) and the difference to the phantom in position 1 is shown in (l).
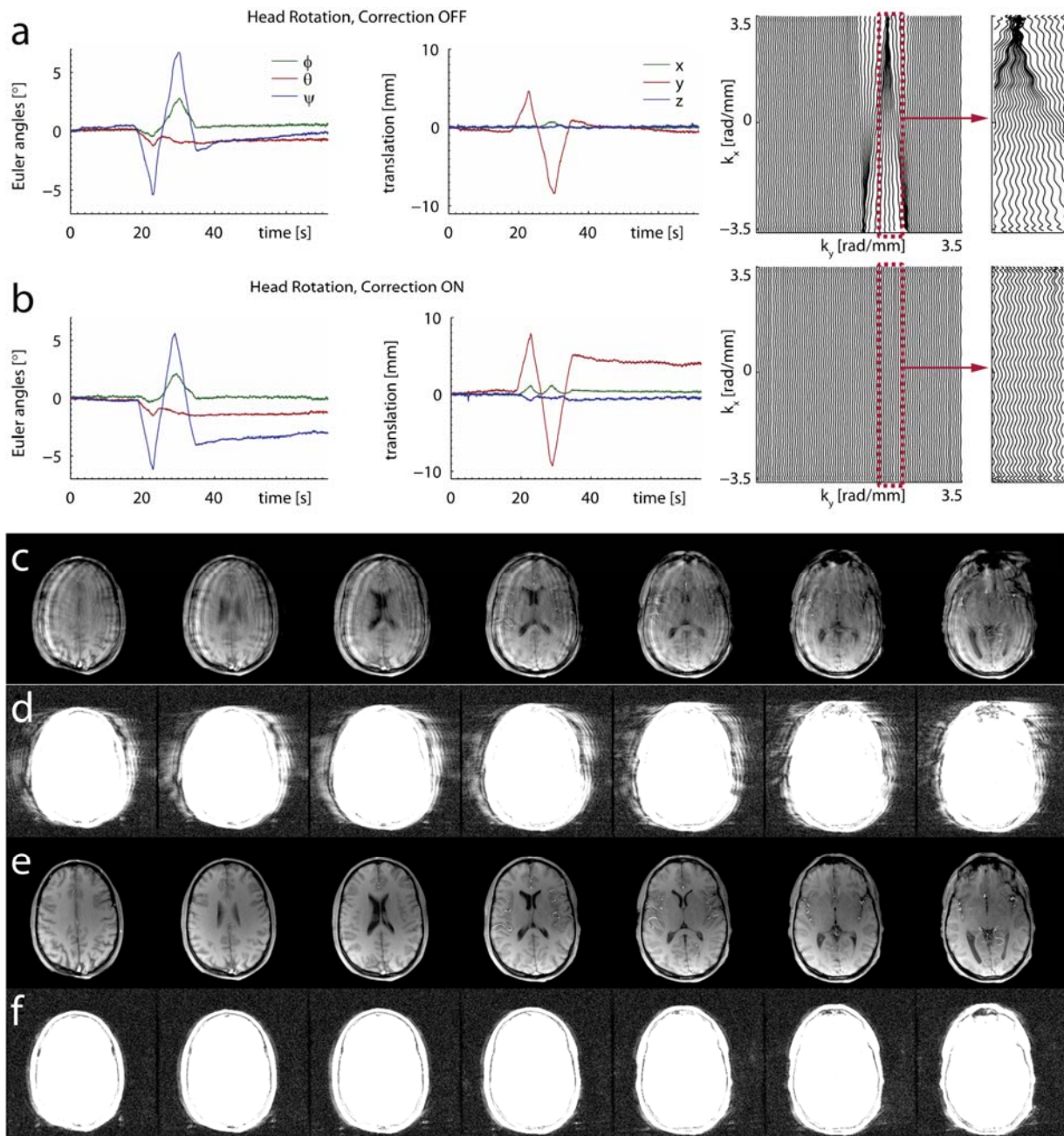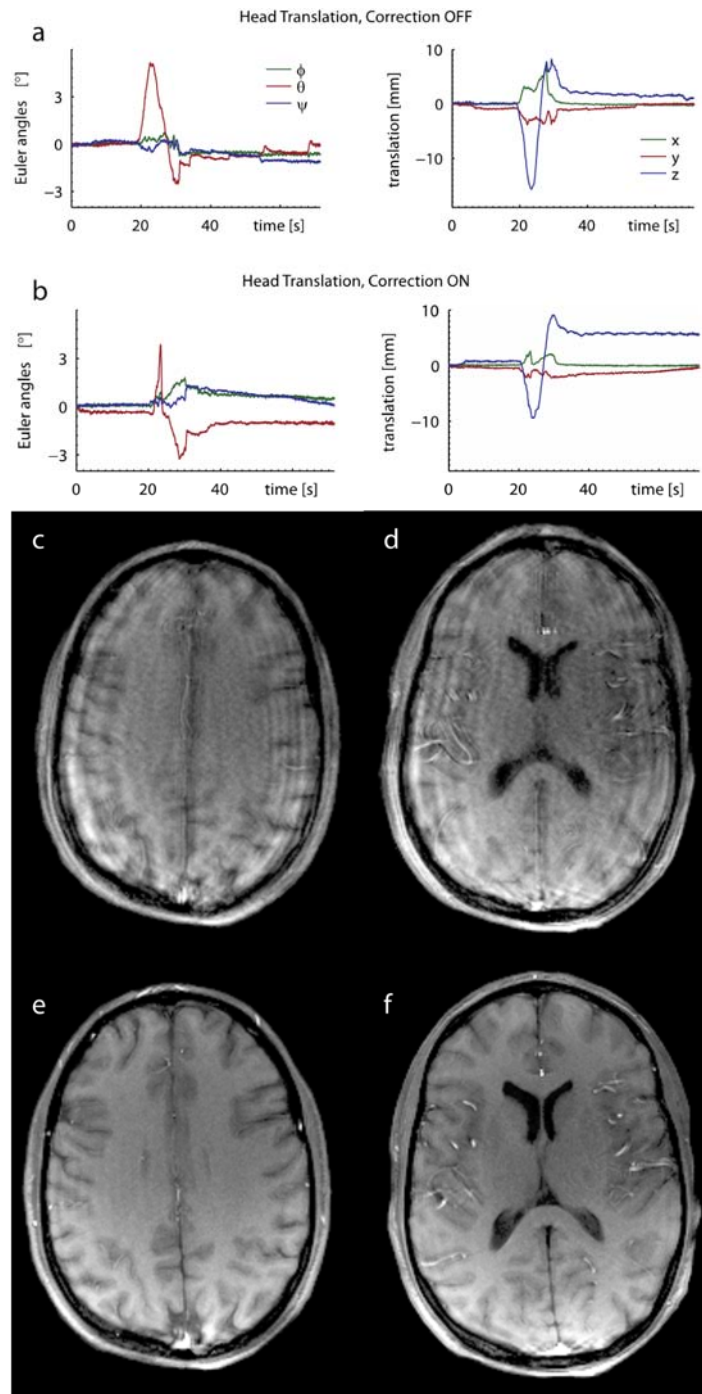
Figure 6: (a-b) Euler angles and center of mass translation of the in vivo rotation experiment in the uncorrected (first row) and in the motion corrected case (second row). The rotation around the z-axis (blue graphs) was reproduced in both scans and the shift along the y-axis (red graphs) shows that the prescribed head rotation was actually a rolling motion. The right-hand columns show the concurrently monitored k-space trajectory in the head frame of reference in the in vivo experiments. The overviews show the trajectory during the prescribed in-plane rotation where sequence update was performed (second row) and in the case of no update (first row). The close-ups show the amplitudes of gradient tones, which amounted to 0.5 Nyquist in the phase encode direction. In the motion corrected case, subtle residual deviations from the reference trajectory resulted in slightly non-parallel encoding lines. In the uncorrected case, the rotation caused very strong distortions of the k-space sampling. The gradient trapezoid's ramp at the beginning and the end of each readout line causes denser sampling at the corresponding k-space positions. (c-f) Image reconstruction in the case of in-plane rotation. All 7 slices

are heavily corrupted by motion artifacts, as shown at both the linear (c) and the power scale (d). Tones-based slice tracking enables image reconstruction free of conspicuous motion artifacts (e); small residual artifacts are observed at the power scale (f).
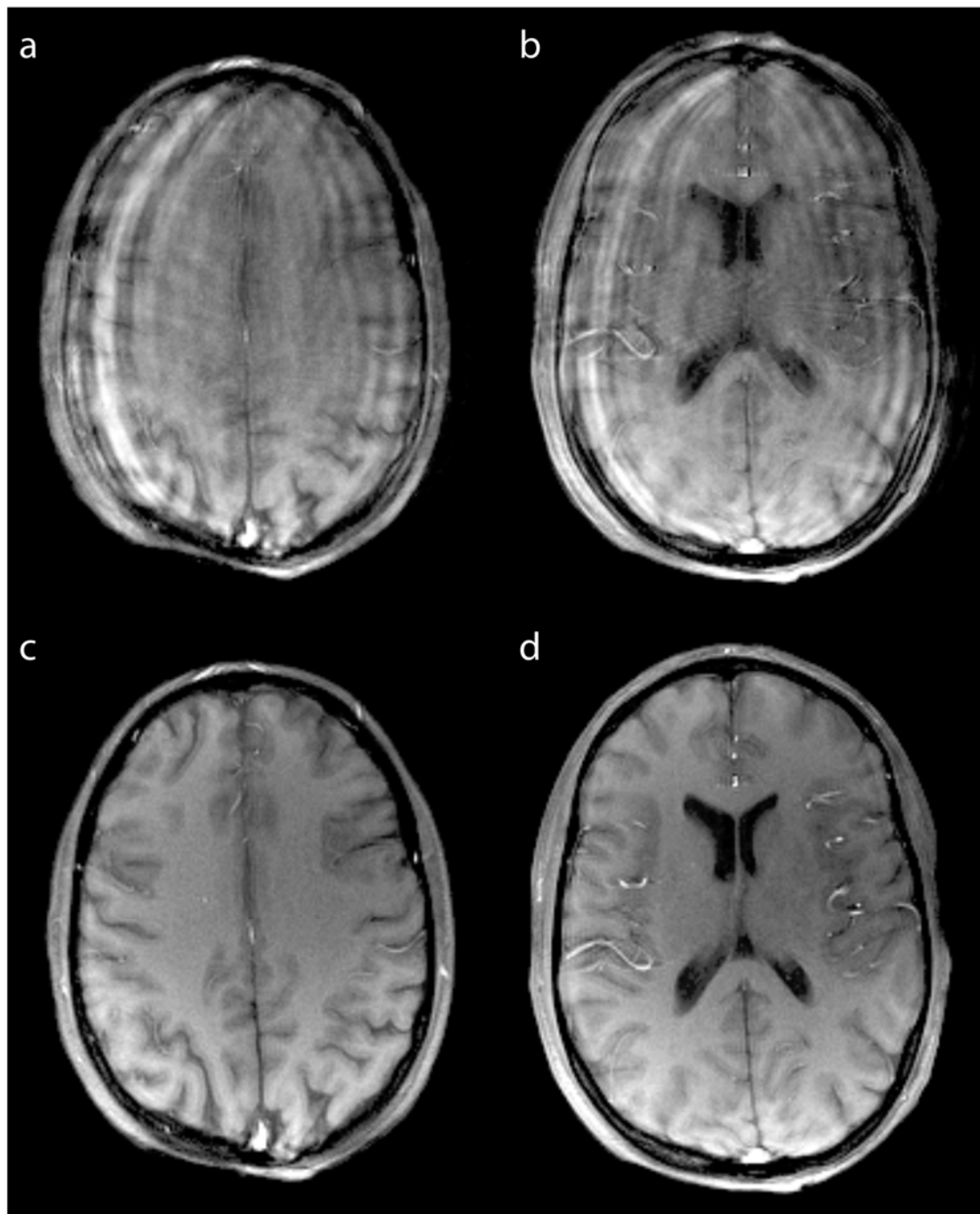
Figure 7: Image reconstruction in the in-plane rotation experiment. 2 out of 7 slices are shown. In the uncorrected case (a, b), severe motion artifacts remain in the reconstructed image whereas motion correction and field monitoring successfully remove them (c, d).

Figure 8: (a-b): Euler angles and center of mass translation of the in vivo translation experiment in the uncorrected (first row) and in the motion corrected case (second row). The prescribed shift along the z-axis is very similar between the two experiments (right, blue graphs). The associated rotation around the y-axis (left, red graphs) refers to a subtle nodding motion during the shift. (c-f): Image reconstruction in the through-plane shift experiment. 2 out of 7 slices are shown. In the uncorrected case (c, d), severe motion artifacts remain in the reconstructed image whereas motion correction and field monitoring successfully remove them (e, f).
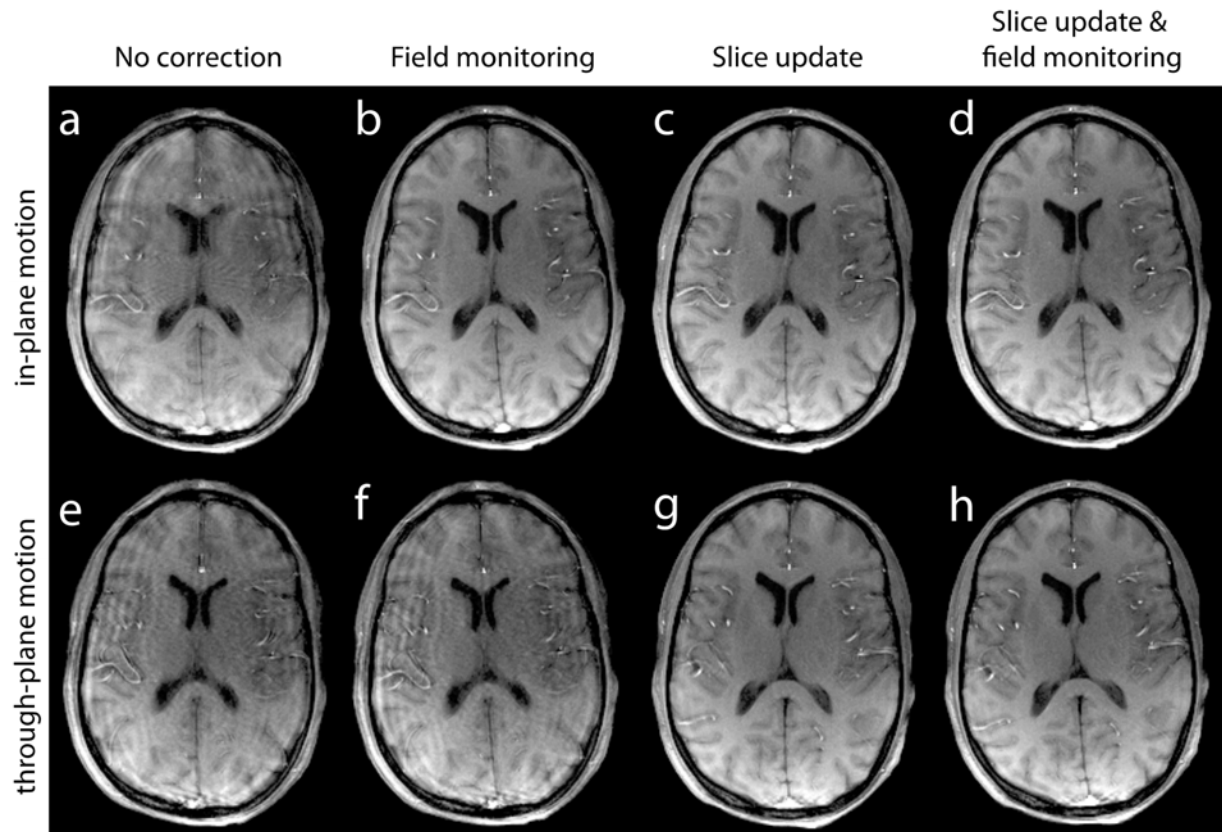
Figure 9: Comparison of different motion correction methods: In-plane rotation (top row): (a) Severe image artifacts occur if neither field monitoring nor prospective motion correction is used. (b) Field monitoring alone successfully corrects for in-plane motion, which was also achieved by slice updates and image reconstruction with the reference trajectory (c). Field monitoring did not visibly improve image quality in the prospective motion correction experiment (d). Through-plane motion (bottom row): Severely corrupted image if no motion correction is used (e). Field monitoring alone is not able to correct for through-plane motion (f). Successful motion correction with tones-based sequence updates (g). Field monitoring did not further improve image quality in the motion correction experiment (h). The only visible differences between (c,d) and (g,h), respectively, are image rotations due to their reconstruction in different coordinate systems.

		Measured Responses						
		G_x		**G_y**		**G_z**		**B_0**
		$\lvert\cdot\rvert$	Φ	$\lvert\cdot\rvert$	Φ	$\lvert\cdot\rvert$	Φ	$\lvert\cdot\rvert$	Φ
Applied Tones	**G_x (6 kHz)**	**0.66**	-11°	$9.0\cdot10^{-4}$	(-147°)	$3.0\cdot10^{-3}$	(-75°)	$1.0\cdot10^{-2}$	(104°)
	G_y (7 kHz)	$1.4\cdot10^{-3}$	(-62°)	**0.59**	-2°	$4.7\cdot10^{-4}$	(-103°)	$5.8\cdot10^{-3}$	(25°)
	G_z (8 kHz)	$1.0\cdot10^{-3}$	(110°)	$1.4\cdot10^{-3}$	(-18°)	**0.53**	7°	$6.9\cdot10^{-3}$	(31°)

Table 1: Gradient system calibration matrix.
As expected, the magnitude ($\lvert\cdot\rvert$) of the desired field components (bold) decreases with increasing frequency. The coupling coefficients were determined with a magnitude precision between $1\cdot10^{-4}$ and $3\cdot10^{-4}$ and the magnitude-dependent phase (Φ) precision of the diagonal elements amounted to 0.014°. The phase precision of the low-magnitude off-diagonal elements was naturally lower and hence mentioned in brackets.

Discussion and Conclusion

The results of this work show the successful implementation of gradient tones as a method to encode the position of NMR field probes, reaching precisions of 35-62 μm according to standard deviations observed in a stationary setup. The proposed solution enables the position tracking of field probes without any extra scan time and without line-of-sight access. Furthermore, it does not disturb the steady-state of the object under investigation. It is shown that the combination of gradient tones and an array of 4 NMR field probes in a rigid body configuration allows synchronous real-time motion tracking and sequence monitoring in vivo. If desired, the 4-probe array used in this work allows for complementary field monitoring of 0th- and 1st-order dynamic fields in the head frame of reference.

These benefits come at the expense of additional hardware and software requirements. For this study, a suitable headset and transmit/receive hardware were built based on ^{19}F field probes and interfaced to a commercial spectrometer for concurrent ^{19}F and ^{1}H acquisition. Due to the proximity of ^{19}F and ^{1}H Larmor frequencies such dual operation will amount to mere software changes on many receiver platforms. Nevertheless it requires dedicating four receiver channels to the motion correction task. Add-on software was also written for the calculation of tone-enhanced gradient waveforms, for real-time probe-data analysis and sequence update, and for non-Cartesian image reconstruction based on field probe data.

The proposed method serves two purposes. It enables sequence update by encoding the head position and orientation in six degrees of freedom and, optionally, performs field monitoring in the head frame of reference. As shown in this work, field monitoring is inherently able to perform motion correction on its own if the motion is in-plane and causes only small Nyquist violations. With prospective motion correction, however, field monitoring did not visibly improve image quality. This suggests that undesired field perturbations and residual within-TR motion were negligible in the case studied. Field monitoring is expected to help, however, in applications where field perturbations of technical or physiological origin are significant. Problems of this kind have previously been described for anatomical imaging and functional MRI (fMRI) at 7T (Versluis et al. 2010; Van de Moortele et al. 2002) and have successfully been accounted for with field monitoring (Wilm et al. 2011; Signe Johanna Vannesjo, Barmet, et al. 2012; Klein et al. 2013; Kasper et al. 2014).

The head setup used for head position tracking in this work relies on a rigid relation among the field probes and between the field probe array and the head, an issue all current marker-based approaches have in common. In this work, we addressed it by designing the head setup such as

to be both rigid and very light. It was operated without padding, which might have exerted confounding forces on the headset. For the presented method to be feasible it was also important that the head coil used permitted suitable cable routing, which may require hardware integration in very dense, closed receiver arrays.

The frequency of the sequence update was locked to the sequence's TR and amounted to 25 Hz, sufficient for the bandwidth of the head motion present in this work. In order to embed prospective motion correction into sequences with shorter TR, the tracking can be decoupled from the sequence timing and the motion can be extrapolated. In order to encompass motion with higher bandwidth, the field probes will need to be re-excited after shorter time intervals and hence require a shorter T_1.

The moderate duty cycle of the sequence used in this work allowed both field monitoring for each readout and full T_1 recovery within one TR. However, sequences that offer no such benign duty cycle limit the application of field monitoring in the current implementation. A generic way of overcoming this limitation will be continuous field monitoring (Dietrich et al. 2011), which provides field monitoring completely independent of sequence duty cycle and timing.

The choice of the probe dimension (1 mm diameter), time window (4.8 ms), image resolution (0.9 mm), as well as nominal tones amplitude (5 mT/m) and frequencies (6 kHz, 7 kHz, and 8 kHz, respectively) resulted in a localization precision of 35-62 µm. This is sufficient for typical applications that suffer from motion because of their target image resolution. Increased precision can be achieved according to the following trade-offs: If one chooses to boost probe SNR by increasing its diameter, the sensitivity will scale strongly with the probe diameter at a linear cost in maximum image resolution. Alternatively, one can choose to prolong the probe acquisition time and increase the sensitivity by a square root of time factor. Finally, one could increase the tones' localization power by scaling the nominal tones amplitude or decreasing their frequencies. Scaling up the gradient amplitudes causes a linear increase in sensitivity but comes at a linear expense of available gradient strength and slew rate available for image encoding. Decreasing the tones frequencies has several effects. It increases sensitivity according to the gradient impulse response function, whose magnitude response is relatively steep at the frequencies considered in this work (Signe J. Vannesjo et al. 2013). The results of the precision measurements showed a 44% increase (from 62 µm to 35 µm) in precision when the frequency was reduced by 2 kHz (from 8 kHz to 6 kHz). Also, lower tones frequencies increase the available slew rate for image encoding but also linearly increase the maximum k-space deviations from the underlying sampling pattern. Finally, the localization sensitivity will generally be somewhat reduced upon the onset of probe signal dephasing induced by image

encoding gradients. It was found that the prediction of the position SD based on the probe's time-dependent SNR corresponded very well with measurements and may thus serve to roughly predict localization performance.

The results of the accuracy experiment show that the RMS localization error amounted to about 600 µm per axis for a position far away from calibration points, reflecting different possible model violations. One main reason is a discrepancy between gradient field shapes at the tones frequencies and zero frequency, respectively. The system response model used in this work considers field terms up to first spatial order, but it has been shown previously that spatially non-linear dynamic fields do occur (Wilm et al. 2011). To address these, higher-order tone field characterization could be incorporated in a calibration step involving more than the four positions. This would change the calibration model to one in which the measured tone response reflects a curvilinear coordinate system whose coefficients could be computed in the same way as for linear coordinates. Importantly, higher-order calibration would not affect the number of probes required in the headset. Gradient systems that are linear and time invariant will permit reusable one-time calibration. A second model violation is caused by concomitant fields. Negligible for high main field strengths as used in this work, it may become a relevant source of error at lower fields. Note, however, that it is possible to predict the concomitant fields to a high degree by using information about nominally known gradient waveforms. The extended field model resulting from these considerations will be non-linear and will have to be addressed in future work.

A central aspect that also needs further investigation is the optimal embedding of probe localization capability into arbitrary gradient waveforms. In this work, sinusoidal tones were used because they permit simple response characterization, are robust against low frequency field contaminations, and can be placed in arbitrary time windows. Their placement is only limited by the practical need to avoid saturation of the probe receive chains during ^{1}H RF excitation and excessively fast probe dephasing, e.g., during strong spoiler gradients. Tones are linearly independent, easy to orthogonalize, and of high power for high tracking precision within short time intervals. Also, if applied on top of an image encoding gradient waveform, they impose small excursions on the k-space trajectory. Nonetheless, they need to be implemented such that these excursions are coordinated to avoid k-space gaps larger than the Nyquist limit. This was readily achieved in the sequence used in this work but may require further consideration in other cases. The separation between the sample sequence and the tones was rather straightforward because the former contained only small frequency components in the tones' frequency band. This situation will be different, e.g., for spiral and EPI trajectories with substantial spectral

content in the kilohertz range. For these, it is promising to use their native high-frequency components directly for probe localization provided that it encompasses sufficient energy for precise localization. To enhance sensitivity, it is conceivable to use entire frequency bands for localization, which will require additional considerations for calibration and signal processing.

Prospective motion correction with NMR field probes using the intrinsic high-frequency content of gradient waveforms

Introduction

MRI of the head suffers from rigid body motion that may result in irrecoverable loss of image information. Image artifacts such as ghosting, blurring, and ringing, erroneous quantification of physiological parameters such as diffusion parameters, tissue volumes and BOLD activation can be caused by such motion. Rigid body motion can be described by 6 degrees of freedom and can thus be addressed by updating the imaging sequence in real-time by rotating the imaging gradients and adjusting the RF excitation frequency.

Several methods have previously been proposed to gather the information required to inform the sequence update. Optical motion tracking uses a camera that tracks a marker in a rigid relation to the head (Zaitsev et al. 2006; Andrews-Shigaki et al. 2011; Jessica Schulz et al. 2012; Forman et al. 2011; Aksoy et al. 2011). It has the benefit to operate completely independently of the MR sequence but requires line-of-sight access from the camera to the marker. This is a challenge in many imaging situations where line-of-sight access to the head is obstructed by imaging hardware such as receive coils, goggles and coil-mounted mirrors used in functional MRI (fMRI), or by the body of the patient.

Alternatively, MRI navigators can encode the head position (Ehman and Felmlee 1989; Fu et al. 2005; Welch et al. 2001; van der Kouwe, Benner, and Dale 2006; Tisdall et al. 2012). In this fashion, the line-of-sight requirement can be obviated. However, navigator techniques have two main drawbacks: They rely on additional sequence modules that may considerably prolong scan time and render them incompatible with short-TR sequences that are widely used in clinical practice. Moreover, navigator techniques that rely on MR signal from the head itself alter the magnetization state of the object to be imaged, and thus interfere with the original sequence design, and require computationally expensive algorithms to retrieve the head pose information. The latter two drawbacks can be addressed by using external NMR markers that are rigidly attached to the head (Derbyshire et al. 1998; Krueger et al. 2006; M. B. Ooi et al. 2009). They rely on the signal from a NMR droplet within a small RF coil whose position is conveniently tracked by determining its carrier frequency, which makes it computationally very efficient. Employing transmit/receive coils allows exciting the probes without disturbing the steady-state of the object magnetization. However, these methods still require additional scan time as they rely on additional sequence modules (Dumoulin, Souza, and Darrow 1993) and suffer from carrier frequency instabilities due to magnetic field fluctuations, which occur predominantly at low frequencies and may be caused either by physiological processes (breathing, heart beat) or

by MR system instabilities (B_0 field drifts, gradient field drifts due to temperature changes in the gradient coils, for example).

The drawbacks of unreliable low-frequency field behavior and additional scan time were recently addressed by using gradient tones. Relying on oscillating gradient fields in the kilohertz range, gradient tones are able to track NMR field probes with high robustness against such low-frequency field perturbations. Furthermore, gradient tones can be superimposed onto existing sequence gradients and thus require no additional scan time.

Gradient tones, however, demand additional amplitude and slew rate from the gradient system, which are no longer available for their original assignment and which compromises the gradient waveform design. When inserted into the image-encoding period of an MR sequence, for example, gradient tones cause deviations from the original k-space sampling pattern used for image encoding. This requires additional sequence calibration to ensure well-conditioned image encoding and requires adjustments to the image reconstruction. Another aspect is that the orthogonality constraint between the tones and the sequence waveforms requires pre-filtering the latter if no empty frequency bands are available for the tones, which complicates sequence design. Also, compromises in the available gradient performance for image encoding strategies with long readout trains intensifies the difficulty of correcting image distortions due to static main magnetic field (B_0) inhomogeneity.

Therefore, it would be desirable to track NMR field probes by relying on unmodified sequence gradients while retaining the advantages of the gradient tones approach. This approach requires that the sequence gradient waveforms contain substantial power at frequencies that are not contaminated by physiological field perturbations and that can be reproduced robustly by the gradient system.

Such sequences do exist. EPI and spiral trajectories are examples of imaging readouts that contain significant power at such frequencies. EPI readouts are particularly widely used in applications such diffusion-weighted imaging (DWI) (Ebisu et al. 1996), diffusion-tensor imaging (DTI) and in BOLD fMRI studies of the brain (Bandettini et al. 1992). Rigid body motion constitutes a major obstacle in these applications (Anderson and Gore 1994). The most common imaging readouts used in clinical applications, spin-warp trajectories (Edelstein et al. 1980), are typically built up by trapezoids that contain substantial power at higher frequencies,

too. Exploiting the intrinsic high-frequency content of such sequences is therefore of widespread interest in both the clinical and the research domain.

The goal of this work is to exploit the strengths of the tones approach without its limitations. This is achieved by a generalization of the calibration framework of the tones approach that allows selecting a desired portion of the intrinsic frequency content of a given gradient sequence for sensitive and robust field probe tracking. The proposed approach does not require any modifications to the gradient sequence and hence conserves all of its properties such as total scan duration, image contrast and SNR, B_0 distortions, and the steady-state of the object's magnetization.

Employing NMR field probes for head pose tracking comes with the additional benefit that their signals also capture unreliable field dynamics. While those signal contributions do not offer a solid basis for calibration-based determination of field probe positions, they do act as an image encoding mechanism. Head-mounted NMR field probes readily acquire all relevant field encoding terms acting on the head and thus are a powerful means to inform image reconstruction.

The proposed method is validated in the present work with single-shot 2D EPI readouts. In the first part, its performance is characterized in terms of accuracy and precision. Its ability to perform prospective motion correction in vivo is validated in the second part of this work by studying a case with instructed head motion and a case with a finger-tapping paradigm.

Methods

Model of the field probe signal

The main idea behind the proposed method is to extract information from a desired section of the frequency content of a field probe's phase signal to track its position during the execution of a gradient sequence with substantial power in some desired frequency range. The available spectral information is determined by the waveform of the gradient sequence and may be distributed arbitrarily over several kilohertz. The spatio-temporal field evolution of such a gradient sequence measured by an NMR field probe (De Zanche et al. 2008; Barmet et al. 2010) at position r can be described by spherical harmonic terms of 0th and 1st spatial order as follows:

$$\frac{1}{\gamma}\frac{d\phi(t)}{dt} = b(t) = g_0(t) + \boldsymbol{g}(t)\boldsymbol{r} + b_0(\boldsymbol{r}) + \eta(t), \qquad [35]$$

where ϕ denotes the unwrapped phase of the field probe signal (De Zanche et al. 2008) at

position $\boldsymbol{r}$, γ denotes the gyromagnetic ratio of the field probe's NMR sample, $b(t)$ denotes the

measured magnetic field at the probe's position, b_0 denotes the static component of the

magnetic field at that position, and $\eta(t)$ denotes real-valued additive Gaussian noise. $\boldsymbol{g}(t) = \{g_x(t), g_y(t), g_z(t)\}$ denotes the three components of the sequence gradient waveforms indexed

by time t, and $g_0(t)$ describes the dynamics of the homogeneous field component. Note that

$b_0(\boldsymbol{r})$ is static in time but can be highly structured in space, whereas $g_0(t)$ is constant in space

but highly dynamic in time.

The probe signal is typically sampled at discrete time intervals, yielding the following matrix

representation of Eq. [35]:

$$\boldsymbol{b} = \boldsymbol{g_0} + \boldsymbol{g}\boldsymbol{r} + \boldsymbol{1}b_0(\boldsymbol{r}) + \boldsymbol{\eta}, \qquad [36]$$

where $\boldsymbol{b}$ and $\boldsymbol{g_0}$ denote column vectors of length N_s whose elements (n) reflect field values

acquired at $t = n\Delta t$. $\boldsymbol{g}$ is a matrix whose elements (n, j) denote gradient field values along the

spatial direction $j = \{x, y, z\}$ that were acquired at time $t = n\Delta t$. Δt denotes the sampling interval

and $n = \{0, 1, ..., N_s - 1\}$ is the sample index. $\boldsymbol{1}$ is a column vector filled with ones and $\boldsymbol{\eta}$ is the

column vector of sampled noise instances. $\boldsymbol{\eta}$ denotes sampled noise drawn from a distribution

of zero mean and time-dependent signal variance $\sigma_b(n\Delta t) = 1/(\gamma\Delta t SNR(n\Delta t))$, where

$SNR(n\Delta t)$ denotes the signal-to-noise ratio of the complex-valued probe signal and γ denotes

the gyromagnetic ratio of the probe's nucleus. $\boldsymbol{\Psi}_b$ denotes the covariance matrix of $\boldsymbol{\eta}$ with

diagonal elements $\boldsymbol{\Psi}_b(n, n) = \sigma_b^2(n\Delta t)$.

Note that Eq. [36] and the corresponding description are very similar to the discretized field

model in the previous chapter. The difference is that the matrix $\boldsymbol{g}$ no longer reflects signal from

three sinusoidal tones but rather from sequence gradients with arbitrary spectral content.

Calibration

The proposed method in this work relies on the gradient system's ability to very accurately

reproduce certain parts of its spectral response. In order to exploit that for field probe tracking

the magnitude and phase components of the sequence content at those frequencies need to be

known. They could be computed by applying linear systems theory and exploit knowing the

gradient system's impulse response function (Signe J. Vannesjo et al. 2013). Alternatively, they

can be determined by playing out the sequence itself and measure the gradient system's field

response to it with an array of four field probes at known positions r_{1-4}, yielding the following modification of Eq. [36]

$$(b_1, b_2, b_3, b_4) = g_0 + g(r_1, r_2, r_3, r_4)$$
$$+ 1(b_0(r_1), b_0(r_2), b_0(r_3), b_0(r_4)) + (\eta_1, \eta_2, \eta_3, \eta_4).$$

[37]

Summarizing all unknowns into one matrix $\widetilde{g} = (g, g_0)$, all static field values into the matrix $\widetilde{b_0} = (b_0(r_1), b_0(r_2), b_0(r_3), b_0(r_4))$, and all noise samples into

$\widetilde{\eta} = (\eta_1, \eta_2, \eta_3, \eta_4)$ further simplifies Eq. [37]:

$$(b_1, b_2, b_3, b_4) = \widetilde{g} \begin{pmatrix} r_1 & r_2 & r_3 & r_4 \\ 1 & 1 & 1 & 1 \end{pmatrix} + 1\widetilde{b_0} + \widetilde{\eta}.$$

[38]

Eq. [38] describes the calibration experiment that is done to determine the desired frequency components. The sequence's complex valued frequency component G_{f_m} at frequency f_m can be obtained by evaluating the discrete-time Fourier transform of $\widetilde{g}$ at f_m:

$$G_{f_m} = F\widetilde{g}.$$

[39]

where F denotes a row vector with elements $F_n = 1/\sqrt{N_s} \cdot e^{-i2\pi f_m n \Delta t}$. This procedure can be performed for a desired set of a total amount of N_f frequencies, yielding

$$G = F\widetilde{g}.$$

[40]

Where F denotes a matrix with N_f rows and N_s columns with elements $F_{m,n} = 1/\sqrt{N_s} \cdot e^{-i2\pi mn/N_s}$. G denotes a column vector containing the sequence's complex-valued Fourier coefficients G_{f_m}, and F is the discrete Fourier transform.

Applying the matrix F to Eq. [38] and using the definition in Eq. [40] yields

$$F(b_1, b_2, b_3, b_4) = G \begin{pmatrix} r_1 & r_2 & r_3 & r_4 \\ 1 & 1 & 1 & 1 \end{pmatrix} + F1\widetilde{b_0} + F\widetilde{\eta},$$

[41]

which should be solved for G. This is achieved in two steps. First, the following observation is made: If the frequency f_m is chosen such that it is a harmonic of the acquisition window, i.e. $f_m = m/(\Delta t N_s)$, where $m = \{1, ..., N_s - 1\}$ is a positive, non-zero integer, the dependence on the magnetic field at the probe position vanishes, yielding

$$F(b_1, b_2, b_3, b_4) = G \begin{pmatrix} r_1 & r_2 & r_3 & r_4 \\ 1 & 1 & 1 & 1 \end{pmatrix} + F\widetilde{\eta}.$$

[42]

$F\widetilde{\eta}$ denotes the noise measured at the designated frequencies with covariance matrix $\Psi_{Fb} = F\widetilde{\eta}\widetilde{\eta}^H F^H$, where the superscript H denotes the hermitian transpose operator.

The unknown calibration coefficients G can then be computed by linear algebra:

$$F(b_1, b_2, b_3, b_4) \begin{pmatrix} r_1 & r_2 & r_3 & r_4 \\ 1 & 1 & 1 & 1 \end{pmatrix}^{-1} = G,$$

[43]

The calibration coefficients contain the information about the gradient system's field response at the frequencies f_m that were chosen such that the calibration coefficients are unaffected by low-frequency field perturbations and other non-reproducible effects.

Determination of field probe coordinates

If a field probe measures the same sequence, its coordinates can readily be computed using the calibration information. Applying the discrete Fourier transform matrix F on the field probe signal in Eq. [36] and using the definition $\widetilde{g} = (g, g_0)$ from above yields

$$Fb = F\widetilde{g}\begin{pmatrix} r \\ 1 \end{pmatrix} + F\eta \qquad [44]$$

and inserting the definition from Eq. [40] gives

$$Fb = G\begin{pmatrix} r \\ 1 \end{pmatrix} + F\eta. \qquad [45]$$

The SNR-optimal least-squares estimate of r is obtained by

$$G^+(Fb - g_0) = r \qquad [46]$$

Where $G^+ = \left(g^H F^H \Psi_{Fb}^{-1} Fg\right)^{-1} g^H F^H \Psi_{Fb}^{-1}$ denotes the SNR-optimal Moore-Penrose pseudo-inverse of G.

The noise covariance of the measured positions is given by

$$\Psi_r = \left(g^H F^H \Psi_{Fb}^{-1} gF\right)^{-1}. \qquad [47]$$

Calculating the probe's coordinates in the SNR-optimal way, however, requires knowledge of its time-dependent SNR. This is determined by the probe's signal dephasing during the sequence, which depends on many parameters such as the sequence itself, the probe's excitation flip angle, and, lastly, the probe's position in the FOV. Thus, it is often not possible to estimate its noise covariance matrix Ψ_{Fb} for its SNR-optimal localization. Instead, the best least-square estimator of the coordinates r is chosen such that does not optimize SNR. The corresponding equations for the coordinate r and the noise covariance are then:

$$G^+(Fb - g_0) = r, \qquad [48]$$

where $G^+ = (g^H F^H Fg)^{-1} g^H F^H$ denotes the Moore-Penrose pseudoinverse of G, and

$$\Psi_r = (g^H F^H gF)^{-1}. \qquad [49]$$

Prospective motion correction

Tracking the position of an NMR field probe in each imaging readout allows performing rigid body prospective motion correction (PMC) by adapting the imaging sequence to the current position of the head. Attaching an array of at least 3 field probes in a linearly independent arrangement to a head allows the determination of the head position via the measured probe

coordinates. Since the field probes are also capable of performing dynamic field monitoring (Barmet, Zanche, and Pruessmann 2008), a setup of four such probes was used in order to capture all relevant field dynamic of 0th and 1st spatial order in terms of spherical harmonics. The rigid body motion of the head is described by a set of parameters, a rotation matrix **R** and a translation vector **t,** with respect to a given reference, which are typically the measured probes' coordinates at the beginning of the scan. The field probe signals were acquired during each imaging readout and processed directly on the MR system's spectrometer. Their coordinates were calculated by Eq. [48] and rigid body motion parameters were calculated using the method proposed by Umeyama (Umeyama 1991). The sequence was updated prior to each imaging readout by rotating all sequence gradients, including slice selection gradients, image encoding gradients and crushers, and by adjusting the center frequency of the RF excitation pulse.

Gradient sequence design

To illustrate the method in a commonly used gradient sequence, a single-shot 2D EPI sequence was chosen (**Figure 10**). Its imaging parameters were similar to the ones of a typical fMRI experiment: in-plane resolution = 2.5 mm, slice thickness = 3 mm, acquisition duration = 40 ms, FOV = 21 cm, TE = 25 ms. The long echo time allowed the insertion of a short period without gradient activity between the ^{1}H excitation pulse and the start of the EPI readout. That period was 1.4 ms long and was used to estimate the static B_0 field at the probe positions for later use in the image reconstruction. In order to encode the field probe coordinates in the through-plane direction, a low-amplitude sinusoidal gradient tone (realized amplitude ≈ 1.5 mT/m, frequency = 9.6 kHz) was played out during the entire EPI readout. The determination of the field probe coordinates was based on signal starting immediately after the onset of the EPI readout; signal before that, including the signal used for the determination of B_0 at the field probe position, was discarded.

Hardware setup

In all experiments, ^{19}F NMR field probes (De Zanche et al. 2008; Barmet et al. 2010) were used to avoid RF interference between the imaging experiments and the field probe operation. The field probes were designed to be able to monitor the targeted image resolution and readout duration, resulting in a diameter of the NMR sample of 1 mm and $T_1 ≈ 30$ ms. The field probes were connected to the spectrometer of a 3T Philips Achieva system, which was used throughout all experiments in this work. Custom-built RF hardware was built for independent field probe operation including RF amplifiers and transmit/receive switches. The field probes were excited

immediately prior to the MR image acquisition by an RF excitation pulse from separate hardware. The Larmor frequency of the field probes was 120.2 MHz.
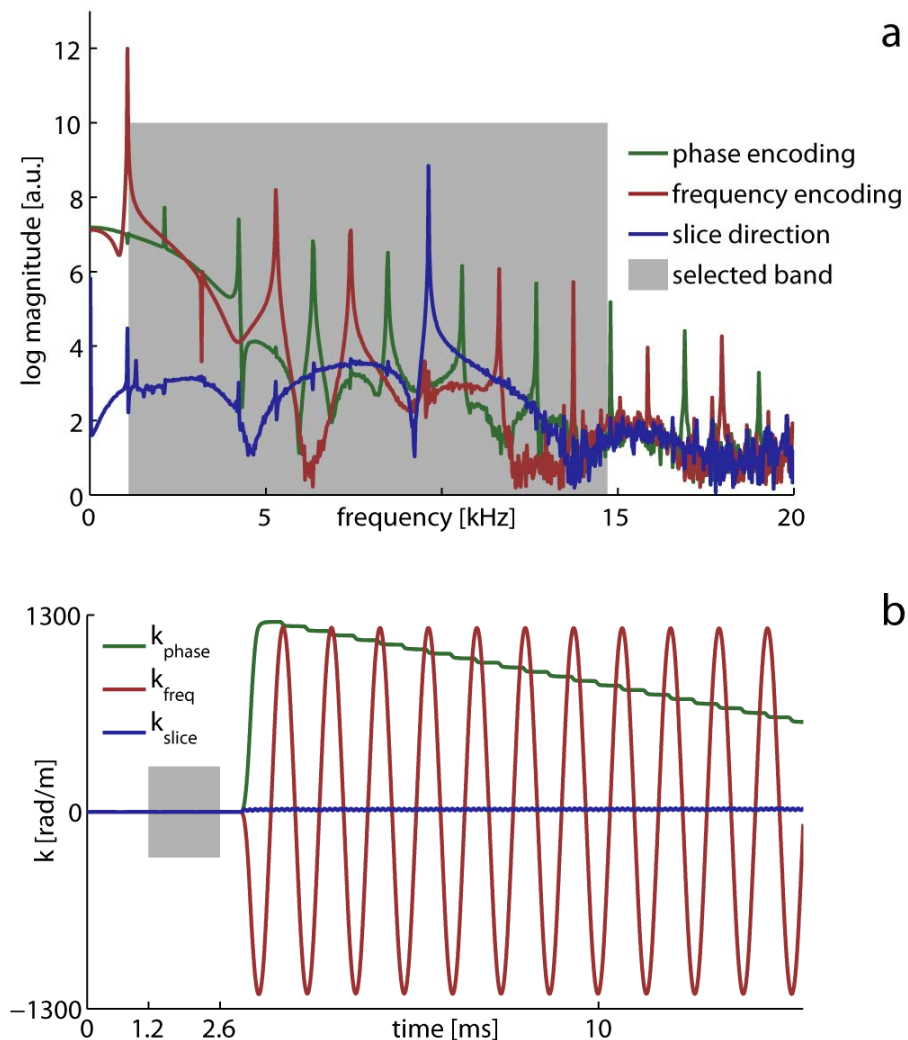
Figure 10: (a) Illustration of the spectral content of the EPI sequence as played out by the gradient system. The gray box indicates the range of frequencies used for the probe localization. Frequencies below 1 kHz and above 15 kHz were left out for robustness and sensitivity, as explained in the manuscript. (b) Time-domain representation of the sequence. The gray box between 1.2 – 2.6 ms indicates the period without gradient activity used to estimate the probes' off-resonance frequencies.

Image reconstruction

Dynamic magnetic field evolutions of 0th and 1st spatial order were computed from the same field probe data as used for slice tracking and a set of reference positions obtained at the beginning of the scan session. The computation of the dynamic fields was done optionally with

static off-resonance frequencies obtained either at the beginning of the scan session or in the period without gradient activity at the beginning of each EPI readout. The off-resonances frequencies were obtained by fitting the probe phase evolution to a linear function, as described in (De Zanche et al. 2008). In the experiments with motion correction, 2D image reconstruction was done based on the concurrently monitored dynamic field data with an iterative conjugate-gradient algorithm using gridding. Note that the concurrently monitored dynamic fields are inherently measured in the subject's frame of reference, which causes some intrinsic in-plane motion correction. In the experiments without sequence update, image reconstruction was done based on a previously monitored k-space trajectory of 0th and 1st spatial order. Phase evolutions in the object caused by the tone orthogonal to the imaging slice were a function of the time-dependent off-center position of each slice and were taken into account throughout.

Experiments

Calibration experiment

In order to calibrate the sequence's Fourier coefficients G, four field probes were rigidly mounted onto an acrylic glass mount within the scanner's FOV. They were placed approximately on the vertices of a tetrahedron, an arrangement expected to yield a very good conditioning of the inversion of the probe coordinate matrix in Eq. [43]. That matrix was filled with known coordinates obtained in a separate experiment by measuring the field probes' frequency shifts under constant gradients of 2.5 mT/m in the x, y, and z direction, respectively (Dumoulin, Souza, and Darrow 1993; Signe J. Vannesjo et al. 2013).

The selected frequencies for the calibration consisted of all harmonics of the acquisition window between 1.1 – 13 kHz. The calibration coefficients were obtained via Eq. [43] by averaging the results from 360 repetitions of the EPI sequence (TR = 700 ms). The obtained calibration parameters were then plugged into Eq. [48] to assess errors in probe localization and rigid body parameters for the static setup. The maximum errors and standard deviations (SD) were computed. Additionally, the standard deviations of the field probe coordinates obtained with the obtained calibration information were computed.

In vivo experiments

In each in vivo experiment, a healthy volunteer was equipped with the custom-built head setup onto which four field probes were rigidly attached (**Figure 11**). The head setup was made up of a headband providing mechanical coupling to the head and a rigid frame providing mechanical

stability to ensure a rigid body relation among the four probes. The frame was made of acrylonitrile butadiene styrene (ABS). The imaging was done with a Philips 8-channel head coil. 15 slices were acquired with a slice TR = 3 s. The motion updates were fed back to the scanner prior to each RF excitation pulse, which amounted to a motion update every 200 ms (= 3 s / 15 slices).

Figure 11: The head setup used for the in vivo experiments. **(left)** The frame with the four field probes. The probes were attached to the frame with tape, which provided good mechanical stability. **(right)** The head setup on a volunteer within the head coil used for the in vivo experiments.

Experiment 1 was performed to validate the slice tracking capability of the proposed method. A healthy volunteer was asked to perform a backward nodding motion (start at t ≈ 30 s, end at t ≈ 60 s) during which 15 slices were repetitively imaged 40 times in a total of 120 s. The experiment was executed twice, once with sequence updates based on the proposed method and once without. In the experiments with sequence updates, image reconstruction for each repetition was performed in three different ways: Once with a reference trajectory obtained in the first repetition of the same experiment, once with the concurrently monitored k-space trajectory using the probes' static off-resonance frequencies from the first repetition of that experiment, and once with the off-resonance frequencies obtained in the period without gradient activity of the repetition that was reconstructed.

In the experiments without sequence update, image reconstruction was performed using concurrently monitored dynamic fields using the probes' static off-resonance frequencies from the current repetition.

To assess the performance of the sequence update, difference images were computed between each repetition and a reference image. The reference image was chosen to be from repetition 5 that was acquired before onset of the nodding motion and after the steady state of the head magnetization had been established. Additionally, the SD over the time series was computed

including repetitions 5 – 40. Repetitions 1 – 4 were excluded as they contained signal changes due to magnetization build-up.

Experiment 2: Two healthy volunteers were imaged using the same sequence while performing a bilateral complex finger-tapping paradigm in a standard block diagram. They tapped their fingers sequentially in the following order: thumb, middle, pinky, index, and ring finger. The instructions were communicated by a programmed video sequence that was projected onto a screen in the scanner suite. The paradigm lasted 30 s, followed by 30 s of rest and was repeated throughout the image acquisition. 208 images were acquired of each of the 15 slices, resulting in acquisition duration of 624 s. The experiment was repeated twice, once with prospective motion correction using the proposed method and once without. Temporal SNR (tSNR) maps were calculated for each slice. In the experiments with sequence update, image reconstruction was performed in the head frame of reference using concurrent field monitoring data. In the experiments without sequence update, image reconstruction was done using concurrently monitored field dynamics, optionally in the head frame of reference and in the laboratory frame of reference. Image reconstruction in the head frame inherently corrects for in-plane motion whereas reconstructing in the laboratory frame contains no motion correction. Rigid body motion parameters of the head and the off-resonance frequencies of the field probes were calculated.

Results

Calibration experiment

Figure 12 illustrates the precision of the probe coordinates measured in standard deviations (SD). The SD of the selected probe along the three different spatial dimensions ranged between 12 – 55 µm (SD in frequency encoding direction = 12 µm, SD in phase encoding = 25 µm, SD in through-plane direction = 55 µm). The resulting errors in the rigid body parameters are illustrated in the center and bottom row of **Figure 12**: The SDs in the rotation parameters were in the order of 10s of millidegrees (frequency encoding direction = 0.008°, phase encoding direction 0.011°, through-plane 0.010°), and the SDs in the translation parameters were in the order of 10s of µm (frequency encoding direction 13 µm, phase encoding direction 19 µm, through-plane 31 µm). The maximum errors were 0.047° (rotation around through-plane axis) and 120 µm (translation along through-plane direction).
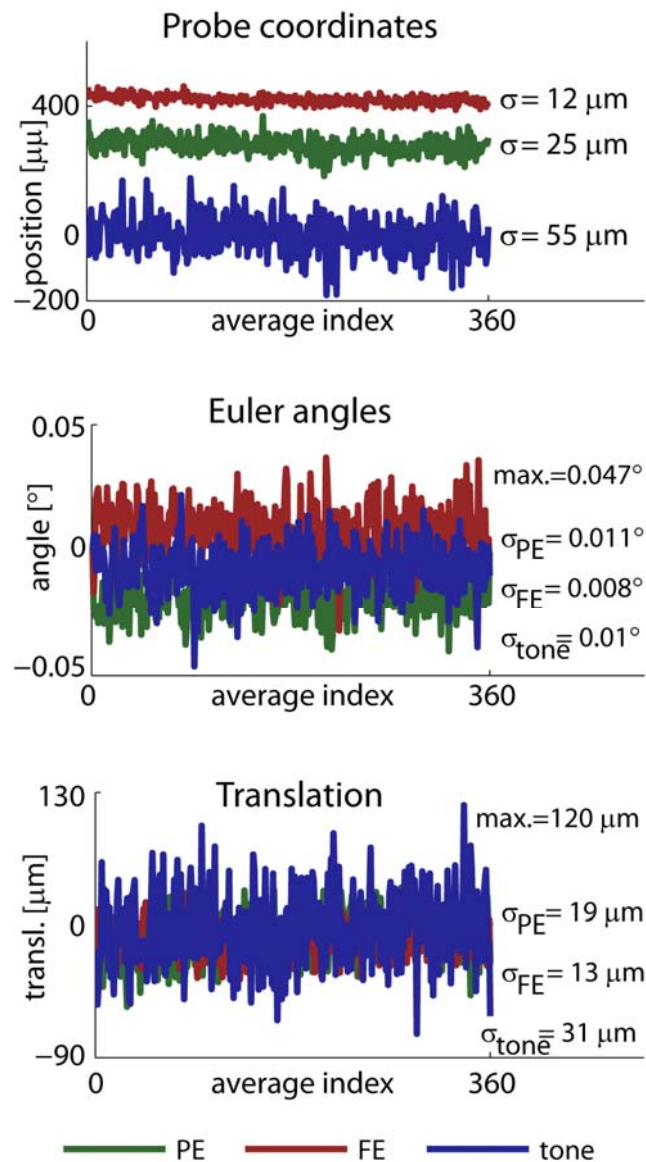
Figure 12: (top) Localization precision of a representative field probe. (center, bottom) Estimations of the rigid body parameters for a static setup.

In vivo experiments

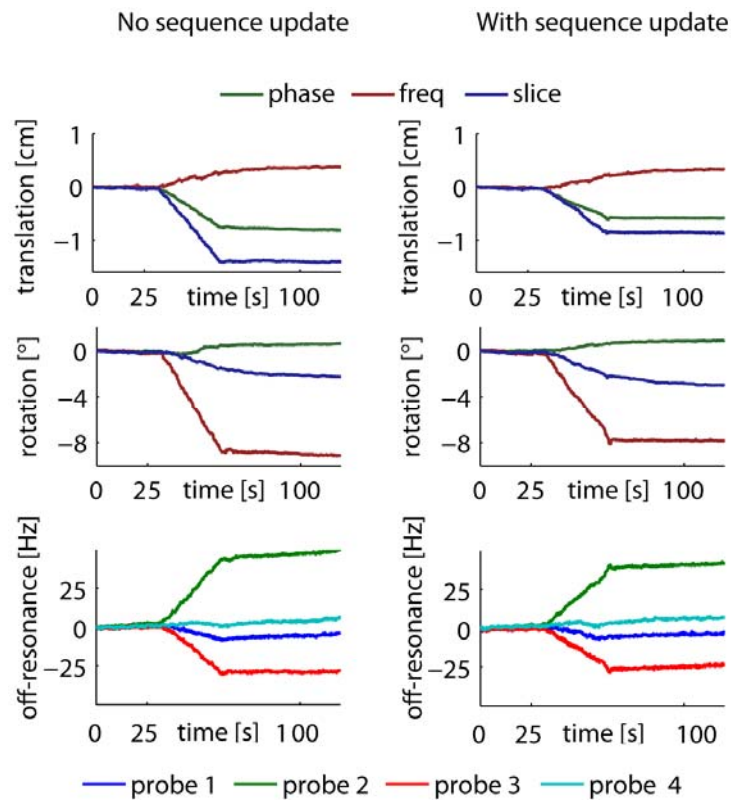*Experiment 1*

Figure 13 illustrate the rigid body parameters for Experiment 1. The left-hand column refers to the experiment without sequence update and shows a head rotation of approximately 8° accompanied by static frequency shifts of the field probes of up to 30 Hz. The right hand column shows the data for the experiment with sequence update with motion and off-resonance values

that corresponded very well to the ones in the left-hand column. The time-dependence of the static off-resonance frequencies correlates with the measured motion and depends on the location of the probe at the head. The probe located right behind the head' top exhibited the strongest deviations whereas the two probes close to the volunteer's ears were less affected. **Figure 14** and **Figure 15** illustrate the image reconstruction results for the experiment without sequence update for a representative slice. Images are ordered left to right and from top to bottom. In **Figure 14** a strong difference between the image acquired in the beginning (top row) and the end if the image acquisition (bottom row). **Figure 15** illustrates the difference images with respect to repetition 5 (right-most image in the top row), clearly showing increasing errors after the onset of motion at t ≈ 30 s (starting in the 3rd row from above). **Figure 15** also shows ghosting in the difference images relating to position-dependent image ghosts.

The results from the experiment with sequence update are shown in **Figure 16** and **Figure 17**. **Figure 16** shows the image reconstruction of the 40 repetitions (ordered from left to right and from top to bottom) of a representative slice showing very good consistency over the acquisition period during with a nodding motion of approximately 8° was performed. Comparing images acquired before and the onset and after the end of the nodding motion, e.g. repetitions 5 (top right) and 40 (bottom right), different distortions are apparent at the top and bottom edges of the brain. **Figure 17** illustrates the differences of each image to repetition 5 (top right), which shows the build-up of the magnetization's steady-state in the top row. The most striking residual errors that come in as motion sets in (after t ≈ 30 s, third row and below) are located at the top and bottom edges of the brain and are caused by position-dependent distortions in the images. The difference images look different if no adjustments to the probes' static off-resonance frequencies are done, as **Figure 18** illustrates. The part at the brain's bottom edge where the error appears larger is stretches over a wider area than in the off-resonance corrected case. It also has a different sign (negative values colored darker, positive values colored lighter), suggesting that the off-resonance correction overcompensated the image distortions to some degree. The error within the brain also seems increased without the correction for the probes' static off-resonance. A comparison of three image reconstructions can be seen in *Figure 19*, which shows data from the experiment with sequence updates. The images on the left-hand side (repetition 5) and the center (repetition 40) of *Figure 19* show the image reconstructions with static probe off-resonance correction, and the image on its right-hand side shows the image of repetition 40 without the correction. A clearly different distortion is apparent between left and right, which is strongly reduced with the correction applied in the center image.

The image differences over the entire time-series can be summarized by its standard deviation (SD), which was strongly reduced by applying sequence updates as **Figure 20** illustrates.

Figure 13: (top, center) Rigid body motion parameters for Experiment 1. In the corrected case, the nodding motion was in good agreement with the uncorrected case, both showing a rotation of approximately 8 degrees. (bottom) Time-dependent probe off-resonance frequencies for each probe. A motion-correlated change is seen, it is stronger for the probes at the volunteer's forehead and neck than at the probes by the volunteers. Probe 1 was located between the volunteer's right ear and temple, probe 2 was roughly behind the head's top, probe 3 at the forehead, and probe 4 between the volunteer's left ear and temple.
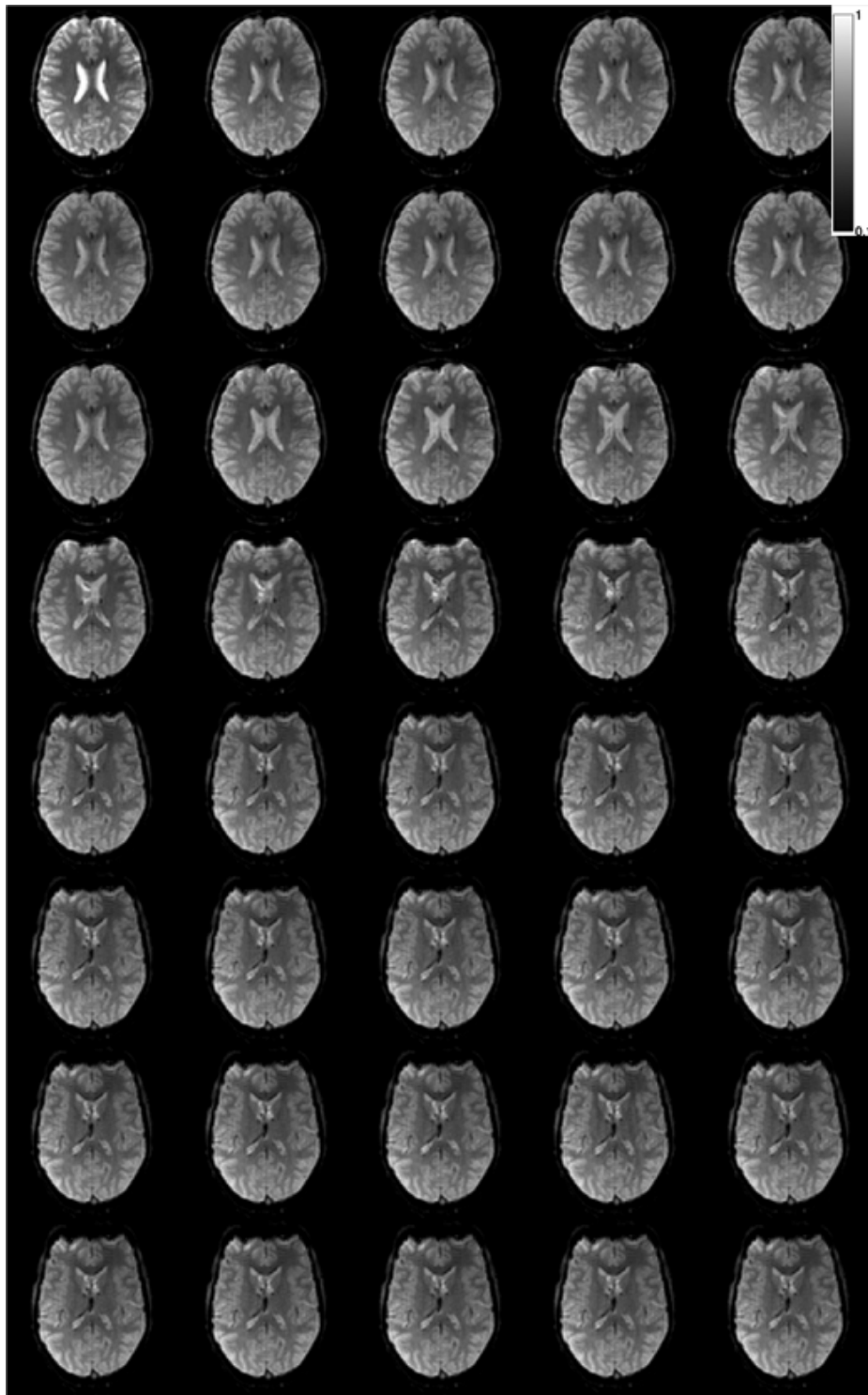
Figure 14: Image reconstructions in for Experiment 1 without sequence update. Time extends from left to right and from top to bottom (repetition 1 is at the top left and the final repetition is at the bottom right). Motion starts in the 3rd row from above and results in the acquisition of inconsistent image information throughout the time series. Steady-state build-up is apparent in the images in the top row.
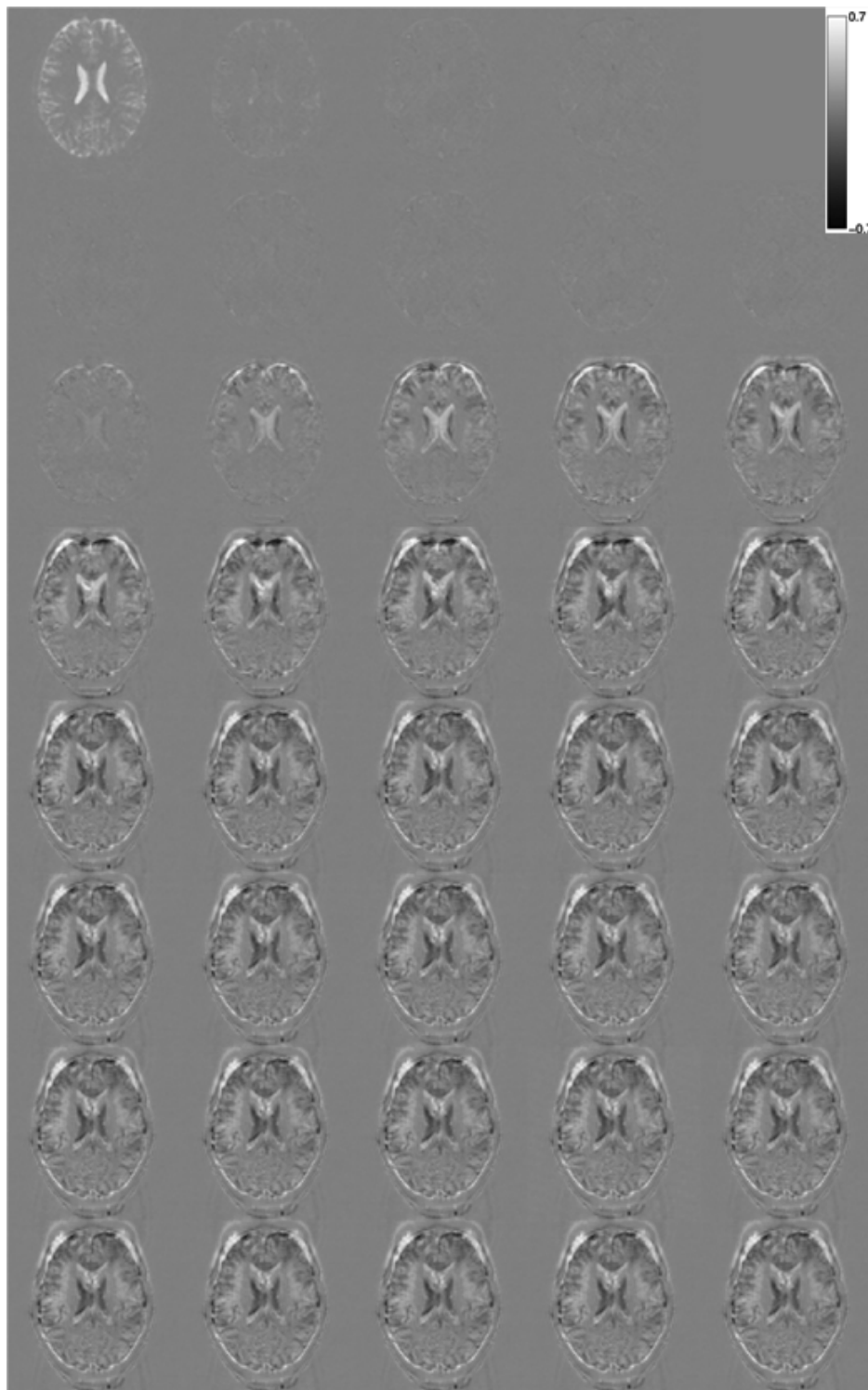
Figure 15: Difference images for Experiment 1 without sequence update. The reference image was acquired in repetition 5. The top row illustrated the establishment of the magnetizations' steady-state, during which no motion occurred. Motion was prescribed to start after the 2nd row (t = 30 s) and is visibly increasing the error starting with row 3. Increased ghosting of the high-frequency image components is also visible with increasing time.
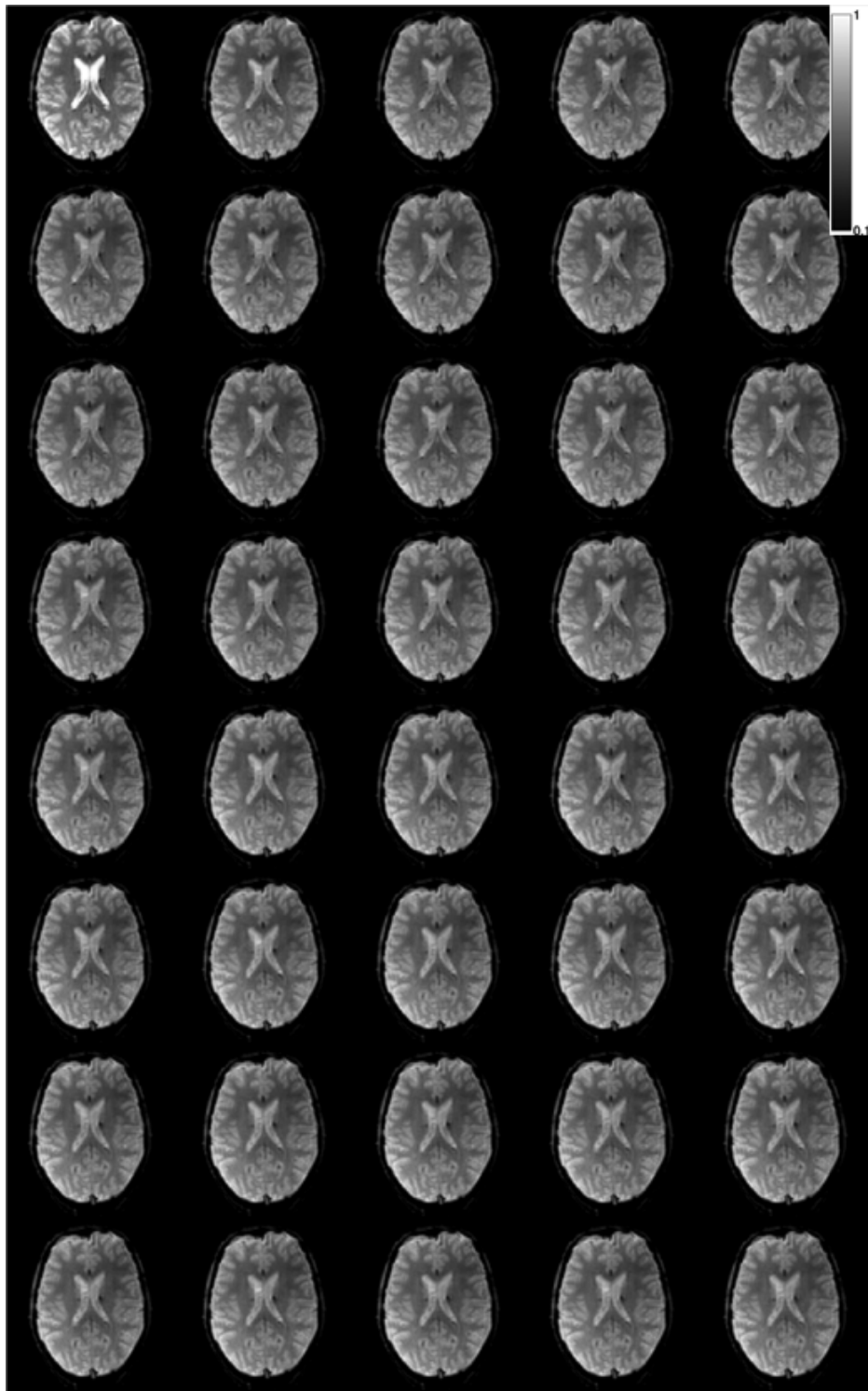
Figure 16: Image reconstruction for a selected slice of the experiment with sequence update. Very good consistency between images is apparent after the establishment of the magnetization steady-state after repetition 5, which is plotted at the top right. The right-hand column of **Figure 13** shows the rigid body motion for this experiment, which was a nodding motion and amounted to roughly 8° and was successfully corrected.
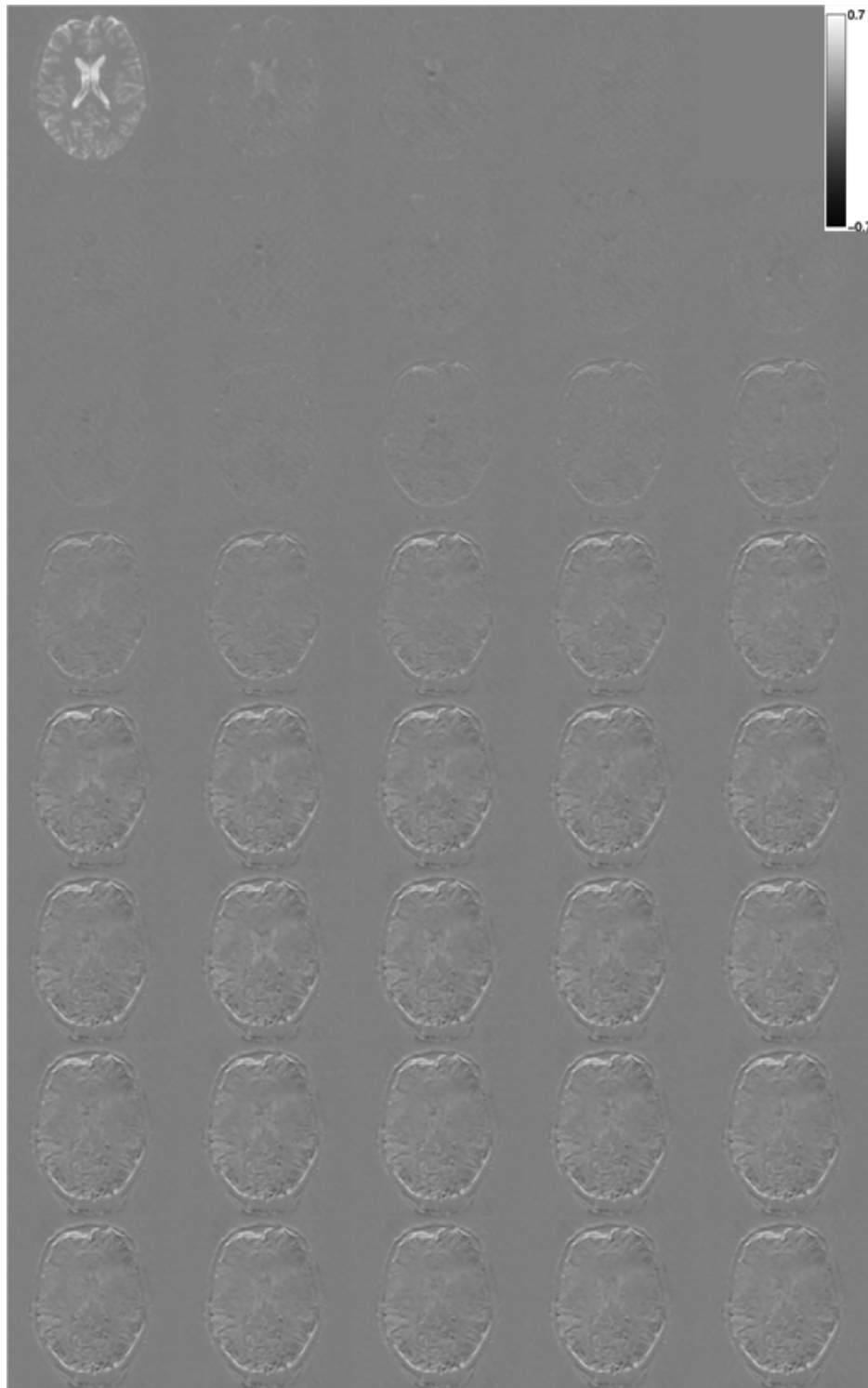
Figure 17: Difference images to repetition 5 (plotted at the top right) of Experiment 1 with sequence updates. The top row was acquired before the onset of motion and shows the establishment of the magnetization stead-state. Small residual errors are visible primarily at the top and bottom end of the brain, which most probably relate to changes in the local background field (B0) due to motion.
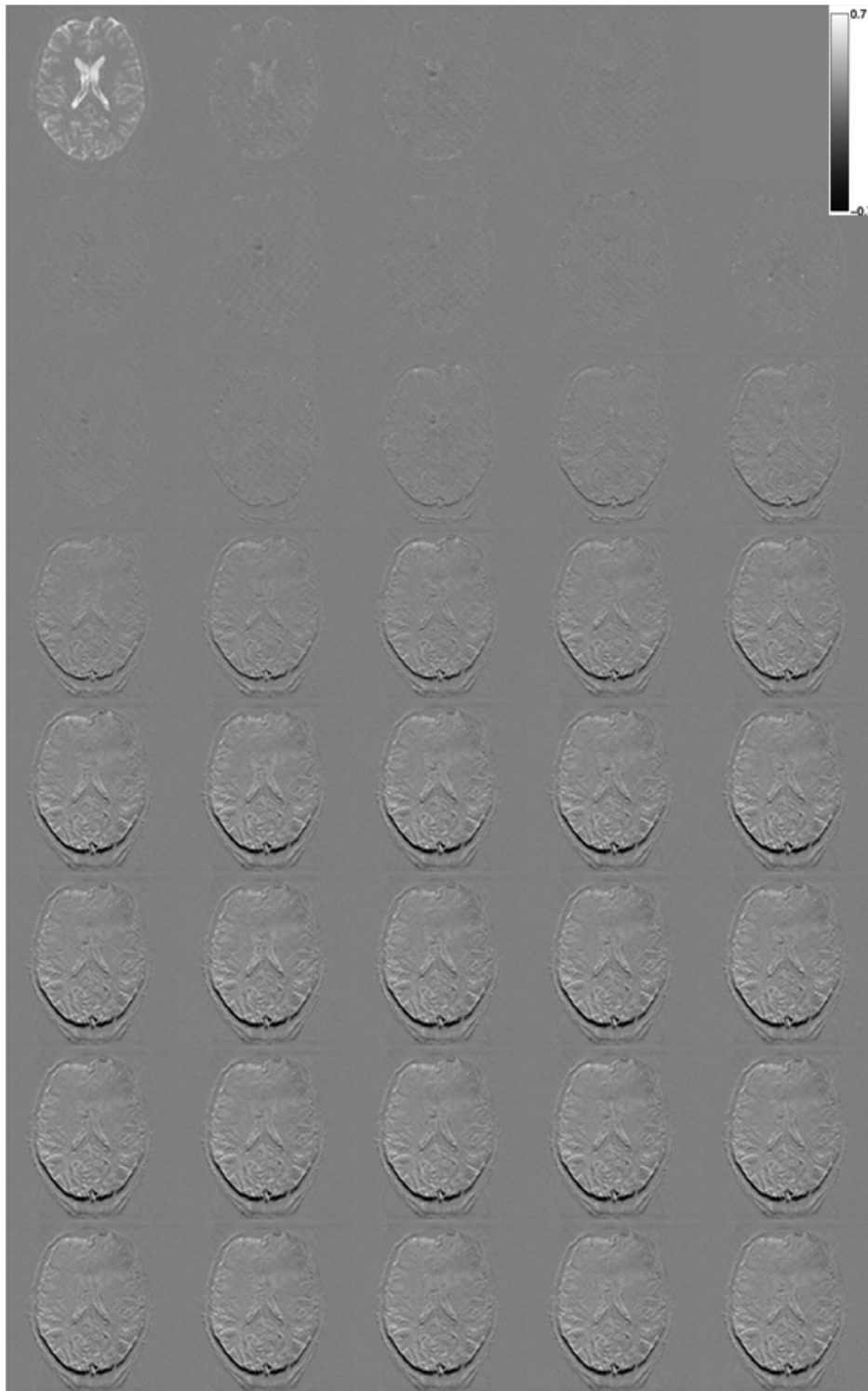
Figure 18: Difference images to repetition 5 (top right) for experiment 1 with sequence update but without adjustments to the time-varying static off-resonance frequency of the probes. Compared to **Figure 17**, the errors at the bottom edge and within the brain are larger but the error at the top edge of the brain is somewhat smaller.
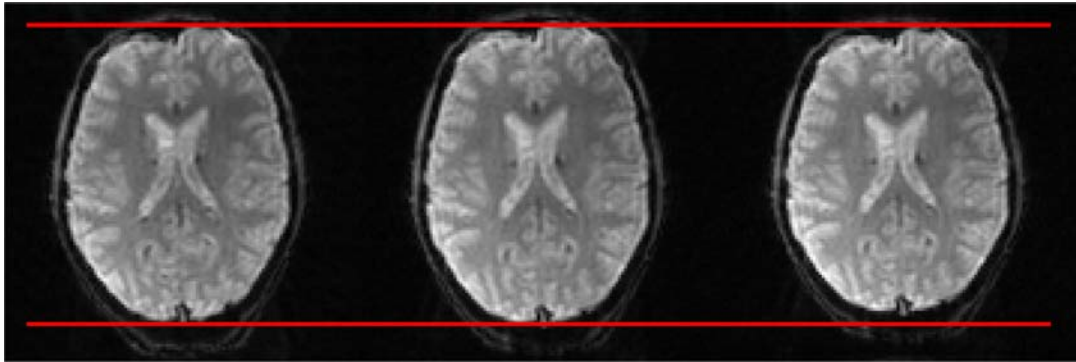
Figure 19: Comparison of image distortions for experiment 1 with sequence updates. The first image (left) shows an image reconstruction at time t = 30 s (repetition 5) based on probe off-resonance frequencies obtained at the same time point. The second image (center) shows the image reconstruction at the end of the scan (time t = 120 s), again based on static off-resonance frequencies obtained at the same time point. The third image (right) was reconstructed with the same data as the second image but with off-resonance frequencies obtained in a separate scan immediately prior to this experiment.
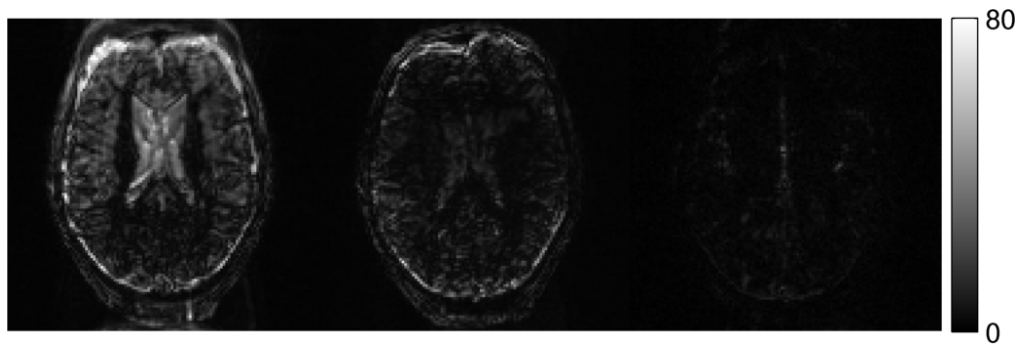
Figure 20: Standard deviation (SD) of the time-series in Experiment 1 without sequence update (left) and with sequence update by the proposed method (center). For comparison, a corresponding slice from a scan without prescribed motion and running PMC is shown on the right. Slice tracking strongly reduces the SD of the time series, as illustrated in the difference between the left and the center images. There is still residual increased SD, particularly at the brain's edges, compared to the case where the volunteer kept still (right).

Experiment 2

Figure 21 illustrates the temporal evolution of the rigid body motion and the field probes' static off-resonance frequencies for both volunteers. The uncorrected scan with volunteer 1 shows motion of up to 2° in rotation and up to 3 mm of translation, which was predominantly in-plane, whereas the uncorrected scan with volunteer 2 contained less motion (max. 0.5° rotation and 1 mm translation). In the experiment with motion correction, volunteer 1 moved somewhat less than in the uncorrected case but a relatively strong (2° rotation, 4 mm translation) and fast (duration ≈ 8 s) jerky motion occurred at t ≈ 350 s. The experiment with motion correction and volunteer 2 exhibited similar motion to the uncorrected experiment with the same volunteer.

Conspicuous, yet small, motion spikes are visible (duration ≈ 2 – 3 s). The off-resonance frequencies are illustrated in the bottom row of **Figure 21**. Their temporal evolution is dominated by a linear frequency drift of about 20 Hz (over the entire scan time of 10 min) that was observed in all probes in all experiments, which corresponds to a drift in the B_0 field of about 370 nT. The divergence of individual off-resonance frequencies is much smaller than in Experiment 1 and amounted to 5 – 15 Hz.
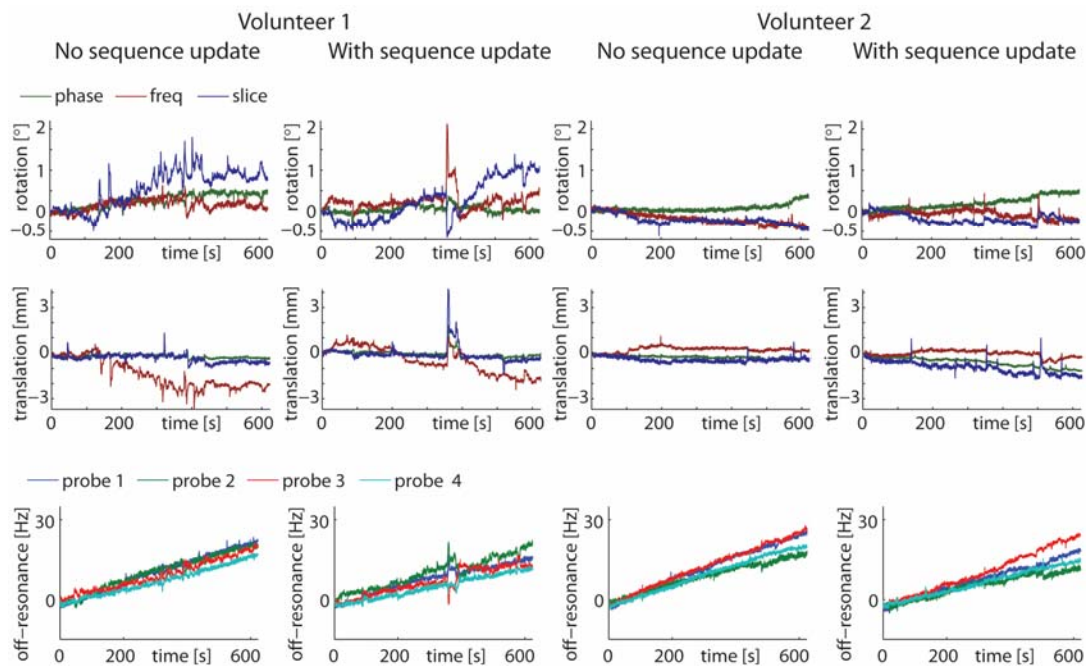
Figure 21: (top, center rows) Rigid body motion parameters for Experiment 2. For volunteer 1, translational motion of more than 3 mm is apparent in both experiments. Volunteer 2 moved little in both experiments; the translational motion in the uncorrected scan was just above 1 mm. (bottom row) The 19F field probes observed a static off-resonance frequency drift of 10–20 Hz over 10 min, corresponding to a field drift of approximately 370 nT. The frequencies diverge less than in Experiment 1 (head nodding).

Figure 22 illustrates the results for the tSNR analysis. tSNR maps of one slice are shown for each volunteer at the top. **Volunteer 1 (left)** Retrospective motion correction by head-mounted field probes ("PMC off pat") performed equally good as prospective motion correction ("PMC on") and both improved tSNR compared to the case without motion correction ("PMC off lab"). The tSNR maps show improvement both at the edges of the brain and within. The smallest effect was observed at the bottom where the tSNR was initially very high. The plot at the bottom left shows the root sum-of-squares of all tSNR values for each slice. The improvement in tSNR by motion correction is consistent over all slices. The tSNR differences get smaller towards slice

1 which contained almost no signal as it was acquired at the edge of the head. **Volunteer 2 (right)** The tSNR is improved in this volunteer but much less than in volunteer 1. Improvements by prospective motion correction ("PMC on") can be seen around the ventricles and the areas that exhibited lower tSNR in the uncorrected case. The plot at the bottom right illustrates the root sum-of-squares of all tSNR values for each slice. In each slice, prospective motion correction outperformed retrospective in-plane motion correction as well as the case without motion correction. The tSNR differences get smaller towards slice 1 which contained almost no signal as it was acquired at the edge of the head.
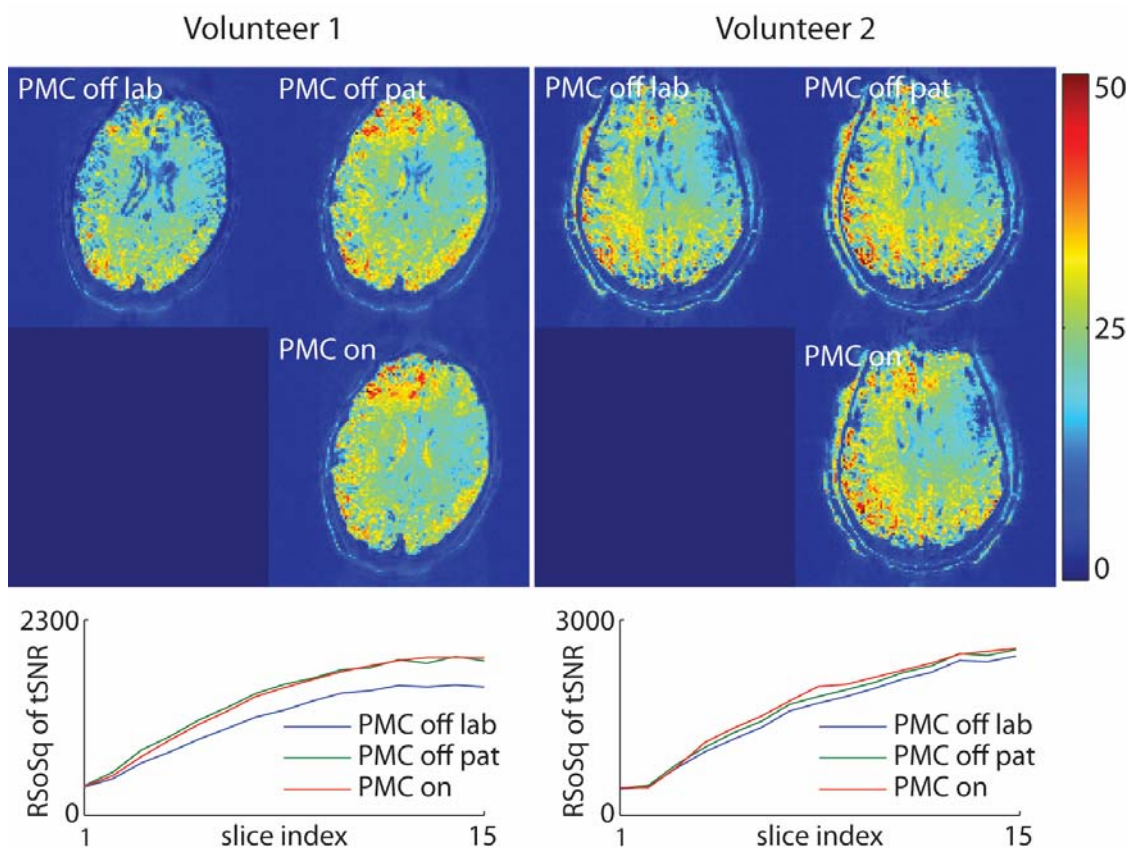
Figure 22: Temporal SNR (tSNR) maps for Experiment 2. (left) Motion correction increases the tSNR for all 15 slices in volunteer 1. Retrospective in-plane motion correction by head-mounted field probes gives identical results as prospective motion correction with the proposed method. (right) In volunteer 2, who moved considerably less than volunteer 1, the effect is smaller. Both motion correction methods performed consistently better than applying no motion correction where in this case, prospective motion correction outperformed in-plane motion correction by head-mounted field probes.

Discussion and Conclusion

This work demonstrates the successful implementation of a novel method to track NMR field probes with precisions ranging between 12 – 55 µm. The method exploits the intrinsic high-frequency content of gradient waveforms allowing robust probe tracking without interference of low-frequency field perturbations from physiological activity or field drifts. Unlike the gradient tones approach, which needs available frequency bands, gradient strength and slew rate, the proposed method is compatible with sequences that offer no room for additional gradient activity. Such sequences are widespread practice where imaging trajectories are often designed to fully exploit either of the gradient system's two primary time-domain constraints, the slew rate or the gradient strength, for efficient image encoding.

In this work, the method was combined with a head-mounted array of 4 NMR field probes to successfully perform prospective motion correction in vivo and synchronously monitor dynamic evolutions for image reconstruction. In this fashion, potential dynamic field imperfections can be accounted for in image reconstruction. The moderate duty cycle of the sequence permitted field monitoring in each readout and full T_1 recovery within one TR. Sequences with higher duty cycle might limit the application of this method in the current implementation. Continuous field monitoring works independently of the sequence's duty cycle and might overcome this limitation (Dietrich et al. 2011). With the current implementation, a solution to the duty cycle limitation would be to use field probes with shorter T_1 relaxation times to enable full T_1 relaxation within one TR. This would prohibit concurrent field monitoring and image reconstruction would have to rely on a reference trajectory from a calibration measurement.

Shortening the probes' T_1 would conserve the ability to track the probes' position, however. This approach would make the current implementation fully compatible with sequences with high duty cycles.

The EPI sequence in the present work was complemented with a small gradient tone in through-plane direction to encode all 3 field probe coordinates synchronously. This approach required the field evolution by that tone to be considered in image reconstruction, which was readily achieved by concurrent field monitoring. It is conceivable to use field evolutions by other gradient waveforms in the through-plane direction. The slice selection gradient, its rephasing or crusher gradient are readily available to be used to encode the probe coordinate in that direction.

As the inherent high-frequency content of the sequence is repeated only once every TR, the sequence update has to rely on position information acquired in the previous TR, which resulted in 200 ms of latency and update rate in this work. This is large compared to optical prospective

motion correction technologies that reported latencies of 19 ms (Jessica Schulz et al. 2012), 60-150 ms (Aksoy et al. 2012), and 39 ms (Maclaren et al. 2012b), respectively or other field probe based methods reporting latencies of 25 ms (Melvyn B. Ooi et al. 2011), and 40 ms (Haeberlin et al. 2014), respectively. As the proposed methods' latency is locked to the sequence TR, motion during the latency period of the motion tracking system results in erroneous slice excitation and incongruent image encoding trajectories in the patient frame of reference. Incongruent k-space trajectories are of minor concern as they result in apparent image rotations if reconstructed in the laboratory frame. This can be accounted for by retrospective image realignment or by directly reconstructing the image in the patient frame of reference as done in the present work. Errors in the slice excitation profile due to motion in the latent period of the sequence update will have to be tackled by estimating the motion at the start of the latency period, i.e. the previous TR, and project the head pose to the current TR. Predictive filters are a common means to address this issue, which will be part of future work.

The calibration of the field probe localization method presented in this work relies on the assumption that the gradient system's field response at high frequencies is invariant to rotations in the input. Work by Vannesjo et al. (Signe J. Vannesjo et al. 2013) shows that coupling among the linear field components and from the linear field components to the homogeneous field component are gradient-coil dependent, thus violating this assumption to a certain degree. The same reference also showed that the amount to which the coupling factors vary lies in the percent range, which should only be of concern in cases of large rotations. The results in this work suggest that the error is very small for rotations up to 8° as the sequence update resulted in very consistent slice excitation. In practice, motion is much smaller as was apparent in the finger-tapping experiments, which means that the assumptions made for the field probe tracking method are not a limiting factor in terms of accuracy.

Another assumption of the calibration model presented in this work is its reliance on dynamic fields of only 0th and 1st spatial order in terms of spherical harmonics. Concomitant fields or eddy currents caused by the diffusion gradients in DWI sequences violate that assumption. The same considerations as in the gradient tones approach apply here: The proposed calibration model is readily extendible to incorporate higher order fields but demands a non-linear algorithm to obtain the probes positions, which requires further investigation.

In cases with stationary objects, concurrent field monitoring of higher order dynamic fields is a viable means to account for gradient nonlinearity-induced image distortions in DWI (Wilm et al. 2011). In the case of bulk motion, distortion correction for constant gradient shapes was

developed recently (Yarach et al. 2014). However, distortions in sequences not limited to constant DC fields such as EPI readouts depend on the frequency content of the sequence and on the head position at each time point during the data acquisition. Head-mounted concurrent field monitoring using more than four field probes could address that problem but requires significant effort in hardware development as a sufficient number of field probes is required on the head to capture the relevant field dynamics.

The precisions in the rigid body parameters obtained with the EPI sequence used in this work were high compared to the image resolution (13 µm, 19 µm, 31 µm; 2.5x2.5x3 mm^3), amounting to RMS errors of about 1% of the pixel width in through-plane direction, and less in the in-plane direction. This was good enough for the studied example that exhibited a somewhat coarse image resolution. In order to boost the precision of the proposed method for high-resolution EPI sequences, for example, the selected frequency range could include the EPI's main peak and much lower frequencies as long as they allow robust probe tracking. Note that the frequency range is expected to be contaminated by low-frequency field perturbation is probably much narrower than 1 kHz and thus robust probe tracking with increased precision could be achieved by including frequencies of about 100 Hz.

The results in the experiments with instructed, large, motion show that image reconstruction based on concurrently monitored dynamic fields benefits in terms of image congruency if the individual static off-resonance frequencies of the field probes are tracked and taken into account in the computation of the k-space trajectory. It has been shown that by virtue of the long TE of the EPI readout, a brief period ($\approx$ 1.4 ms) without gradient activity could be exploited to acquire static off-resonance frequencies with sufficiently high precision to obtain improved image congruency.
The results in the experiments with involuntary motion, which illustrates a much more realistic scenario, show that the static off-resonances do not diverge among probes but are rather dominated by a drift of the background field. This suggests that the off-resonance correction required for the instructed motion will not be required in typical imaging scenarios, allowing for concurrent field monitoring based image reconstruction without modification.

The proposed method may be very useful in fMRI applications with task paradigms that suffer from rigid bulk motion. It may also enable the study of BOLD activation for motor paradigms that were very challenging or impossible to conduct due to strong bulk motion, for example leg

movements, extended arm movements, and movement of the head itself. With the increasing interest in fMRI studies at 7T, the capability to concurrently monitor dynamic encoding fields will be essential to correct for field perturbations in the head induced by the moving anatomy, as has been shown recently (Signe Johanna Vannesjo, Barmet, et al. 2012). FMRI experiments often use goggles and mirrors, which occlude the line-of-sight to the head and thus limit the applicability of current optical motion correction methods. RF based methods like the one presented here may be more practical in such imaging scenarios.

The application to EPI-based DWI is readily possible, yet limited to correcting bulk motion during the image acquisition. However, DWI suffers from bulk motion during the application of the diffusion gradients, which may cause irrecoverable signal voids and warrants continuously updating the diffusion gradients (Herbst et al. 2012).

Advances in prospective motion correction for clinical routine head MRI using gradient tones

Introduction

Rigid body motion is a major contributor to image quality degradation in both clinical and research applications of MRI. Prospective motion correction (PMC) methods address that problem by adapting the geometry of the MR sequence to the head pose to reduce the irrecoverable information loss incurred by such motion during the MR experiment. Several different marker-based approaches have recently been proposed to implement PMC. Methods based on optical cameras, on one hand, have the advantage to operate fully independently of the MR sequence (Zaitsev et al. 2006; Andrews-Shigaki et al. 2011; Maclaren et al. 2012b; Aksoy et al. 2011; Forman et al. 2011; Jessica Schulz et al. 2012), and RF coil based methods, on the other hand, benefit from their lack of a line-of-sight requirement to the head (Derbyshire et al. 1998; Krueger et al. 2006; M. B. Ooi et al. 2009; Haeberlin et al. 2014).

To encode the marker coordinates, RF coil based methods rely on gradient activity that entail either dedicated sequence modules at zero frequency (Dumoulin, Souza, and Darrow 1993) or high-frequency gradient oscillations (Haeberlin et al. 2014). The gradient tones approach is of particular interest as it allows field probe tracking without any extra scan time, rendering it compatible with short-TR sequences used in clinical practice. Field probe tracking without extra scan time is achieved by inserting the gradient tones into frequency bands orthogonal to the ones occupied by existing sequence gradient waveforms, which allows performing the sequence task in synchrony with field probe tracking. Additionally, the gradient tones approach exhibits high robustness against common low-frequency field fluctuations from scanner instability (main field drifts) or physiological activity (breathing, heart beat), which compromise the accuracy of field probe tracking methods using constant gradients.

The implementation of the gradient tones concept presented in (Haeberlin et al. 2014), however, contains design choices that may limit the method's acceptance in clinical practice. Firstly, the gradient tones are inserted into the sequence's image encoding gradients and extend over the entire duration of the gradient trapezoids. As a result, sequence gradients have to be stop-band filtered in a pre-processing step to ensure orthogonality to the gradient tones. Additionally, image reconstruction needs to be informed about the exact realization of the gradient tones and the filtered sequence gradients. This requires either modifications to existing product software on a clinical scanner or exporting the imaging data and employing custom-made reconstruction software on an external computer.

Furthermore, when PMC is applied the gradient tones need to be subject to the sequence update and be rotated in the same manner as the image encoding in order to avoid sampling gaps in k-space for well-conditioned image encoding. This affects the steady-state of the eddy currents at the tones frequencies, violating the calibration model to a certain degree, which may result in errors in the field probe coordinates.

Secondly, their implementation combines field probe tracking with concurrent field monitoring of the image encoding part of the pulse sequence. In that fashion, the method is able to include unexpected field dynamics for image reconstruction. Concurrent field monitoring of image encoding gradients, however, couples important imaging parameters to the choice of probe diameter. The maximum extent in k-space cannot exceed the reciprocal of the probe diameter by roughly twofold (Barmet, Zanche, and Pruessmann 2008), and the sequence TR must be such that in enables extensive (or full) T_1 recovery of the probe signal for sensitive field monitoring in each readout.

Thirdly, they use the scanner's own spectrometer as receiver for the field probe signal, which requires available RF receiver hardware for ^{19}F signals on the MR system. Also, they use the scanner's real-time sequence control program to perform the signal processing that returns the sequence geometry updates. This reduces the resources available for computing other parts of the sequence, which could render the sequence execution instable and ultimately limits the minimum sequence TR.

In the present work, an alternative implementation of the tones approach for prospective motion correction is proposed in order to facilitate its use in clinical applications. It conserves the core idea of gradient tones as encoding mechanism for field probe coordinates while avoiding numerous limitations of the previous design.

The proposed modifications are based on the observation that the vast majority of clinical pulse sequences are based on a combination of robust spin-warp imaging readouts (Edelstein et al. 1980) and a set of either crushing and balancing gradients that are implemented with trapezoidal gradient waveforms.

A first design modification concerns the application of concurrent field monitoring of each image-encoding segment of the sequence. To date, image quality in clinical MR imaging is not limited by image encoding errors concurrent field monitoring is able to account for. Also, the results shown in (Haeberlin et al. 2014) exhibited no visual degradation in image quality when a reference trajectory was used for the image reconstruction of a spin-warp sequence. By

sacrificing the concurrent field monitoring capability in the present work, the probe design can be fully optimized for its motion correction assignment. For instance, the probe's T_1 can be optimized for the expected motion bandwidth and the required duration of the gradient tones for a targeted localization precision.

A second design modification concerns the placement of the gradient tones within the pulse sequence. Most practical pulse sequences contain additional sequence parts that either include gradient waveforms to either crush or balance the object's magnetization or are free of gradient activity to allow T_1 relaxation for contrast or SNR optimization.

In the present work, the tones are inserted into those sequence parts. This allows conserving the sequence's image encoding gradients, which avoids informing the image reconstruction about the existence of the tones. As a consequence, the scanner's native image reconstruction routines can be used, which is of great practical utility. In this fashion, the design of the probe geometry, e.g. the diameter of the NMR droplet, is simplified as it becomes fully decoupled from the targeted image resolution. In particular, the probe diameter can now be substantially larger than previously, which allows for higher SNR and shorter tones segments.

Removing the gradient tones from the image encoding parts of the pulse sequence also does away with the requirement to subject them to the sequence update by the prospective motion correction. Instead, each gradient tone remains fixed on one gradient axis. In this fashion, the steady-state of the eddy currents at the tones frequencies is not disturbed, rendering the probe localization more robust.

A third design choice in the present work avoids pre-filtering the sequence gradients to render them orthogonal to the tones. This is achieved by exploiting the trapezoid's plateau that consists of a period of constant gradient amplitude. This sequence part is inherently orthogonal to the gradient tones.

Another modification to the previous implementation concerns the hardware and software used for signal reception and processing. In the present work, an independent external spectrometer receives the ^{19}F field probe signals, which avoids the need for the scanner to provide dedicated RF receive channels capable of doing that. Moreover, dedicated software running on the external spectrometer computes the sequence geometry updates without interfering with the scanner's real-time sequence control program.

The proposed PMC system is validated with a spoiled multislice and a 3D T_1w gradient echo (FFE) sequences. First, the performance of field probe localization with gradient tones on the sequence's spoiler gradients is assessed in terms of precision. Then, it is applied to in vivo brain imaging.

Methods

Field probe design

The field probe design was identical to the one in the original gradient tones implementation. The key elements are repeated here for completeness.

All experiments were done using NMR field probes as described in (De Zanche et al. 2008; Barmet et al. 2010). To avoid RF interference between the monitoring and the imaging experiment, perfluoropinacol-based ^{19}F NMR field probes were used with a droplet diameter of 1 mm, a Larmor frequency of 120.2 MHz, and $T_2^* \approx 4$ ms. The field probes were excited with a hard excitation pulse (duration 5 µs, nutation frequency 50 kHz, power ≈ 5 W) triggered by separate hardware.

External receiver and motion correction system

RF signal reception

The field probe signals were routed by custom-built hardware including PIN diode switches for independent transmit/receive operation, and a preamplification stage (Barmet et al. 2010). The blanking signal of the MR scanner's RF amplifier was routed to logic gates controlling the T/R switches to ensure save receive operation. Signal reception was triggered by the MR system and performed by custom-configured high-speed spectrometers based on field-programmable gate arrays (National Instruments, Austin, TX, USA).

Digital probe signal processing

Data processing was performed by dedicated software elements developed in LabVIEW running on a Windows 7 operating system (Microsoft, Redmond, WA, USA). In a first stage after signal reception, the LabVIEW program "Scan Application" performs all signal processing steps to return the unwrapped probe phase coefficients. The Scan Application was developed in-house for various field-monitoring projects within this research group (Wilm et al. 2014; Dietrich et al. 2011; Duerst et al. 2014). A new data interface was implemented and included after the phase unwrapping step in order to make the probe phase data available for further motion-correction

related signal processing. The interface is a FIFO stack (first-in/first-out) dubbed "queue" in LabVIEW terms, and "Ext. Phase Queue" in the particular implementation. See **Figure 23**a-d for a flow chart of these subsystems.
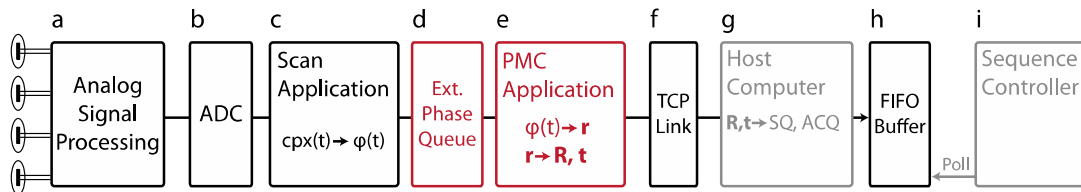
Figure 23: The prospective motion correction system. Black boxes label pre-existing technology, either from in-house developments (a-c), or the scanner manufacturer (f,h). Gray boxes denote pre-existing technology that was reconfigured for the motion correction task (g,i), and red boxes denote subsystems developed in the present work. (d,e) The PMC Application receives the phase data via a dedicated queue that was added to the Scan Application (c) and computes the rigid body parameters (RBP, rotation matrix R, and translation vector t, respectively). It transmits the RBP to the scanner's host computer (g) via a TCP link (f). The reception of the TCP message triggers an event on the host resulting in the assignment of the corresponding sequence (SQ) and acquisition (ACQ) parameters, which are then exported to a FIFO buffer (h) shared by both the host and the real-time sequence control program (i). The latter empties the buffer by polling for geometry updates every TR.

The second stage of the signal processing steps consisted of the routine that computed the field probes coordinates based on the unwrapped phase values provided by the queue (**Figure 23**e). It implemented Eq. [25], which allows the field probe computation in the presence of gradient tones. The calibration matrix enters the operation as a constant parameter and was stored in local RAM. Flexible use of different tones calibration matrices was enabled by keeping the calibration information in local text files and writing them into the LabVIEW RAM via its "file read" interface prior to its first use. In that fashion, it is straightforward to use a variety of different tones during the same scan session. This is beneficial if the different imaging sequences demand, or allow, different optimization trade-offs in terms of tones amplitude, duration, or frequency.

The implementation of Eq. [31] that obtained the rigid body parameters was part of the same signal processing stage and followed directly after the probes' coordinates had been obtained. The rigid body parameters were computed by comparing the current probes coordinates to a set of reference coordinates. In order to label a set of probe coordinates as either "reference" or "current" coordinates, a binary switch as implemented that could be set to "reference" at any desired moment and that toggled back to "current" immediately after the probe coordinates had been stored. In the present work, the switch was reset to "reference" prior to the first interleave of a new scan. However, its use is more flexible. For instance, the reference scan could be set

only at the beginning of an entire scan session, allowing for consistent volume coverage. It has to be kept in mind, however, that this requires the insertion of a "reference coordinate acquisition" that precedes image acquisition and does not excite the imaging volume to avoid excitation inconsistencies with subsequent readouts.

Scanner software interfacing

The rigid body parameters were transmitted via an Ethernet link (using the TCP protocol) to the MR scanner's host computer (**Figure 23** f,g). The scanner manufacturer provided software source code, precompiled binaries, and many valuable instructions to convert the array of rigid body parameters to a suitable TCP message recognized by the host computer. The transmission protocol is based on the manufacturer's external data handling interface XTC (Smink et al. 2011). The host computer was reconfigured to listen to TCP messages (on a defined communication port) from a given computer address (given by the external computer's name). The reception of such a message triggered the execution of a pre-existing callback function that was customized for proper data handling. The processing steps in that function, *ipmc_new_motion_cb(MOTION_STRUCT *motion_ptr)*, included minor local modifications for proper assignment of sequence orientation matrices and RF center frequency offsets. *motion_ptr* denotes a pointer to the struct containing the rigid body transformation. The final signal-processing step in that routine involved writing the new geometry information into a FIFO stack (**Figure 23**h) that was shared by both the host computer and the real-time sequence controller (**Figure 23**i).

The implementation on the sequence controller required a few more minor software changes. In contrast to the host computer, whose reaction to incoming motion information is event-triggered, the sequence control program needs to be programmed to poll the shared FIFO stack for incoming geometry updates. The polling is implemented by a call to the function *MCUI`:poll_for_updates(MPF_UPDATE_FUNC update_procedure_cb)*, which was modified such that it was performed every TR. The manufacturer's pre-existing implementation had polled for geometry updates after the acquisition of an entire image, a reflection of its initial use in high-intensity focused ultrasound (HIFU) applications (de Senneville, Mougenot, and Moonen 2007; Ries et al. 2010). In order to ensure that the latest available geometry update was used for the sequence update, it was called within a while loop until the FIFO stack was empty.

Another aspect that had to be considered within the real-time environment of the sequence controller was inherent latency due to precompiled sequence instructions. The sequence control code precompiles sequence instructions ahead of its execution ("ahead time"), which amounts

to typically a few TR. Precompiling code stabilizes the sequence execution but increases latency as newly arrived geometry information is not integrated into already compiled code. This "ahead time" can be adjusted by instructing the sequence control program to wait for its hardware to catch up. This is achieved by calling *SQ`wait_for_hw(maximal_ahead_time)* immediately after the arrival of new geometry information. In the present work, it was found heuristically that ahead times of 10 ms or more yielded robust sequence execution for the sequences studied.

Experiments

All experiments were performed using the same head setup as in the first tones implementation. The calibration measurements were performed by rigidly mounting the head setup onto a disc-shaped, structured water phantom. In the in vivo experiments, a healthy volunteer was equipped with the head setup. All experiments were performed with a Philips 8-channel head coil. Image reconstruction was performed using the standard image reconstruction pipeline provided by the MR system manufacturer.

Sequence 1: Multislice T_1w FFE

In these experiments, three gradient tones were inserted into the crusher gradients of a multislice T_1w FFE sequence (**Figure 24**a). The strength of the crusher gradients as prescribed by the sequence was such that that it allowed the insertion of additional tones without any modifications. The tones parameters were as follows: nominal amplitudes $A_x = A_y = A_z = 6$ mT/m, f_x =2.1 kHz, f_y = 3.6 kHz, f_z = 5.0 kHz, duration = 1.4 ms. The tones were centered on the 3 crusher gradients' plateaus (duration = 1.55 ms).

The sequence parameters were: FOV 24x24x12.9 cm^3, slice thickness 5 mm^3, slice TR = 251 ms, TE = 4.6 ms, flip angle 80º, 20 slices, reconstruction matrix 560x560, and total scan duration = 85 s. Motion update interval = 12.55 ms (= slice TR / slices).

A calibration experiment was performed with the head setup on the disc-shaped phantom and playing out the sequence with identical timing parameters. The crusher gradients were turned off to increase probe's SNR. The probe coordinates were computed only every 4th TR, which corresponds to a frequency of 19.9 Hz and an update interval of 50.2 ms. The localization precision was determined by computing the root-mean-square error (RMSE).

An experiment was performed to assess the delay of the PMC system. For that purpose, the sequence was played out with a few modifications. For easier data analysis, the field probes were triggered every TR, which corresponds to a rate of 79.7 Hz. Also, the crusher gradients on which the tones had been placed were removed from the sequence for better probe SNR. The gradient tones were configured to rotate along with a prescribed sequence rotation, unlike in the other experiments. The probe signal processing was kept the same as for the other experiments except that a binary rotation pattern was sent to the scanner. In this fashion, the measured probe positions reflect a delayed picture of the known binary rotation pattern that was sent to the scanner, which was used to determine the latency of the feedback loop.

In vivo experiments were performed using the same timing for the field probe operation as in the calibration experiment, resulting in a motion update rate of 19.9 Hz. A healthy volunteer was instructed to perform a nodding motion in a first experiment and a "head shake" motion in a second experiment, and to remain still in a third experiment. All three experiments were performed twice, once with sequence updates and once without.

Sequence 2: 3D T1w FFE

This sequence offers an interval without gradient activity after the crusher gradients, in which the tones were inserted (**Figure 24**b). The tones parameters were as follows: nominal amplitudes $A_x = A_y = A_z = 6.5$ mT/m, $f_x = 1.5$ kHz, $f_y = 3.0$ kHz, $f_z = 4.5$ kHz, duration = 2.0 ms. The suggested REST slab was inserted at the neck.

The sequence parameters were: FOV 24x24x13.0 cm^3, slice thickness 1 mm, slice TR = 25 ms, TE = 1.9 ms, flip angle 30 degrees, 130 slices, reconstruction matrix 256x256. Motion update interval = 25 ms.

A calibration experiment was performed with the head setup on the disc-shaped phantom and playing out the sequence with identical timing parameters. The probe coordinates were computed every single TR, which corresponds to a frequency of 40 Hz and an update interval of 25 ms. The localization precision was determined by computing the root-mean-square error (RMSE).
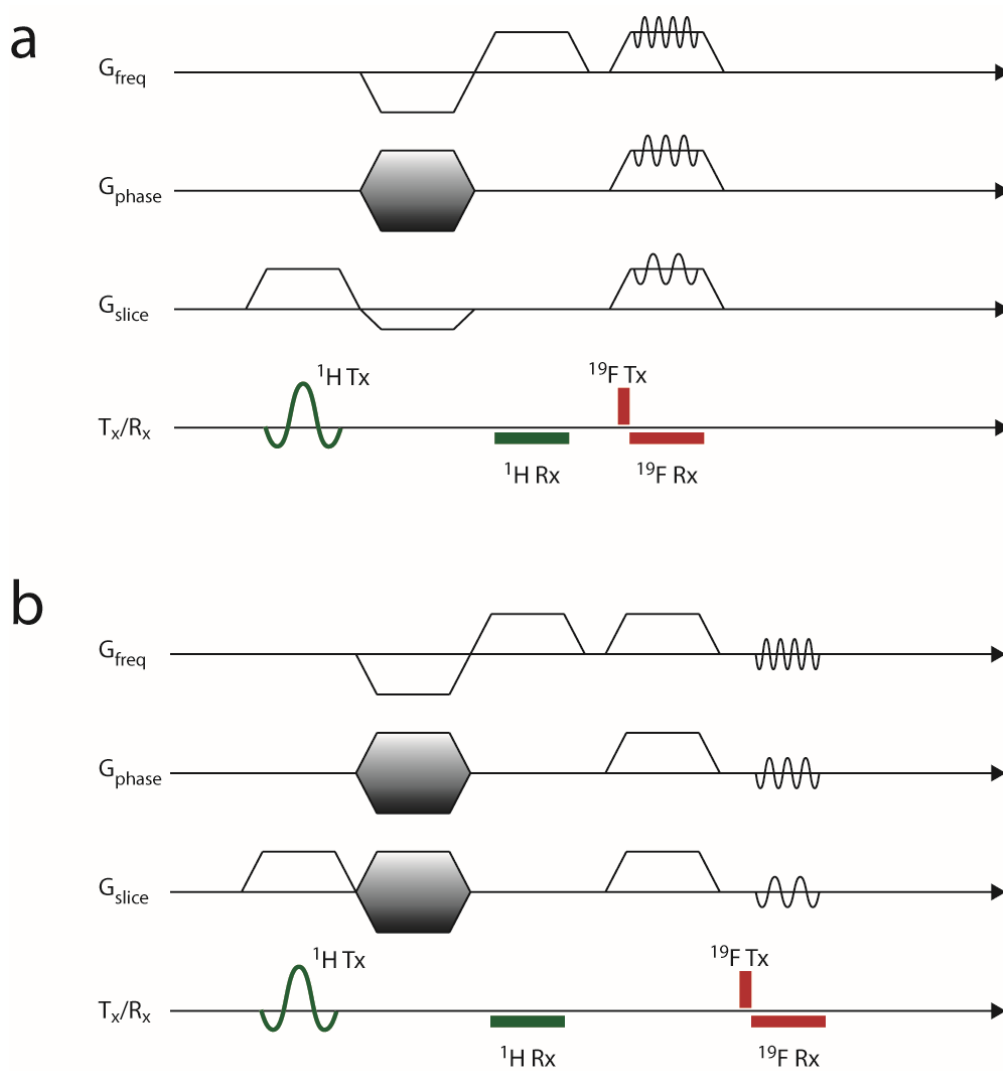
Figure 24: Pulse sequence diagram of the 2D Multislice T1w FFE (a) and the 3D T1w FFE (b) sequences. In (a), the gradient tones are placed on the crusher gradients as no idle time is available between the crushers and the subsequent slice excitation. In (b), a window without gradient activity after the crushing gradients was exploited for tone placement. The field probes are excited immediately before the tones readout.

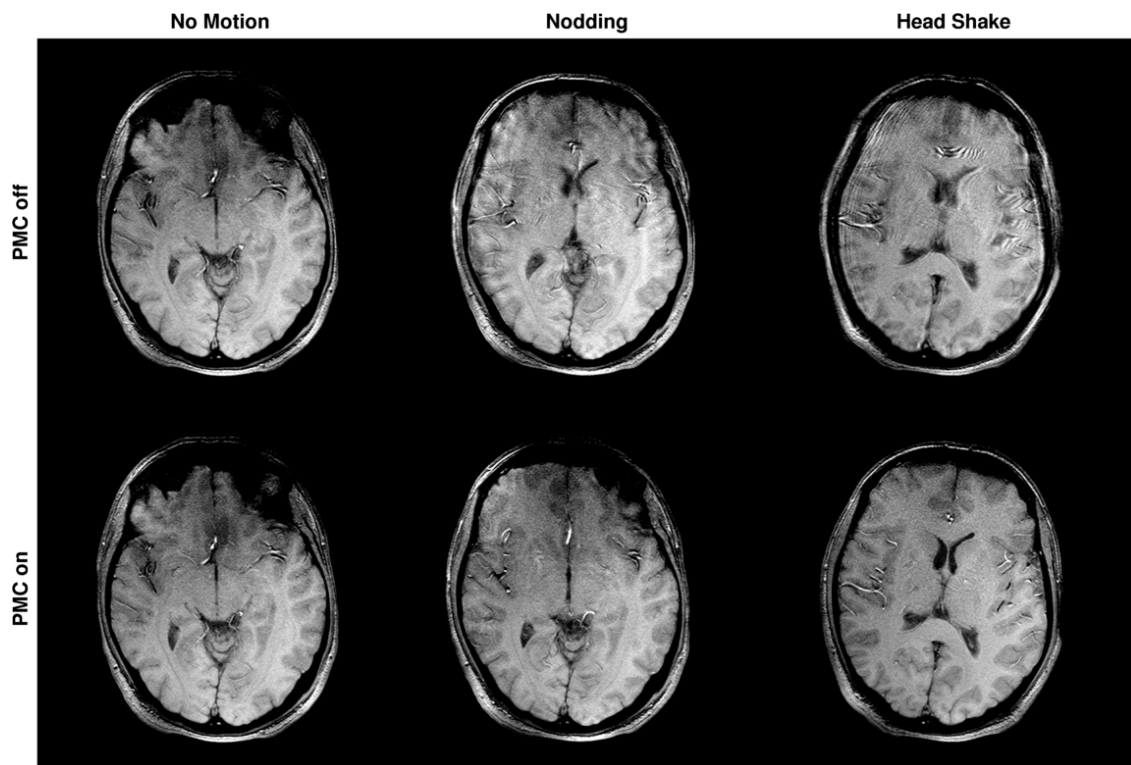# Results

Sequence 1: Multislice T_1w FFE

Calibration

The root-mean-squared error of the probe localization for the static setup varied between probes and amounted to $7 - 13$ μm (x), $13 - 17$ μm (y), and $18 - 22$ μm (z).

Update delay assessment

The update delay was not randomly distributed about its mean but exhibited a repetitive pattern of values ranging between 3 – 8 TR, which corresponds to 38–88 ms (data not shown).

In vivo experiments

Figure 25 illustrates the image reconstruction for the Multislice experiment. The top row shows the image quality for the three different motion tasks acquired without prospective motion correction. In the case without prescribed motion (left-hand column), the image quality is good. Sever motion artifacts are seen in the top row when a "head-shake" (center image) or a "nodding" (right-hand image) movement was done. Images acquired with real-time sequence updates are shown at the bottom. In the case without motion, the image quality is identical to the uncorrected case. The images in the center and on the right-hand side show successful prospective motion correction for the "head-shake" and the "nodding" motion. These images are free of conspicuous motion artifacts.

Figure 25: In vivo reconstruction of the Multislice T1w FFE sequence. For each experiment, one representative slice was selected. (top) Image reconstructions when prospective motion correction (PMC) was turned off. (bottom) Tones-based prospective motion correction results in very good image quality free of conspicuous motion artifacts. The corresponding motion patterns are illustrated in **Figure 26**.

Sequence 2: 3D T$_1$w FFE

Calibration

The root-mean-squared error of the probe localization for the static setup varied between probes and amounted to 5 – 9 µm (x), 15 – 18 µm (y), and 22 – 34 µm (z).

In vivo experiments

Figure 27 illustrates the results of the experiments using the 3D sequence. The top left image shows severe image artifacts due to motion, which is shown in the center and bottom plots on the left-hand side. The center and bottom plots in the center row show almost identical motion in the experiment with PMC. The resulting corrected image is shown in the center row at the top. The image quality has improved substantially. There are still residual ringing artifacts visible in the frontal lobe, which suggests residual errors in the sequence update.

The top right image shows the image quality in the experiment in which the volunteer was asked to remain still. It shows that the sequence update did not induce visible blurring (image on top row, center). There are some artifacts that can be explained by the unintended motion of the volunteer as measured by the field probes and illustrated in the rigid body parameter plots on the right-hand side. The motion in that scan amounted to approximately 2º and 2 mm, which is roughly twice the image resolution. The images look dark at the neck due to the applied REST slab.

The data were reformatted so as to show the image reconstructions in the sagittal and coronal plane, respectively, as illustrated in **Figure 28**.
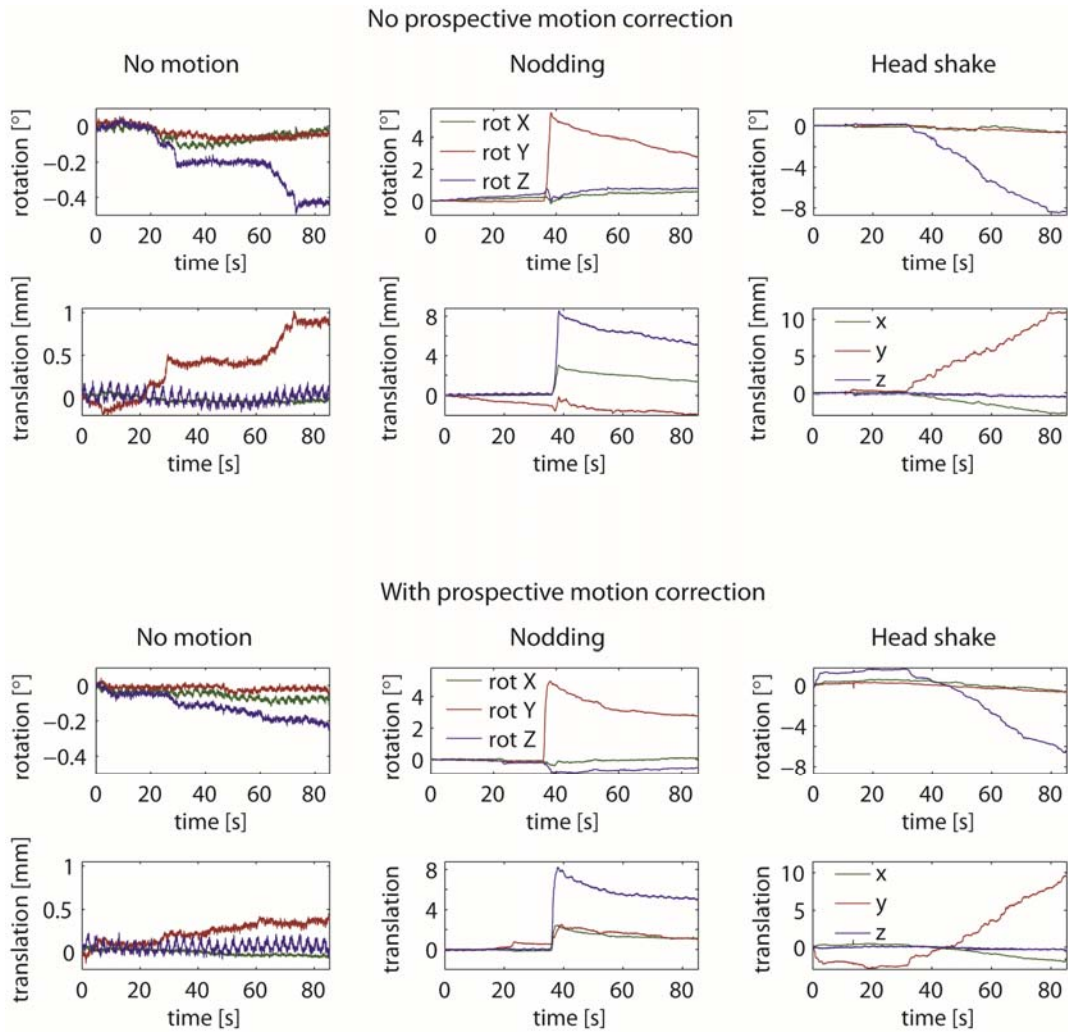
Figure 26: Euler angles and translation vectors for the Multislice sequence experiments. The prescribed motion patterns measured in the experiments with and without prospective motion correction, respectively, corresponded very well.
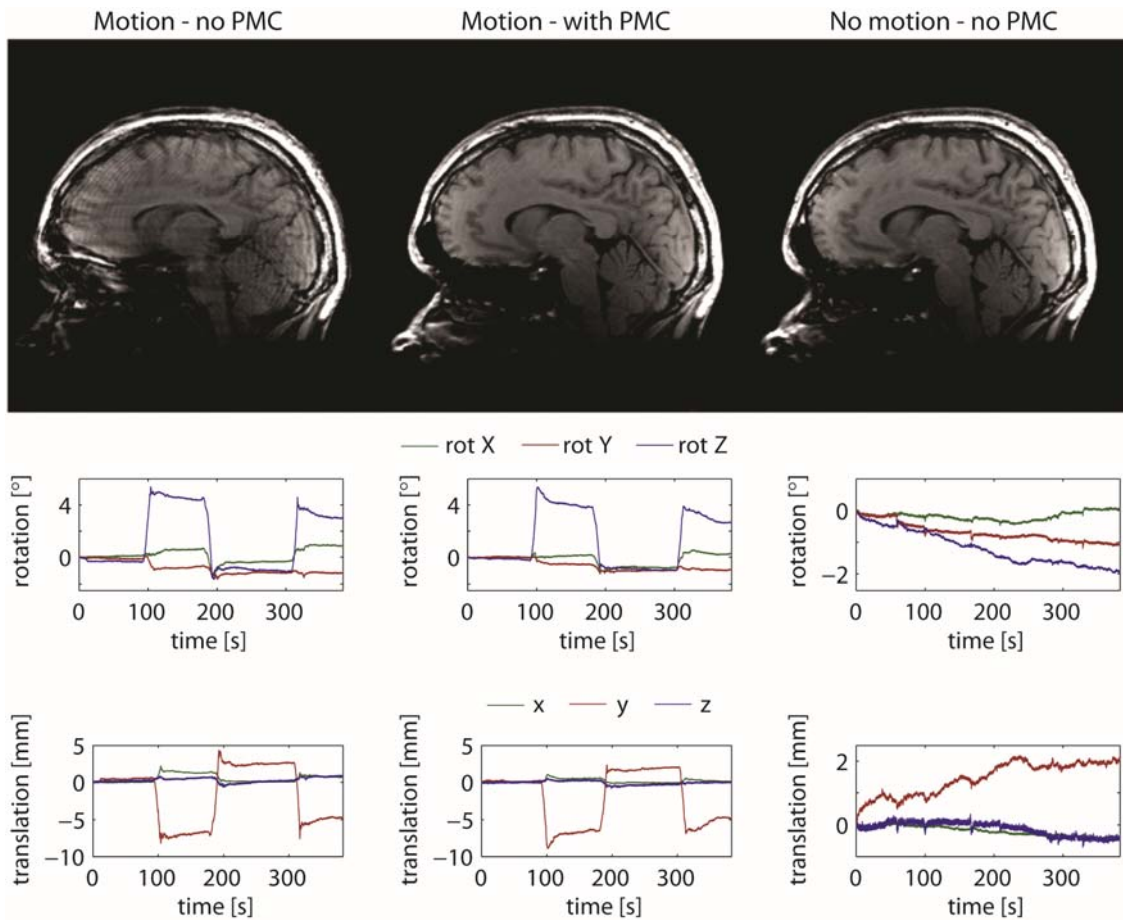
Figure 27: Results of the 3D sequence experiments. (top row) The image quality is severely degraded due to motion (left-hand image). Prospective motion correction with the proposed system successfully removes most of these artifacts (center image). Some residual ghosting is still visible, probably due to correction inaccuracies. The right-hand image shows a reference from an experiment where the subject was asked to remain still and no sequence update was performed. (center and bottom rows) The Euler angle and translation vector plots show that the realized motion in the two experiments (left and center) corresponded very well, allowing a fair comparison between the two. The right-hand motion patterns show motion of about 2° in the experiment where the volunteer was asked to remain still, which can explain the residual artifacts in the top right image.
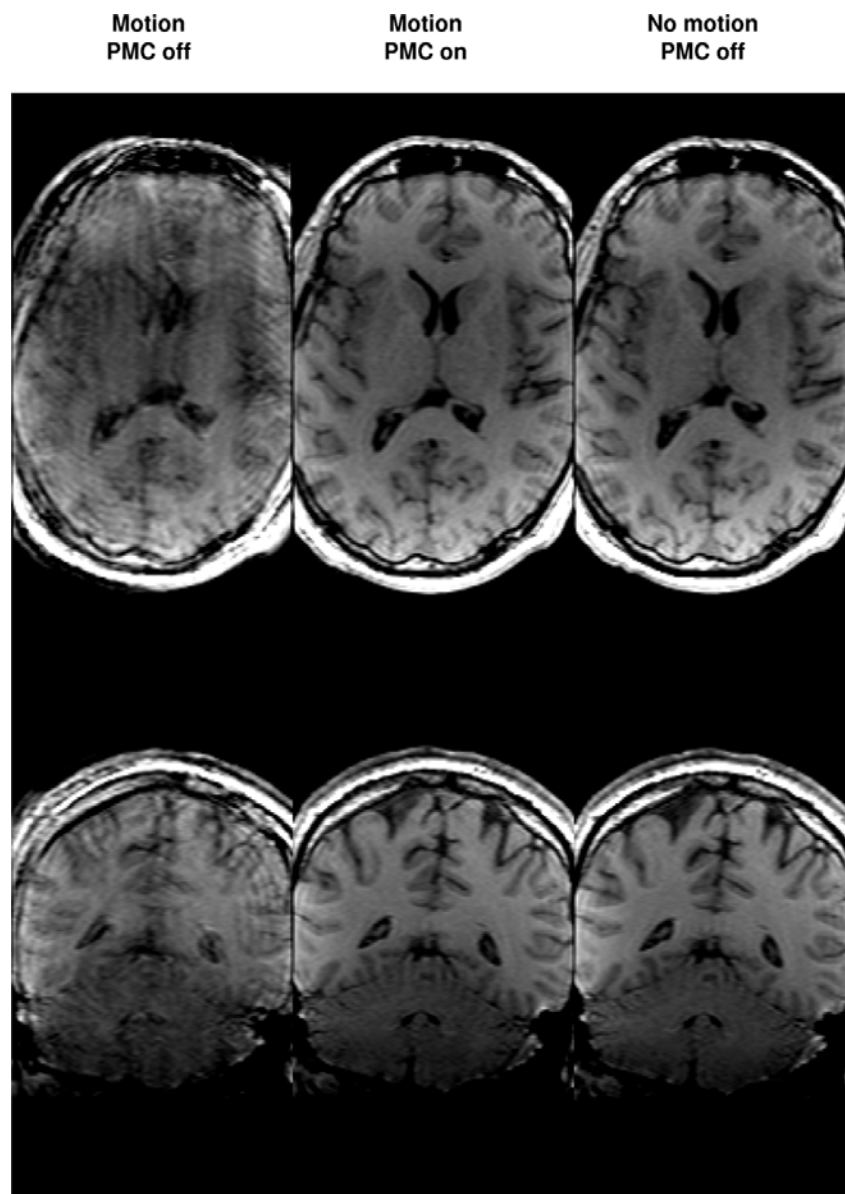
Figure 28: Image reconstructions in the sagittal and coronal planes for the 3D sequence experiments.

Discussion and Conclusion

The present work demonstrates the implementation of a novel design for gradient tone-based prospective motion correction that has been successfully applied to two clinically relevant sequences in vivo.

By placing the gradient tones into other sequence parts than the image-encoding segment, several key aspects have been enabled for routine clinical imaging. In this fashion, it's possible

to use the scanner's image reconstruction routine, which allows easy use and fast imaging results. Relying on calibrated or nominal k-space trajectories instead of applying concurrent field monitoring (Barmet, Zanche, and Pruessmann 2008), however, bears the intrinsic risk of residual imaging artifacts due to perturbations in the field encoding. Without concurrently monitoring the image encoding part of the sequence, field perturbations could be addressed by snapshot monitoring, which has recently been applied at 7T (S. Johanna Vannesjo, Wilm, et al. 2014).

The selected time windows for the gradient tones were chosen such that pre-filtering of the existing sequence gradients was avoided. This also allows to boost the method's sensitivity, which was improved to 5 – 34 µm (RMS) this work, by selecting either lower frequencies and leverage on the higher magnitude of the gradient system's transfer function or by increasing the tones frequencies without being limited to slew rate constraints imposed by sequence gradient activity.

However, these options rely on the availability of either gradient strength on the crusher plateau or sequence parts without gradient activity. Neither option may be available in certain sequences, which is a limitation of this approach. However, crusher gradients tend to be executed with limited gradient strength to avoid eddy currents during the subsequent image-encoding period, which suggests that the current solution may be widely applicable.

Moving the computation of the rigid body parameters onto an external system allowed imaging with arbitrary sequence TRs. External tracking systems have been widely used in prospective motion correction methods (Zaitsev et al. 2006; Aksoy et al. 2011; M. B. Ooi et al. 2009; Jessica Schulz et al. 2012) and is not fundamentally new. The latency of the sequence update loop in the present work was measured to vary between 30 – 80 ms. This is much longer than expected from the mere computation time of the rigid body parameters, which was measured to be of the order of a few milliseconds. Moreover, the latency is not constant but exhibits a time-dependent pattern. Considering the fact that neither the computation of the rigid body parameters on the external computer nor the assignment of these parameters to sequence variables on the host computer is performed within a real-time environment, such behavior can be expected. The analysis of the sources of the latency remains part of future work. Routing the rigid body parameters to the real-time sequence control program via the host computer should be avoided and a direct communication link to the sequence controller should be sought. Replacing the current operating system on the external computer is harder as the system is central to the method, in contrast to the host computer.

The application of this technology in routine head imaging requires substantial one-time investment into additional hardware and minor modifications to existing scanner software. Another important aspect regarding compatibility in routine head imaging is the head setup, which was not part of the numerous optimizations conducted in the present work. For the current head set design, the ear pads used for ear protection from acoustic noise were removed to allow larger head motion in the experiments with instructed motion. Ear protection was achieved with earplugs, which might violate safety instruction in clinical environments. Modifications to the existing head set design will be addressed in future work with emphasis on compatibility with a variety of head coil designs, and subject compatibility.

Control of noise propagation in parallel MRI

Motivation

Parallel imaging allows to increase the imaging speed of MR examinations by the use of receive coil arrays and image reconstruction techniques that exploit the intrinsic spatial encoding mechanism provided by the individual coils (Sodickson and Manning 1997; Pruessmann et al. 1999; Griswold et al. 2002). It allows undersampling k-space with respect to the Nyquist criterion, enabling shorter image acquisition periods. Shorter image acquisition periods have many benefits: They reduce susceptibility artifacts in applications using long imaging readouts such as EPI or spiral, allow shortening echo times (TE) and repetition times (TR) to increase image contrast and allow for a more efficient use of imaging time, which is of high importance in clinical practice. Last but not least, faster imaging speed is a viable, yet very limited, means of addressing motion artifacts which tend to increase with longer examinations.

However, shortening the acquisition duration with parallel imaging comes with a penalty in signal-to-noise ratio (SNR). The combination of sensitivity encoding, k-space undersampling and acquisition time reduction results in thermal noise in the image domain that is spatially dependent and increased compared to acquisition strategies that rely on fully sampled k-space data.

For Cartesian Fourier encoding strategies, the quantitative description of the resulting thermal noise in the image domain is described by the geometry factor ("g-factor"), which quantifies the increase in thermal noise at each location in the image domain compared to a fully sampled, Cartesian k-space sampling strategy (Pruessmann et al. 1999). The ability to compare two trajectories is due to few degrees of freedom they can be described by. It is the bandwidth of the readout direction and the constant spacing between adjacent phase encoding lines that renders the straightforward comparison of two trajectories possible. An additional feature of Cartesian trajectories is the structure of their point-spread function (PSF), which contains discrete peaks in the image domain and renders the numerical computation time of the g-factor numerically simple.

The same PSF consideration, however, renders Cartesian trajectories ill-suited for parallel imaging with k-space undersampling as the resulting g-factor map contains sharp transitions between areas with different noise amplification. This results in apparent image contrast of thermal origin, which may be misinterpreted as anatomical structures.

Additionally, Cartesian trajectories do not make any use of the encoding capability of the phase-encoding gradient during the passage along the frequency-encoding direction. It is very inefficient to use only one of the three gradient coils to perform image encoding. The reason for

this is that the required calibration of the field response is reduced to one dimension, which enables the accurate calibration of the resulting Fourier encoding for Cartesian readouts. Non-Cartesian image encoding strategies, on the other hand, make much more efficient use of the encoding capabilities of the gradient system. Spiral trajectories, for example, collect the necessary image information in k-space faster than Cartesian trajectories and have a PSF in the case of undersampling that promises more benign noise amplification in the image domain.

The analysis of noise performance in parallel imaging becomes more complicated in the case of non-Cartesian Fourier encoding. First, it becomes unclear what fully sampled reference the now arbitrary Fourier sampling pattern should be compared to. It is therefore better to consider image domain maps of the resulting noise standard deviation ("noise maps") than g-factor maps. Second, the numerical complexity of computing the noise maps becomes daunting, for reasons explained below, and needs to be tackled with efficient numerical methods that approximate the analytical solution available for Cartesian trajectories (Pruessmann et al. 1999). Third, the Fourier encoding of such trajectories is not reproducible accurately enough, which results in minute discrepancies between the desired and the actual gradient encoding acting on the image. This results in image artifacts that limit the acceptance of non-Cartesian MR imaging despite its many advantages for parallel MRI.

In practice, Cartesian trajectories are very efficiently implemented by EPI readouts. They allow fast k-space coverage and exhibit a very benign behavior when imaging in an inhomogeneous static magnetic background field (B_0), which results in a mere voxel shift along the phase-encoding direction. They are widely used in neuroimaging applications such as diffusion weighted imaging (DWI) or BOLD functional MRI (fMRI) for these reasons.

However, Cartesian EPI trajectories still suffer from very sharp transitions between areas of different noise amplification as described above. It is thus desirable to manipulate their sampling pattern such that their noise maps improve while keeping the advantages of EPI trajectories. Modifying k-space trajectories to improve the data acquisition speed, the noise and PSF performance of parallel MRI has been studied in the past. Based on the generalized sampling theorem by Papoulis (Papoulis 1977), Moriguchi and Duerk proposed to apply strong zigzag perturbations in the phase encoding direction of a Cartesian sampling strategy in order to skip phase encoding steps for faster data acquisition (Moriguchi and Duerk 2006). The same zigzag sampling strategy was used by Breuer (Breuer et al. 2008) to undersample k-space additionally along the frequency encoding direction to better exploit sensitivity variations for GRAPPA reconstructions. Moriguchi reported strongly decreased SNR behavior in his method, probably due to the use of a non SNR-optimal reconstruction technique. Furthermore, both methods used

a Cartesian sampling pattern in the phase encoding direction, which kept the striking noise structures in the resulting image reconstructions.

In 3D acquisitions, deviations from the Cartesian sampling pattern in a 2D plane are more easily attained as the effective encoding speed within that plane can be reduced without sacrificing scan time. This idea has been applied to homogenize and quantitatively improve g-factor maps (Bilgic et al. 2014).

The present work focuses on 2D image acquisition strategies due their widespread use in practice. As described above, knowing the actual image encoding during data acquisition is crucial for non-Cartesian image encoding. Concurrent field monitoring is a solution to that problem as it provides accurate accounts of the actual Fourier encoding acting on the object, thus circumventing time-consuming and unreliable k-space trajectory calibration and enabling well-informed image reconstruction. Therefore, concurrent field monitoring served as the basis for image reconstruction for all experiments described below.

This chapter concerns the manipulation of the PSF of EPI trajectories to specifically control noise propagation in parallel imaging. First, parallel imaging reconstruction is revisited to establish the basis for the rest of this chapter. Methods are described that allow for efficient computation of noise maps. Heuristic parameterizations are presented that allow sampling pattern manipulations while keeping the image reconstruction problem well-posed. Based on simulations, a set of 6 trajectories is used to perform experiments in vivo.

Parallel image encoding and reconstruction

The idea behind parallel imaging is to encode spatial information in receive coil sensitivities in parallel to Fourier encoding. As introduced in the introduction, the signal at the receive coil j is defined as follows:

$$m_j(t) = \int_{Volume} \rho(\boldsymbol{r})s_j(\boldsymbol{r})e^{i\gamma \int_0^t \sum_{n=0}^{N_p-1} c_n(\tau)f_n(\boldsymbol{r})d\tau + i\omega^{static}(\boldsymbol{r})t} d\boldsymbol{r} + \eta_j(t). \quad [50]$$

$\rho(\boldsymbol{r})$ denotes initial transverse magnetization, $s_j(\boldsymbol{r})$, the sensitivity profile of the receive coil j, and $\eta_j(t)$ denotes additive white Gaussian noise at the receive coil terminal at time t.

For the remainder of this chapter, the dynamic contribution of the phase encoding term will be expanded in 0th and 1st order of spherical harmonic terms. That is, $N_p = 3, f_0(\boldsymbol{r}) = 1, f_1(\boldsymbol{r}) = x, f_2(\boldsymbol{r}) = y, f_3(\boldsymbol{r}) = z$. Relying on 0th and 1st order terms only prompts the transformation of the

term $\gamma \int_0^t c_n(\tau)d\tau$ into the more familiar k-space representation, i.e. $\gamma \int_0^t c_n(\tau)d\tau = k_n(t)$. Rearranging terms yields

$$m_j(t) = \int_{Volume} \rho(\boldsymbol{r})s_j(\boldsymbol{r})e^{ik_0(t)}e^{i\boldsymbol{k}(t)\cdot\boldsymbol{r}}e^{i\omega^{static}(\boldsymbol{r})t}d\boldsymbol{r} + \eta_j(t). \qquad [51]$$

It is apparent in Eq. [51] that three encoding mechanisms act jointly on the image: The sensitivity encoding term $s_j(\boldsymbol{r})$, the encoding by different static off-resonance frequencies, $e^{i\omega^{static}(r)t}$, and the Fourier encoding term $e^{ik_0(t)}e^{i\boldsymbol{k}(t)\cdot\boldsymbol{r}}$. The three terms offer very different amount of room for individual optimization in a given imaging situation: The sensitivity profiles of receiver coils are given and change only if their load changes, which is negligible in typical imaging situations. The spatial dependence of the off-resonance term is given by the magnetization induced in the object and thus offers no room for optimization. However, the Fourier encoding term can be modified relatively easily by adjusting the temporal evolution of $\boldsymbol{k}(t)$. The gradient coils used to provide the temporal evolution of the Fourier term can be controlled very accurately over a bandwidth of approximately 30 kHz. It is therefore efficient to limit the image encoding optimization to the Fourier term and consider the other image encoding terms as known parameters.

It is beneficial to express the individual image encoding mechanisms by a single operator,

$$E_{j,t,\omega}(\boldsymbol{r}) = s_j(\boldsymbol{r})e^{ik_0(t)}e^{i\boldsymbol{k}(t)\cdot\boldsymbol{r}}e^{i\omega^{static}(r)t}, \qquad [52]$$

which leads to a more compact description of Eq. [51]:

$$m_j(t) = \int_{Volume} \rho(\boldsymbol{r})E_{j,t,\omega}(\boldsymbol{r})d\boldsymbol{r} + \eta_j(t). \qquad [53]$$

Combining the signals m_j obtained by the individual coils into one column vector yields the image encoding model

$$\boldsymbol{m}(t) = \int_{Volume} \rho(\boldsymbol{r})E_{t,\omega}(\boldsymbol{r})d\boldsymbol{r} + \boldsymbol{\eta}(t) \qquad [54]$$

where $\boldsymbol{m}(t) = \{m_1(t), m_2(t), \dots, m_{N_c}(t)\}^T$, $\boldsymbol{\eta}(t) = \{n_1(t), n_2(t), \dots, n_{N_c}(t)\}^H$. The subscript N_c denotes the number of receiver coils and the superscript H denotes the matrix transpose. For image reconstruction Eq. [54] is discretized in the image domain at locations $\boldsymbol{r} = \boldsymbol{r}_q$, with index $q = \{1, \dots, N\}$, and in the time domain at time points $t = t_\mu$, with index $\mu = \{1, \dots, N_c \cdot N_k\}$.

N denotes the number of pixels in the image, N_k denotes the number of acquired k-space samples and N_c denotes the number of receive coils. Using matrix notation and omitting indices, Eq. [54] reads as follows:

$$\boldsymbol{m} = E\rho + \boldsymbol{\eta}. \qquad [55]$$

The linear image reconstruction matrix F yielding the SNR optimal estimation of the image content $\rho(\boldsymbol{r}_q)$ on a discretized set of image space locations $\boldsymbol{r}_q$ measured at discrete time points $t = t_\mu$ was given by Pruessmann et al. (Pruessmann et al. 1999) and reads as follows:

$$F = (E^H \Psi^{-1} E)^{-1} E^H \Psi^{-1}. \qquad [56]$$

Ψ denotes the noise covariance between the receive coils. The reconstruction acts on both terms of the discretized image encoding model as follows:

$$F\boldsymbol{m} = \rho + F\boldsymbol{\eta}. \qquad [57]$$

Eq. [57] yields an SNR-optimal, unbiased estimator of ρ contaminated by thermal noise. The noise covariance matrix X in the reconstructed image is given as follows:

$$\mathrm{X} = F\boldsymbol{\eta}\boldsymbol{\eta}^H F^H. \qquad [58]$$

X is a matrix with N^2 columns and N^2 rows where N denotes the number of pixels in the image. In typical scenarios $N = 200,$ which renders the computation and storage of X prohibitive. However, the computation of its trace, i.e. its diagonal, is numerically feasible. The elements of the trace reflect the noise variance in that pixel but yield no information about the covariance of thermal noise among different pixels. This, however, is enough information to assess the noise performance of the image reconstruction.

The trace of X can be estimated by repeatedly performing the reconstruction on mere noise input and estimating the standard deviation of the magnitude in each pixel. Throughout this chapter, the noise analysis was limited to determining $\mathrm{X}'s$ trace and noise covariance terms were disregarded.

The reconstruction matrix F contains N^2 rows and $N_c \cdot N_k$ columns, which makes it practically impossible to store it in computer memory and hence prohibits a direct inversion. Instead, it was proposed to solve the inversion iteratively using the conjugate gradient (CG) algorithm (Pruessmann et al. 2001), which performs the inversion in a few iterations without the explicit

computation of parts of the reconstruction matrix F. Throughout this chapter, noise maps were computed using this iterative algorithm.

Parameterized perturbations of Cartesian EPI trajectories

Perturbing the sampling pattern of Cartesian EPI trajectories needs to be done carefully as a number of aspects need to be considered. First, to ensure comparability between the original Cartesian trajectory and the perturbed one, the readout duration must not be changed. This means that the perturbations can only be applied to the phase encoding gradient. Second, intrinsic slew rate and maximum strength limitations of the gradient system need to be met. Perturbations that are identical from one phase encoding line to the next will be less effective as they perturb the PSF only in the frequency encoding direction. Thus, in order to modify the PSF in both spatial dimensions they need to be different from one frequency encoding line to the next.

For the perturbations to effectively modify the sampling pattern's PSF, they need to cause substantial deviations from the underlying Cartesian pattern. For EPI trajectories considered here, that means that deviations in the phase encoding direction should be in the order of the Nyquist rate and above.

Sinusoidal perturbations are a good choice for this task. They are analytical and hence allow the rapid prototyping within scanner limitations. Sinusoids are eigenfunctions of gradient systems, which enables simple calibration and the conservation of the deviation pattern when played out on the gradient system. Furthermore, the task of modifying the resulting PSF in the phase encoding direction can be effectively achieved by advancing and delaying the sinusoids along the frequency encoding direction. This can be achieved easily by incorporating different phase shifts for each frequency encoding line. Due care has to be taken when invoking such phase shifts. They modify the sampling density in k-space, which may cause deteriorating noise behavior in the image reconstruction.

Methods

In all experiments, noise maps were computed by reconstructing an MR image using the iterative algorithm presented in (Pruessmann et al. 2001). Noise maps were calculated for different trajectories: Trajectory 1 ("Cart full") was a fully sampled Cartesian EPI, trajectory 2 ("Cart R4") was a Cartesian EPI with constant undersampling factor 4, trajectories 3-5 were dubbed "sine 05", "sine 15", and "sine 19" respectively, according to their different sine amplitudes. The amplitude labels ("05", "15", and "19", respectively) relate to their extent in k-

space measured in Nyquist intervals, i.e. "sine 05" was realized with a sine amplitude of 0.5 times the Nyquist rate. These trajectories did not perturb the PSF in phase encoding direction. Trajectories 6 and 7, dubbed "swing 1" and "swing 2", respectively, perturbed the PSF in both directions. **Figure 29** illustrates these trajectories as realized by the gradient system. The phase shifts in trajectories 6 and 7 were defined such that they described a sinusoidal function covering two periods from the first to the last phase encoding step. The amplitude of these sinusoidal "swings" was chosen to be 1/8 of the period of the sinusoids along the frequency direction for trajectory 6 and about 1/6 for trajectory 7.

The FOV covered by the trajectories was 23 cm, the resolution was 1.3 mm and the readout duration was 55 ms. All trajectories were single-shot.

Simulations

For the trajectories 2-4, and 7, k-space data were calculated by encoding a pre-existing reconstruction of an MR image of a head and adding complex-valued, white Gaussian noise to each receive coil output. Noise among receive coils was modeled as being uncorrelated. The noise magnitude was scaled such that the SNR at the highest k-space location was around 100 to ensure well-defined behavior of the CG iterations, which were stopped after 100 iterations. The encoding matrix contained 8 sensitivity profiles obtained from a pre-existing set of measured receive sensitivities of an 8-channel head array for 3T imaging (**Figure 30**).

48 averages were computed for each trajectory and the standard deviation was computed for the magnitude value in each pixel. For the Cartesian trajectory, the analytical g-factor map was computed using the same coil array and a reduction factor of 4 for comparison.
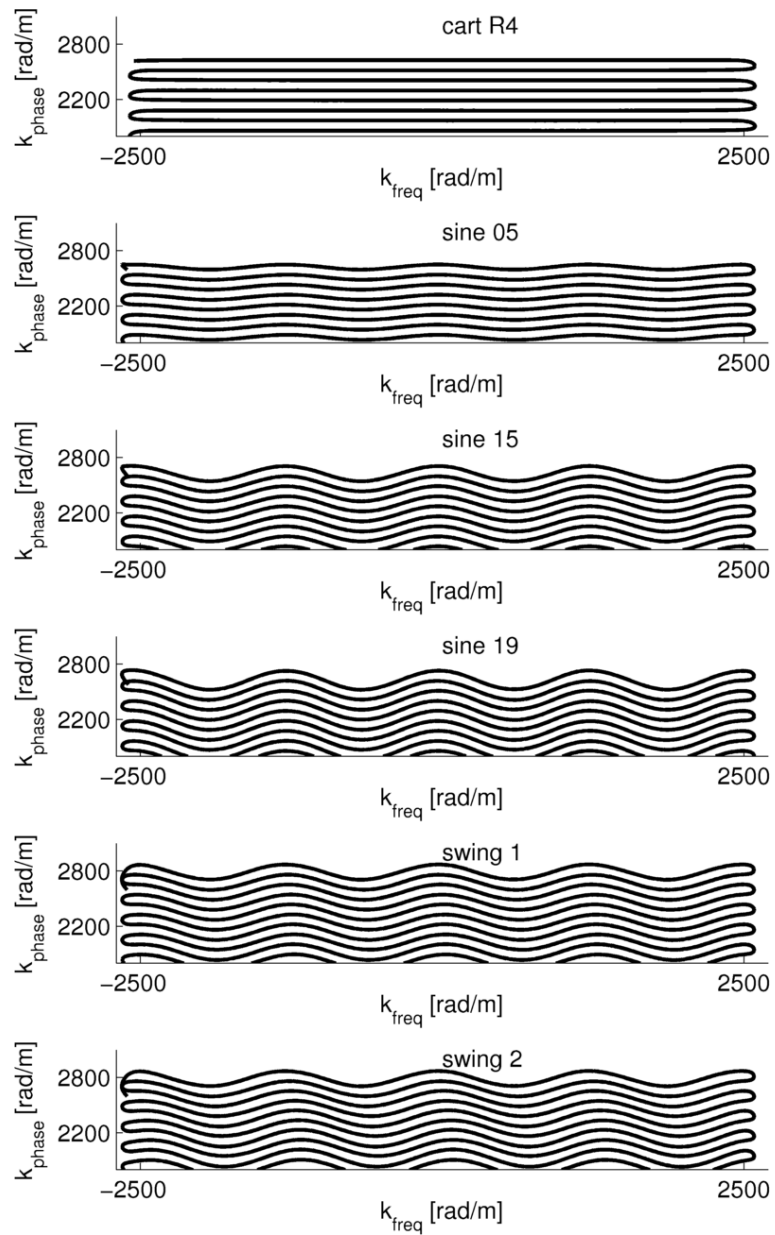
Figure 29: The measured k-space trajectories used in the in vivo experiments. Note the difference between the sine trajectories, which are perfectly phase coherent, and the swing trajectories that exhibit subtle yet noticeable phase offsets.
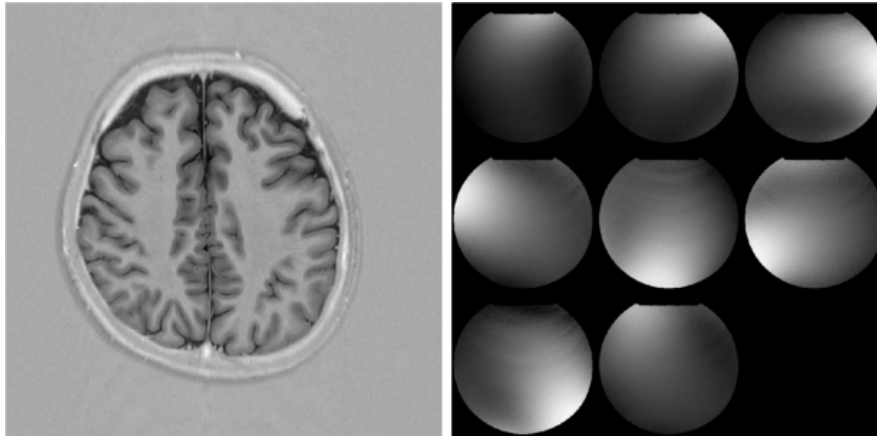
Figure 30: Image reconstruction vehicle (left) and the coil sensitivities used for the simulations (right). The vehicle was a magnitude image of an MR image of a head. The coil sensitivities were acquired on the same MR system with the same receive coil array used for the in vivo experiments.

In vivo experiments

Trajectories 2 – 7 were implemented and played out on a 3T Philips Achieva MR system. The prescribed gradient waveforms were pre-compensated with the gradient impulse response function (GIRF) of the scanner, which was measured by (Signe J. Vannesjo et al. 2013), mainly to correct for expected infidelities such as delays between the frequency encoding and phase encoding gradient coils and damping of the desired sine amplitudes. A healthy volunteer was scanned after giving informed consent. For imaging, a Philips 8-channel head coil was used. A B_0 map was acquired with two spin-warp acquisitions with two different TEs (6.6 ms, and 7.2 ms). The sensitivity maps were computed from the first spin-warp scan. For each trajectory, the experiment was repeated 100 times. The first 50 repetitions were acquired to obtain the vehicle image with the following sequence parameters: TR = 3 s, TE = 34 ms, slice thickness 4 mm, flip angle 80º, readout BW 367 kHz. The second 50 dynamics were done to obtain the noise data. In this case, the sequence parameters were identical to the previous experiment except TR = 500 ms and no RF excitation pulse was played out.

All experiments were done by applying the volume shim on the Philips platform and a SPIR pre-pulse for fat suppression was applied throughout.

Concurrently, field probe data were acquired using the field probe setup developed in this group (Barmet et al. 2010). It consisted of 16 ^{19}F field probes located on the receive coil array. The field probes acquired data throughout the entire EPI readout and were excited with external hardware. The field probe array was connected to the Philips spectrometer that was re-programmed to receive ^{19}F data. k-Space trajectories were computed by fitting the field probe signals to a 0th and 1st order model of spherical harmonics.

The image reconstruction was an iterative SENSE reconstruction with simultaneous B_0 correction by multi-frequency interpolation (Man, Pauly, and Macovski 1997). The iterative CG reconstruction approximated Eq. [56] and was aborted after 35 iterations. The image and field probe date used for the vehicle to reconstruct the noise images was chosen separately for each trajectory and was arbitrarily chosen to be from dynamic 25 for all noise averages.

Noise maps were computed by estimating the trace of the noise covariance matrix defined in Eq. [58]. The total noise content and the maximum SD value were computed for each map. The total noise content was defined as the root sum of squares (RSOS) of all SD values in the noise map. Then, the pixels of each noise map were sorted by value and their structure was analyzed.

Results

Simulations

Figure 31 illustrates the results of the noise map calculation for the four trajectories that were compared in this study. **Figure 31 (a)** was computed analytically as a control for the noise map of the Cartesian EPI shown in **Figure 31 (b)**, which correspond very well to one another. **Figure 31 (b-d)** show how the noise map is increasingly smeared out in frequency encoding direction as the amplitude of the sinusoidal perturbations was increased. **Figure 31 (e)** shows how the noise map can be effectively smeared out in the phase encoding direction by applying a varying phase shift along the same direction.
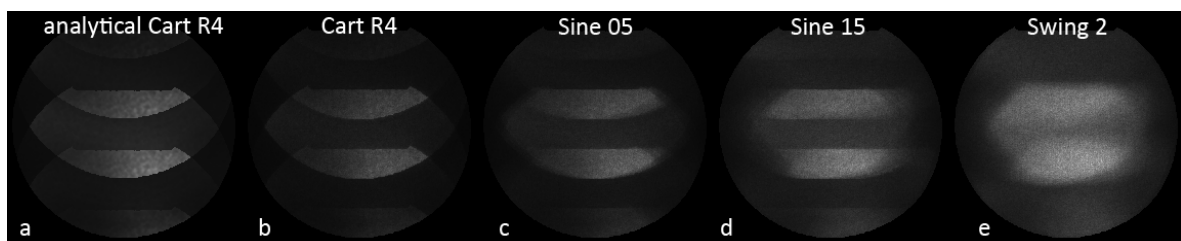
Figure 31: Simulation results for four different trajectories. The noise map is smeared out in frequency encoding direction with increasing sine amplitudes (b-d), and effectively smeared out in phase encoding direction when phase offsets between readout lines were applied (e). Very good quantitative correspondence of the simulation result of the Cartesian EPI (b) with the analytical result (a).

In vivo experiments

The top row in

Figure 33 shows the obtained noise maps in the in vivo experiments.

Figure 33 (a-d) show how the noise map was effectively smeared out in frequency encoding direction by applying sinusoids of increasing amplitudes, as expected from the simulations. Adding an additional phase offset that varied from one phase encoding line to the next ("swings") additionally caused noise map smearing along the phase encoding direction (e,f). The results from the in vivo experiments correspond very well to the results obtained in the simulations. The measured maximum SD that were calculated for the different imaging situations were very similar: the maximum SD was reduced by maximally 10%, and the total noise was reduced by maximally 4.5%. It can be noted, however, that all non-Cartesian trajectories except "sine 19" (shown in

Figure 33 (d)) performed favorably compared to the Cartesian trajectory, which exhibited a maximum SD value of 98.7. A similar result was obtained regarding the total amount of noise in the reconstructed image: All non-Cartesian trajectories except "swing 2" (shown in

Figure 33 (f)) performed better than the Cartesian trajectory with a total noise content of 72.28. **Figure 32** illustrates how the noise content is modified in each of the different experiments performed. The graph in **Figure 32** at the bottom left shows how non-Cartesian trajectories effectively reduce the pixel SD for pixels with already high SD, thus improving the sensitivity in areas where it is relatively low. However, the graph in **Figure 32** at the bottom right illustrates the opposite effect in pixels with relatively low SD values. In image regions with relatively low noise SD, the perturbed trajectories performed worse than the Cartesian trajectory as they increased the SD. This result illustrates that the main effect of perturbing Cartesian EPI trajectories as presented in this work is moving noise from image regions with high SD to regions with low SD. Altogether, total noise is slightly reduced with the non-Cartesian trajectories (cf. RSOS values in

Figure 33). **Figure 29** illustrates the measured k-space trajectories for the in vivo experiments. For illustration purposes, only parts of k-space are shown. They realized the prescribed trajectories with high fidelity, suggesting that pre-compensation with the GIRF is a very effective means to achieve a desired k-space sampling pattern. Very subtle differences in realized amplitudes of the sinusoids remained (data not shown), suggesting small residual imperfections of the calibration with the GIRF.

Figure 34 shows the B_0 and the sensitivity maps used for the in vivo image reconstruction.
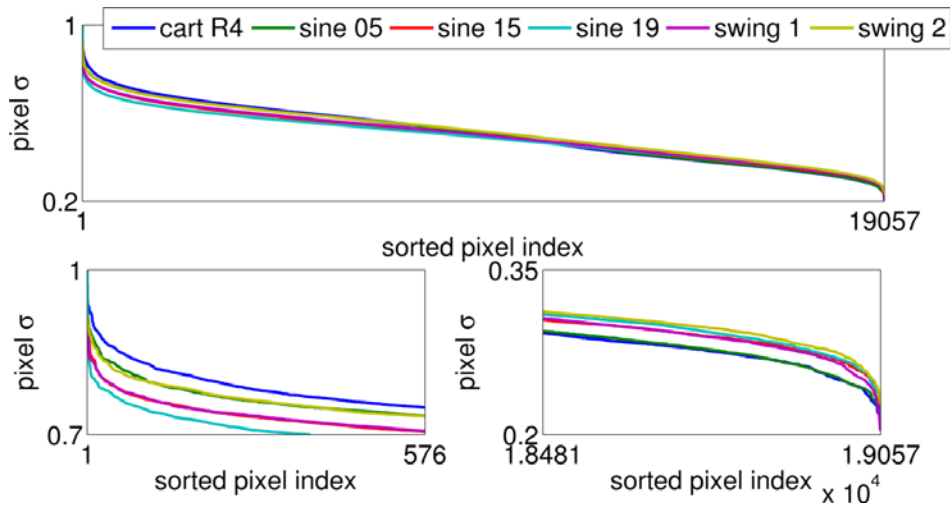
Figure 32: The distribution of the noise standard deviation values for all pixels, sorted by value. Top: Overview. Bottom left: The Cartesian trajectory (blue) exhibits larger values for high standard deviations than all perturbed trajectories. Bottom right: The Cartesian trajectory (blue) shows the smallest values for small standard deviations. This shows that there is negligible gain in total noise as the noise content merely gets smeared out from high to low values when perturbed trajectories are used.
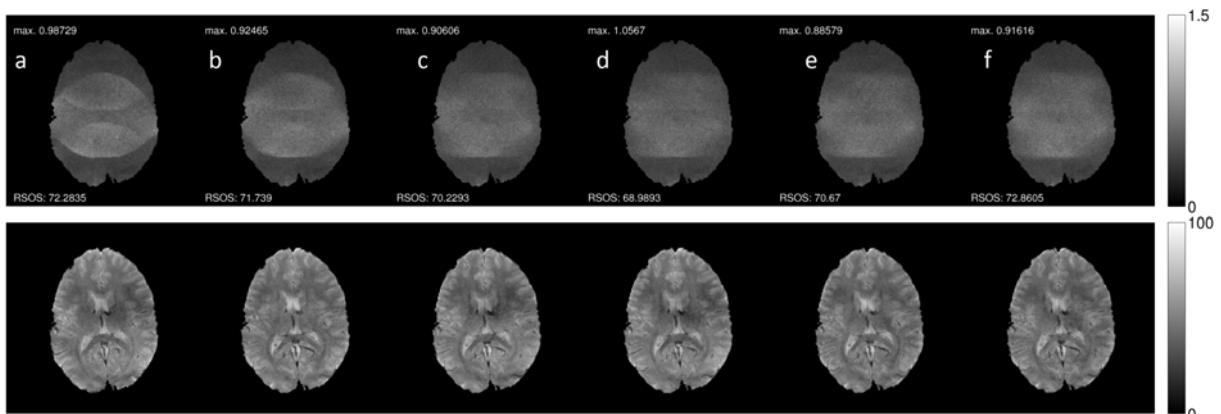
Figure 33: Noise maps (noise standard deviation) (top) and vehicle reconstructions (bottom) for the in vivo experiments. The trajectory labels from left to right are: "Cart R4" (a), "Sine 05" (b), "Sine 15"(c), "Sine 19" (d), "Swing 1" (e), and "Swing 2" (f), respectively.
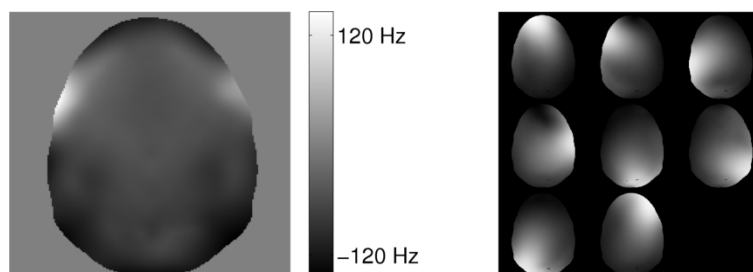
Figure 34: B_0 map (left) and sensitivity profiles (right) used in the in vivo experiments.

Discussion and Conclusion

In this chapter, it has been studied how sinusoidal perturbations in both frequency and phase encoding direction affect the noise behavior of parallel image reconstruction using SENSE. For this purpose, simple heuristic parameterizations of sinusoidal gradient waveforms were added to the phase encoding direction in order to modify the PSF of the resulting sampling pattern. The approach promised to improve overall sensitivity in terms of total thermal noise content in the resulting image, to improve sensitivity in image regions with relatively high thermal noise content and to smooth the spatial distribution of thermal noise in the image to reduce apparent image structures due to sharp transitions between image regions with different noise amplification.

The results presented in this chapter show that perturbing Cartesian EPI trajectories with a simple sinusoidal model is not able to substantially improve the sensitivity of parallel MR imaging using a SENSE reconstruction. Two measures, the maximum SD of thermal noise and the root sum-of-squares (RSOS) did not produce significant improvements. Despite the fact that for each measure, all but one of the studied non-Cartesian trajectories outperformed the Cartesian reference, the effect size of a few percent is too small to be regarded a relevant improvement.

These findings suggest that Cartesian EPI imaging is already very efficient for a 2D imaging situation using a circular receive coil array and relying on linear image reconstruction. This is somewhat unexpected given the fact that the trajectory only exploits sensitivity difference along its phase encoding direction.

It is further possible that the degrees of freedom offered by k-space sampling modifications, which only optimize the choreography of the linearly varying phase terms of the Fourier encoding mechanism, are not enough. Recently, it was shown that varying the Fourier encoding phase with highly non-linear functions may offer improved noise performance (Stockmann et al. 2010).

However, the perturbations employed in the present work were very effective at smearing out the noise distribution in both directions in the image while conserving the conditioning of the Cartesian trajectory. Enabled by concurrent field monitoring, it was possible to reconstruct images of non-Cartesian single-shot EPI trajectories without visible artifacts and smooth noise maps. The results presented in this work show that it has been possible to reduce the structure present in the final image to anatomical origin by reducing image artifacts with concurrent field monitoring and reducing thermal noise-induced structures by k-space trajectory design. This

may be very beneficial for example in clinical diffusion weighted MRI that use parallel imaging in conjunction with undersampled Cartesian EPI trajectories.

Conclusion and Outlook

Spatial non-linearity

This thesis presents the development of original concepts for field probe localization that rely on both the reliable reproduction of magnetic field dynamics by gradient coils as well as the high sensitivity of NMR field probes. It was shown that additional gradient tones can be superimposed onto existing gradient waveforms to achieve precisions of probe localization down to a few micrometers (< 10 μm with an amplitude of 6.5 mT/m, duration of 2 ms, and frequency 1.5 kHz). The computation of the probe's coordinates was based on a calibration model that incorporated dynamic fields of 0th and 1st spatial order. It was found that, for large probe displacements, localization errors were not limited by thermal noise but largely dominated by systematic effects (≈ 595 μm systematic error (RMS) vs. ≈ 30 μm precision (RMS) in the single probe tracking experiment). Such errors can be addressed by employing calibration models that consider field terms of higher spatial orders, which should fully capture systematic errors in situations where the input to the gradient coils in the time window used for probe localization does not vary over time (e.g., due to rotation of the input, or due to scaling of a trapezoid onto which a gradient tone is inserted). In the present work, such a situation occurred in the experiment with the 3D FFE sequence that contained a sequence window without gradient activity. It has to be noted, however, that in practice, such time windows are not common and thus merely extending the existing calibration model to spatial fields of higher polynomial orders won't suffice as other model violations come into play.

Non-linear gradient dynamics

One such confound is nonlinear gradient behavior, which has to be addressed by incorporating knowledge about the gradient waveforms onto which the gradient tones are superimposed. Initial measurements performed during this thesis suggest errors due to such non-linear behavior may be significantly larger than errors due to thermal noise. In practice, addressing this problem will often reduce to knowing the scaling and temporal order of trapezoids to describe the non-linear behavior of gradient systems. Whereas the non-linear output to gradient scaling can be calibrated offline, its occurrence within the sequence is only known shortly before the start of the scan (e.g., when deciding on a profile order). Since those information need to be transferred to the motion correction system if online sequence updates should be performed,

additional communication software or operator interaction will be required, which complicates its use.

In more general cases where the estimation of a trapezoid's scaling won't be sufficient, it is unclear if software approaches are adequate to correct for non-linear gradient behavior.

Coil-dependent field coupling

Another confound of field probe tracking accuracy that was not addressed in the present work is the rotational variance of the gradient system's transfer function. To this end, a tone or a native sequence waveform was calibrated for one gradient coil only. When rotated, the field response does not rotate exactly, which was disregarded in the present thesis. The successful motion correction results for both tones and the EPI sequence show that the thus incurred error is small for the studied examples. However, with increasing accuracy requirements systematic errors due to this assumption might become limiting. A possible solution is to perform the calibration of each coordinate-encoding gradient waveform for each gradient coil separately, yielding an extended calibration matrix of 12 coefficients per frequency (as opposed to currently 4). The calculation of the probe coordinates will be based on the knowledge or an estimate of the rotation applied to the gradient waveforms, and apply a linear combination of the calibration coefficients that had been obtained for each individual gradient coil. A full calibration of the gradient system's field response can be obtained very efficiently by applying triangular pulse shapes or frequency sweeps (Signe J. Vannesjo et al. 2013; S. Johanna Vannesjo, Dietrich, et al. 2014). A potential confound with that approach could be non-linear gradient behavior, which could be mitigated by performing the calibration with the gradient waveforms that will actually be used for field probe localization. This approach is tantamount to linearizing non-linear gradient behavior at the operating point, which is a common means used in engineering to improve the accuracy of control systems.

An important benefit of this approach to the current, "single-axis" calibration is its potentially higher accuracy for arbitrary rotations of the imaging slice. To this end, the orientation of the imaging slice at the beginning of the scan was aligned to the one used in the calibration, which greatly limited its flexible application in Chapters 2 and 3. This extended calibration will catalyze its use in imaging applications where the imaging sequence is known a priori. In applications that define the imaging sequence only immediately before each scan, for instance when resolution and FOV are optimized in each scan separately, the use of the gradient system's impulse response information could be a viable option. However, further work is necessary to

quantify the systematic calibration errors incurred due to the non-linear behavior of the gradient system.

Combining head- and coil-mounted field probe arrays

The accuracy of the probe localization may also be improved by abandoning calibration altogether. Instead, the field dynamics are simultaneously measured by an additional set of stationary field probes, located in the imaging volume's periphery, that monitor field dynamics in the laboratory frame. The motion correction system would then rely on the field evolution concurrently monitored by the static probe set in the laboratory frame to obtain the coordinates of the head-mounted field probes. In that fashion, the aforementioned confounding factors, in particular the non-linear gradient behavior, can be accounted for, which will result in more accurate localization of the head-mounted field probes.

However, such a dual setup provides benefits that go beyond replacing the calibration of the field probe localization. In Chapter 3 of this work, it was shown that head motion changes the local static off-resonance frequency of the head-mounted field probes. This causes errors in the image reconstruction due to errors in the field monitoring experiment. To address that issue, available sequence parts without gradient activity were exploited in Chapter 3 to update the estimation of the static off-resonance frequency. This approach might not be an option if such sequence parts are not available. Instead, the concurrently monitored dynamic fields of the static field probe array may be used for image reconstruction. Since the static field probe array is farther away from the moving head, motion will affect the off-resonance frequencies of the static probe array to a lesser degree than they affected head-mounted probes.

An additional important benefit of a set of static field probes in the periphery of the imaging volume is its potential to account for image distortions due to spatial gradient non-linearity. In the presence of bulk motion of the head, these change dynamically and need to be accounted for. In principle, this would also be possible with a head-mounted probe array but the requirement to mount more field probes on the head setup (9 field probes for full 2nd order, and 16 field probes for full 3rd order field monitoring), and the higher instability of the static off-resonance frequency of head-mounted field probes, render that approach impractical.

Relying on an additional field probe array for concurrent field monitoring frees the head-mounted probe array from its field-monitoring task (for which it was used in Chapters 2 and 3). This provides the benefit that each of the two probe arrays may be designed individually. In this fashion, for example, the head-mounted field probes could contain a substantially larger NMR

sample, which increases SNR that can be traded in for smaller tone amplitudes, shorter tone durations, and higher motion update rates.

Beyond field monitoring, another benefit of an additional static field probe array is the ability to perform dynamic shimming in parallel to motion correction. On its own, dynamic shimming using NMR field probes has been successfully performed incorporating spatial dynamic field evolutions of up to 3rd order (Duerst et al. 2014). The implementation presented in Duerst et al.'s work followed a similar approach to the one presented in the present thesis in the Chapter on clinically feasible applications of gradient tones. In both, the scanner's image reconstruction pipeline was unaware of the fact the sequence was adaptively modified, and both approaches relied on the same hardware and software framework. A combination of these two methods will be of very high interest in ultra-high field (7T and above) anatomical head imaging in which both bulk motion and physiological field fluctuations, but not gradient encoding errors, constitute limiting factors.

Correcting for other image encoding terms

This thesis addressed motion-induced inconsistencies in the excitation volume and in the gradient encoding terms. It did not address inconsistencies in the background field pattern $B_0(r)$, and receive sensitivity profiles $B_1^-(r)$. Due to their spatial variability, they are more complex than rigid body motion and much harder to correct. However, once bulk motion and spatial gradient non-linearity have been accurately corrected for, they are going to be the next limiting factors in image quality in neuroimaging applications such as fMRI and DWI. Regarding the correction of the sensitivity profiles, the alternative of choosing a k-space sampling strategy that allows co-encoding the sensitivity profiles and the image content needs to be juxtaposed to retrospectively rotating and translating a set of sensitivity profiles obtained in a preceding calibration scan (Bammer, Aksoy, and Liu 2007). The latter approach is much simpler and seems to be robust in the case of small motion despite its assumption of rotational invariance of the sensitivity profiles with respect to head motion. Co-encoding strategies require modifications to the imaging sequence (k-space sampling pattern) and are limited to single-shot sequences (if additional scan time needs to be avoided), which are predominantly used in BOLD fMRI. In such an imaging scenario, motion will result in complex-valued image modulations that reflect both the sensitivity profile (transmit and receive profiles) and local B_0. Further work is required to disentangle these modulations from the image content.

Application to clinically relevant sequences

The developments towards applying gradient tones to clinically relevant sequences has benefitted greatly from the omission of concurrent field monitoring, which allowed decoupling the sequence TR from the update rate of the motion updates and the use of product software for image reconstruction. In this approach, gradient tones need be inserted into non-image encoding sequence parts that contain no frequency content at the tones frequencies. All short-TR, spin-warp based sequences in the clinical domain contain crushing, prephasing, or balancing gradients that can be exploited for field probe tracking with gradient tones, making the insertion of tones relatively straightforward. Typically, the available time windows are shorter than the ones used in the present work (≥ 1.4 ms), which can be compensated with slightly larger diameters of the field probe's NMR active sample. To minimize potential field oscillations during the image encoding period, gradient pre-emphasis could be applied, as previously done for shim coils (Signe Johanna Vannesjo, Dietrich, et al. 2012).

In DWI applications, a persistent problem is motion during the diffusion-sensitizing gradients, which leads to irrecoverable signal dropouts. Recently, Herbst et al. (Herbst et al. 2012) have proposed to "continuously" update the diffusion encoding gradient based on optical head pose estimates. Field-probe based motion correction for such an application is very demanding. Small gradient tones may be played out along the diffusion-encoding gradients. This, however, affects diffusion encoding. It remains to be seen if field probe design can be optimized such that the amplitude of the tones may be small enough to be negligible for diffusion encoding. Alternatively, the refocusing gradient of the slice selective gradient immediately before the diffusion gradient may be extended with gradient tones and an estimate of the velocity of the head pose may be used as a 1ˢᵗ-order approximation of motion during the diffusion encoding gradient, which could be extrapolated to the diffusion-encoding period.

Improving the performance of the external tracking system

The present thesis relied on instructed motion to show the efficacy of the proposed motion correction methods. That motion was chosen to be relatively large ($\approx 8°$ rotation) and slow. In this fashion, it was possible to show the efficacy of the novel concepts proposed in this work. However, typical motion in clinical settings is smaller, and more abrupt. To get systematic improvements when correcting small motion, the method's sensitivity needs to be considered, which should not be difficult to improve when necessary, as discussed above (larger field probes, larger tones amplitudes, etc.). Relatively fast, abrupt motion needs to be addressed with reducing latency, which was measured to be approximately $30 - 80$ ms. This is several times

larger than the time window used for localization (1.4 – 4.8 ms). Importantly, the latency is not dominated by computation time on the external motion correction system, but by communication delays. This suggests that there is ample room to reduce latency down to a level where signal-processing steps start to dominate. Different options are possible to reduce the communication delays, which are related to the shortcomings of the current design. First, the update delay was not constant but exhibited a distinct temporal structure, suggesting interference from the operating systems running on the external spectrometer and the host computer. Interference from the external spectrometer's operating system can be avoided by implementing the calculations in a real-time environment, for instance by implementing them directly on the FPGA architecture. Second, the communication was routed via the scanner's host computer, which is unnecessary and should be avoided in future work. The host computer performs unimportant data conversion operations on an operating system without real-time performance, which is likely to have contributed to the latency. However, the option to directly communicate with the real-time sequence controller of the MR system used in the present work is not available yet and its implementation requires a collaborative effort with the manufacturer.

The computation time for probe coordinate determination on the external motion correction system used in Chapter 4 was estimated to be around 2 – 4 ms for window durations of 1.4 ms and a bandwidth of 1 MHz. As the signal bandwidth linearly affects computation time, its optimization will have impact if it's considered in future work, in particular for field probe tracking using long EPI or spiral readouts. Typical bandwidths of EPI and spiral waveforms are no wider than 15 – 20 kHz, which allows substantial downsampling of the field probe phase data to reduce computation time. Assuming a bandwidth of 20 kHz, computation time per millisecond field probe phase data can be reduced by a factor of 50, which is of particular interest if long readouts are used to encode the field probe position.

Pose extrapolation using predictive filters

Erroneous sequence update due to latency can be addressed by extrapolating the head pose in time. In order to capture abrupt motion, predictions will need to incorporate estimates of the velocity, and perhaps the acceleration, of the head pose's six degrees of freedom. The best choice of predictive filter for motion correction will depend on the SNR position determination. It seems that in most cases involving field probes SNR is high, as seen in the examples using gradient tones and an EPI sequence. However, there are also cases not yet considered that may exhibit variable SNR. Such a situation occurs, for example, if probe-based motion correction is to be performed using the intrinsic content of spin-warp sequences whose phase-

encoding gradients become very small as the k-space center is sampled. Predictive filters such as the Kalman could be used to reliably extrapolate the field probe coordinates in the phase encoding direction to ensure well-conditioned motion correction for spin-warp sequences using their intrinsic properties.

Head setup design and interface

The effectiveness of these methods relies crucially on the head setup's ability to maintain a rigid relationship to the head, and to ensure the same among the field probes. The current head setup was thus designed to be both light and rigid. The rigidity requirement is essential and may be violated in the case of mechanical interaction of the head setup with the head coil or the subject's head. In order to avoid the former, the head setup should be designed such that it does not touch the head coil in the presence of a few degrees of rotational motion, which requires minimizing the setup's thickness. This, in turn, demands that the field probes be more tightly integrated into the head frame. In order to avoid interaction with moving structures on the head, it is important to minimize scalp motion due to friction at the contact point between the backside of the head and the receive coil. The development of optimized padding for that region requires further work. If it turns out that scalp motion at that point cannot be reduced to an acceptable degree, the head setup design could be modified such that mechanical coupling between the moving scalp and the head setup is minimized, which could be obtained by combining flexible structures with rigid frames.

This work employed field probes that were connected to the receiver hardware via coaxial cables. In this fashion, receive path separation and low losses were achieved. Even if not a problem in the experiments done in the scope of this thesis, high currents on the coaxial cables could be a safety risk for the subject if placed very close to his or her body. More work will be required to ensure safe operation of wired cables in clinical settings. Cable routing was facilitated by the available openings between adjacent coil elements in the receiver, which might not be available in other coil designs. An obvious design modification is to route cables through the same opening the head is put in, which is identical to the routing of the acoustic wave guides attached to current head phone products. This design would come at a cost of sensitivity as thermal noise increases with longer transmission lines. However, the expected loss amounts to tens of percent, which is acceptable for practical applications given the current sensitivity of field probe tracking.

References

Addy, Nii Okai, Holden H. Wu, and Dwight G. Nishimura. 2012. "A Simple Method for MR Gradient System Characterization and K-Space Trajectory Estimation." *Magnetic Resonance in Medicine : Official Journal of the Society of Magnetic Resonance in Medicine / Society of Magnetic Resonance in Medicine* 68 (1): 120–29. doi:10.1002/mrm.23217.

Aksoy, Murat, Christoph Forman, Matus Straka, Tolga Çukur, Joachim Hornegger, and Roland Bammer. 2012. "Hybrid Prospective and Retrospective Head Motion Correction to Mitigate Cross-Calibration Errors." *Magnetic Resonance in Medicine* 67 (5): 1237–51. doi:10.1002/mrm.23101.

Aksoy, Murat, Christoph Forman, Matus Straka, Stefan Skare, Samantha Holdsworth, Joachim Hornegger, and Roland Bammer. 2011. "Real-Time Optical Motion Correction for Diffusion Tensor Imaging." *Magnetic Resonance in Medicine : Official Journal of the Society of Magnetic Resonance in Medicine / Society of Magnetic Resonance in Medicine* 66 (2): 366–78. doi:10.1002/mrm.22787.

Aksoy, Murat, Chunlei Liu, Michael E. Moseley, and Roland Bammer. 2008. "Single-Step Nonlinear Diffusion Tensor Estimation in the Presence of Microscopic and Macroscopic Motion." *Magnetic Resonance in Medicine* 59 (5): 1138–50. doi:10.1002/mrm.21558.

Anderson, Adam W., and John C. Gore. 1994. "Analysis and Correction of Motion Artifacts in Diffusion Weighted Imaging." *Magnetic Resonance in Medicine* 32 (3): 379–87. doi:10.1002/mrm.1910320313.

Andrews-Shigaki, Brian C., Brian S.R. Armstrong, Maxim Zaitsev, and Thomas Ernst. 2011. "Prospective Motion Correction for Magnetic Resonance Spectroscopy Using Single Camera Retro-Grate Reflector Optical Tracking." *Journal of Magnetic Resonance Imaging* 33 (2): 498–504. doi:10.1002/jmri.22467.

Atkinson, David, Derek L.G. Hill, Peter N.R. Stoyle, Paul E. Summers, Stuart Clare, Richard Bowtell, and Stephen F. Keevil. 1999. "Automatic Compensation of Motion Artifacts in MRI." *Magnetic Resonance in Medicine* 41 (1): 163–70. doi:10.1002/(SICI)1522-2594(199901)41:1<163::AID-MRM23>3.0.CO;2-9.

Bammer, Roland, Murat Aksoy, and Chunlei Liu. 2007. "Augmented Generalized SENSE Reconstruction to Correct for Rigid Body Motion." *Magnetic Resonance in Medicine* 57 (1): 90–102. doi:10.1002/mrm.21106.

Bandettini, Peter A., Eric C. Wong, R. Scott Hinks, Ronald S. Tikofsky, and James S. Hyde. 1992. "Time Course EPI of Human Brain Function during Task Activation." *Magnetic Resonance in Medicine* 25 (2): 390–97. doi:10.1002/mrm.1910250220.

Barmet, Christoph, Nicola De Zanche, Bertram J. Wilm, and Klaas P. Pruessmann. 2009. "A Transmit/receive System for Magnetic Field Monitoring of in Vivo MRI." *Magnetic Resonance in Medicine* 62 (1): 269–76. doi:10.1002/mrm.21996.

Barmet, Christoph, Bertram Wilm, Matteo Pavan, Georgios Katsikatsov, Jochen Keupp, Giel Mens, and Klaas P. Pruessmann. 2010. "Concurrent Higher-Order Field Monitoring for Routine Head MRI: An Integrated Heteronuclear Setup." In *Proceedings of the 18th Scientific Meeting, International Society for Magnetic Resonance in Medicine, Stockholm, Sweden*, 216.

Barmet, Christoph, Nicola De Zanche, and Klaas P. Pruessmann. 2008. "Spatiotemporal Magnetic Field Monitoring for MR." *Magnetic Resonance in Medicine* 60 (1): 187–97. doi:10.1002/mrm.21603.

Batchelor, P. G., D. Atkinson, P. Irarrazaval, D. L. G. Hill, J. Hajnal, and D. Larkman. 2005. "Matrix Description of General Motion Correction Applied to Multishot Images." *Magnetic Resonance in Medicine* 54 (5): 1273–80. doi:10.1002/mrm.20656.

Bilgic, Berkin, Borjan A. Gagoski, Stephen F. Cauley, Audrey P. Fan, Jonathan R. Polimeni, P. Ellen Grant, Lawrence L. Wald, and Kawin Setsompop. 2014. "Wave-CAIPI for Highly Accelerated 3D Imaging." *Magnetic Resonance in Medicine*, July, n/a – n/a. doi:10.1002/mrm.25347.

Bloch, F. 1946. "Nuclear Induction." *Physical Review* 70 (7-8): 460–74. doi:10.1103/PhysRev.70.460.

Breuer, Felix A., Hisamoto Moriguchi, Nicole Seiberlich, Martin Blaimer, Peter M. Jakob, Jeffrey L. Duerk, and Mark A. Griswold. 2008. "Zigzag Sampling for Improved Parallel Imaging." *Magnetic Resonance in Medicine* 60 (2): 474–78. doi:10.1002/mrm.21643.

Brown, Timothy T., Joshua M. Kuperman, Matthew Erhart, Nathan S. White, J. Cooper Roddey, Ajit Shankaranarayanan, Eric T. Han, Dan Rettmann, and Anders M. Dale. 2010. "Prospective Motion Correction of High-Resolution Magnetic Resonance Imaging Data in Children." *NeuroImage* 53 (1): 139–45. doi:10.1016/j.neuroimage.2010.06.017.

Buerger, Christian, Tobias Schaeffter, and Andrew P King. 2011. "Hierarchical Adaptive Local Affine Registration for Fast and Robust Respiratory Motion Estimation." *Medical Image Analysis* 15 (4): 551–64. doi:10.1016/j.media.2011.02.009.

Derbyshire, J. A., G. A. Wright, R. M. Henkelman, and R. S. Hinks. 1998. "Dynamic Scan-Plane Tracking Using MR Position Monitoring." *Journal of Magnetic Resonance Imaging* 8 (4): 924–32.

De Senneville, Baudouin Denis, Charles Mougenot, and Chrit T.W. Moonen. 2007. "Real-Time Adaptive Methods for Treatment of Mobile Organs by MRI-Controlled High-Intensity Focused Ultrasound." *Magnetic Resonance in Medicine* 57 (2): 319–30. doi:10.1002/mrm.21124.

De Zanche, Nicola, Christoph Barmet, Jurek A. Nordmeyer-Massner, and Klaas P. Pruessmann. 2008. "NMR Probes for Measuring Magnetic Fields and Field Dynamics in MR Systems." *Magnetic Resonance in Medicine* 60 (1): 176–86. doi:10.1002/mrm.21624.

Dietrich, Benjamin, Christoph Barmet, David Brunner, and Klaas P. Pruessmann. 2011. "An Autonomous System for Continuous Field Monitoring with Interleaved Probe Sets." In *Proceedings of the 19th Scientific Meeting, International Society for Magnetic Resonance in Medicine, Montreal, Canada*, 1842. Montreal, Quebec, Canada.

Duerst, Yolanda, Bertram J. Wilm, Benjamin E. Dietrich, S. Johanna Vannesjo, Christoph Barmet, Thomas Schmid, David O. Brunner, and Klaas P. Pruessmann. 2014. "Real-Time Feedback for Spatiotemporal Field Stabilization in MR Systems." *Magnetic Resonance in Medicine*, March, n/a – n/a. doi:10.1002/mrm.25167.

Dumoulin, C. L., S. P. Souza, and R. D. Darrow. 1993. "Real-Time Position Monitoring of Invasive Devices Using Magnetic Resonance." *Magnetic Resonance in Medicine* 29 (3): 411–15.

Duyn, Jeff H., Yihong Yang, Joseph A. Frank, and Jan Willem van der Veen. 1998. "Simple Correction Method for K-Space Trajectory Deviations in MRI." *Journal of Magnetic Resonance* 132 (1): 150–53. doi:10.1006/jmre.1998.1396.

Ebisu, Toshihiko, Chuzo Tanaka, Masahiro Umeda, Makoto Kitamura, Shoji Naruse, Toshihiro Higuchi, Satoshi Ueda, and Hiroshi Sato. 1996. "Discrimination of Brain Abscess from Necrotic or Cystic Tumors by Diffusion-Weighted Echo Planar Imaging." *Magnetic Resonance Imaging* 14 (9): 1113–16. doi:10.1016/S0730-725X(96)00237-8.

Edelstein, W. A., J. M. S. Hutchison, G. Johnson, and T. Redpath. 1980. "Spin Warp NMR Imaging and Applications to Human Whole-Body Imaging." *Physics in Medicine and Biology* 25 (4): 751. doi:10.1088/0031-9155/25/4/017.

Ehman, R L, and J P Felmlee. 1989. "Adaptive Technique for High-Definition MR Imaging of Moving Structures." *Radiology* 173 (1): 255–63.

Filipovic, M., P.-A. Vuissoz, A. Codreanu, M. Claudon, and J. Felblinger. 2011. "Motion Compensated Generalized Reconstruction for Free-Breathing Dynamic Contrast-Enhanced MRI." *Magnetic Resonance in Medicine* 65 (3): 812–22. doi:10.1002/mrm.22644.

Forman, Christoph, Murat Aksoy, Joachim Hornegger, and Roland Bammer. 2011. "Self-Encoded Marker for Optical Prospective Head Motion Correction in MRI." *Medical Image Analysis* 15 (5): 708–19. doi:10.1016/j.media.2011.05.018.

Fu, Z. W., Y. Wang, R. C. Grimm, P. J. Rossman, J. P. Felmlee, S. J. Riederer, and R. L. Ehman. 2005. "Orbital Navigator Echoes for Motion Measurements in Magnetic Resonance Imaging." *Magnetic Resonance in Medicine* 34 (5): 746–53.

Griswold, Mark A., Peter M. Jakob, Robin M. Heidemann, Mathias Nittka, Vladimir Jellus, Jianmin Wang, Berthold Kiefer, and Axel Haase. 2002. "Generalized Autocalibrating Partially Parallel Acquisitions (GRAPPA)." *Magnetic Resonance in Medicine* 47 (6): 1202–10. doi:10.1002/mrm.10171.

Haeberlin, Maximilian, Lars Kasper, Christoph Barmet, David O. Brunner, Benjamin E. Dietrich, Simon Gross, Bertram J. Wilm, Sebastian Kozerke, and Klaas P. Pruessmann. 2014. "Real-Time Motion Correction Using Gradient Tones and Head-Mounted NMR Field Probes." *Magnetic Resonance in Medicine*, September, n/a – n/a. doi:10.1002/mrm.25432.

Herbst, Michael, Julian Maclaren, Matthias Weigel, Jan Korvink, Juergen Hennig, and Maxim Zaitsev. 2012. "Prospective Motion Correction with Continuous Gradient Updates in Diffusion Weighted Imaging." *Magnetic Resonance in Medicine* 67 (2): 326–38. doi:10.1002/mrm.23230.

Jezzard, Peter, and Robert S. Balaban. 1995. "Correction for Geometric Distortion in Echo Planar Images from B0 Field Variations." *Magnetic Resonance in Medicine* 34 (1): 65–73. doi:10.1002/mrm.1910340111.

Kasper, Lars, Maximilian Haeberlin, Benjamin E. Dietrich, Simon Gross, Christoph Barmet, Bertram J. Wilm, S. Johanna Vannesjo, et al. 2014. "Matched-Filter Acquisition for BOLD fMRI." *NeuroImage*. Accessed June 17. doi:10.1016/j.neuroimage.2014.05.024.

Klein, Saskia, Lars Kasper, Signe Johanna Vannesjo, Maximilan Haeberlin, Simon Gross, Benjamin Dietrich, and Klaas P. Pruessmann. 2013. "Concurrent Magnetic Field Monitoring of EPI Time Series: Characterizing Encoding Field and Image Fluctuations Using Principal Component Analysis." In *Proceedings of the 21st Scientific Meeting, International Society for Magnetic Resonance in Medicine, Salt Lake City, USA*, 2715.

Krueger, S., T. Schaeffter, S. Weiss, K. Nehrke, T. Rozijn, and P. Boernert. 2006. "Prospective Intra-Image Compensation for Non-Periodic Rigid Body Motion Using Active Markers." In *Proceedings of the 14th Scientific Meeting, International Society for Magnetic Resonance in Medicine, Seattle, USA*, 3196. http://afni.nimh.nih.gov/sscc/staff/rwcox/ISMRM_2006/ISMRM%202006%20-%203340/files/03196.pdf.

Lauterbur, P. C. 1973. "Image Formation by Induced Local Interactions: Examples Employing Nuclear Magnetic Resonance." *Nature* 242 (5394): 190–91. doi:10.1038/242190a0.

Lee, Christine C., Roger C. Grimm, Armando Manduca, Joel P. Felmlee, Richard L. Ehman, Stephen J. Riederer, and Clifford R. Jack. 1998. "A Prospective Approach to Correct for Inter-Image Head Rotation in FMRI." *Magnetic Resonance in Medicine* 39 (2): 234–43. doi:10.1002/mrm.1910390210.

Lee, Christine C., Clifford R. Jack, Roger C. Grimm, Phillip J. Rossman, Joel P. Felmlee, Richard L. Ehman, and Stephen J. Riederer. 1996. "Real-Time Adaptive Motion

Correction in Functional MRI." *Magnetic Resonance in Medicine* 36 (3): 436–44. doi:10.1002/mrm.1910360316.

Ling, Josef, Flannery Merideth, Arvind Caprihan, Amanda Pena, Terri Teshiba, and Andrew R. Mayer. 2012. "Head Injury or Head Motion? Assessment and Quantification of Motion Artifacts in Diffusion Tensor Imaging Studies." *Human Brain Mapping* 33 (1): 50–62. doi:10.1002/hbm.21192.

Maclaren, Julian, Brian S R Armstrong, Robert T Barrows, K A Danishad, Thomas Ernst, Colin L Foster, Kazim Gumus, et al. 2012a. "Measurement and Correction of Microscopic Head Motion during Magnetic Resonance Imaging of the Brain." *PloS One* 7 (11): e48088. doi:10.1371/journal.pone.0048088.

Maclaren, Julian, Brian S. R. Armstrong, Robert T. Barrows, K. A. Danishad, Thomas Ernst, Colin L. Foster, Kazim Gumus, et al. 2012b. "Measurement and Correction of Microscopic Head Motion during Magnetic Resonance Imaging of the Brain." *PLoS ONE* 7 (11): e48088. doi:10.1371/journal.pone.0048088.

Man, Lai-Chee, John M. Pauly, and Albert Macovski. 1997. "Multifrequency Interpolation for Fast off-Resonance Correction." *Magnetic Resonance in Medicine* 37 (5): 785–92. doi:10.1002/mrm.1910370523.

Moriguchi, Hisamoto, and Jeffrey L. Duerk. 2006. "Bunched Phase Encoding (BPE): A New Fast Data Acquisition Method in MRI." *Magnetic Resonance in Medicine* 55 (3): 633–48. doi:10.1002/mrm.20819.

Nehrke, Kay, and Peter Börnert. 2005. "Prospective Correction of Affine Motion for Arbitrary MR Sequences on a Clinical Scanner." *Magnetic Resonance in Medicine* 54 (5): 1130–38. doi:10.1002/mrm.20686.

Odille, Freddy, Sergio Uribe, Philip G. Batchelor, Claudia Prieto, Tobias Schaeffter, and David Atkinson. 2010. "Model-Based Reconstruction for Cardiac Cine MRI without ECG or Breath Holding." *Magnetic Resonance in Medicine* 63 (5): 1247–57. doi:10.1002/mrm.22312.

Odille, Freddy, Pierre-André Vuissoz, Pierre-Yves Marie, and Jacques Felblinger. 2008. "Generalized Reconstruction by Inversion of Coupled Systems (GRICS) Applied to Free-Breathing MRI." *Magnetic Resonance in Medicine* 60 (1): 146–57. doi:10.1002/mrm.21623.

Ooi, M. B., S. Krueger, W. J. Thomas, S. V. Swaminathan, and T. R. Brown. 2009. "Prospective Real-Time Correction for Arbitrary Head Motion Using Active Markers." *Magnetic Resonance in Medicine* 62 (4): 943–54.

Ooi, Melvyn B., Sascha Krueger, Jordan Muraskin, William J. Thomas, and Truman R. Brown. 2011. "Echo-Planar Imaging with Prospective Slice-by-Slice Motion Correction Using Active Markers." *Magnetic Resonance in Medicine* 66 (1): 73–81. doi:10.1002/mrm.22780.

Papoulis, A. 1977. "Generalized Sampling Expansion." *IEEE Transactions on Circuits and Systems* 24 (11): 652–54. doi:10.1109/TCS.1977.1084284.

Pruessmann, Klaas P., Markus Weiger, Peter Boernert, and Peter Boesiger. 2001. "Advances in Sensitivity Encoding with Arbitrary K-Space Trajectories." *Magnetic Resonance in Medicine* 46 (4): 638–51. doi:10.1002/mrm.1241.

Pruessmann, Klaas P., Markus Weiger, Markus B. Scheidegger, and Peter Boesiger. 1999. "SENSE: Sensitivity Encoding for Fast MRI." *Magnetic Resonance in Medicine* 42 (5): 952–62. doi:10.1002/(SICI)1522-2594(199911)42:5<952::AID-MRM16>3.0.CO;2-S.

Purcell, E. M., H. C. Torrey, and R. V. Pound. 1946. "Resonance Absorption by Nuclear Magnetic Moments in a Solid." *Physical Review* 69 (1-2): 37–38. doi:10.1103/PhysRev.69.37.

Rabi, I. I. 1937. "Space Quantization in a Gyrating Magnetic Field." *Physical Review* 51 (8): 652–54. doi:10.1103/PhysRev.51.652.

Ries, Mario, Baudouin Denis de Senneville, Sébastien Roujol, Yasmina Berber, Bruno Quesson, and Chrit Moonen. 2010. "Real-Time 3D Target Tracking in MRI Guided Focused Ultrasound Ablations in Moving Tissues." *Magnetic Resonance in Medicine* 64 (6): 1704–12. doi:10.1002/mrm.22548.

Schmidt, Johannes F. M., Martin Buehrer, Peter Boesiger, and Sebastian Kozerke. 2011. "Nonrigid Retrospective Respiratory Motion Correction in Whole-Heart Coronary MRA." *Magnetic Resonance in Medicine* 66 (6): 1541–49. doi:10.1002/mrm.22939.

Schulz, Jessica, Thomas Siegert, Enrico Reimer, Christian Labadie, Julian Maclaren, Michael Herbst, Maxim Zaitsev, and Robert Turner. 2012. "An Embedded Optical Tracking System for Motion-Corrected Magnetic Resonance Imaging at 7T." *Magnetic Resonance Materials in Physics, Biology and Medicine* 25 (6): 443–53. doi:10.1007/s10334-012-0320-0.

Schulz, J., T. Siegert, P. -L. Bazin, J. Maclaren, M. Herbst, M. Zaitsev, and R. Turner. 2014. "Prospective Slice-by-Slice Motion Correction Reduces False Positive Activations in fMRI with Task-Correlated Motion." *NeuroImage* 84 (January): 124–32. doi:10.1016/j.neuroimage.2013.08.006.

Seto, E., G. Sela, W.E. McIlroy, S.E. Black, W.R. Staines, M.J. Bronskill, A.R. McIntosh, and S.J. Graham. 2001. "Quantifying Head Motion Associated with Motor Tasks Used in fMRI." *NeuroImage* 14 (2): 284–97. doi:10.1006/nimg.2001.0829.

Smink, Jouke, Marko Häkkinen, Ronald Holthuizen, Sascha Krueger, Mario Ries, Yasmina Berber, Moonen Chrit, Max Köhler, and Vahala Erkki. 2011. "eXTernal Control (XTC): A Flexible, Real-Time, Low-Latency, Bi-Directional Scanner Interface." In *Proceedings of the 19th Scientific Meeting, International Society for Magnetic Resonance in Medicine, Montreal, Canada*, 1755.

Sodickson, Daniel K., and Warren J. Manning. 1997. "Simultaneous Acquisition of Spatial Harmonics (SMASH): Fast Imaging with Radiofrequency Coil Arrays." *Magnetic Resonance in Medicine* 38 (4): 591–603. doi:10.1002/mrm.1910380414.

Speck, O., J. Hennig, and M. Zaitsev. 2006. "Prospective Real-Time Slice-by-Slice Motion Correction for fMRI in Freely Moving Subjects." *Magnetic Resonance Materials in Physics, Biology and Medicine* 19 (2): 55–61. doi:10.1007/s10334-006-0027-1.

Stockmann, Jason P., Pelin Aksit Ciris, Gigi Galiana, Leo Tam, and R. Todd Constable. 2010. "O-Space Imaging: Highly Efficient Parallel Imaging Using Second-Order Nonlinear Fields as Encoding Gradients with No Phase Encoding." *Magnetic Resonance in Medicine* 64 (2): 447–56. doi:10.1002/mrm.22425.

Tan, Hao, and Craig H. Meyer. 2009. "Estimation of K-Space Trajectories in Spiral MRI." *Magnetic Resonance in Medicine* 61 (6): 1396–1404. doi:10.1002/mrm.21813.

Thesen, Stefan, Oliver Heid, Edgar Mueller, and Lothar R. Schad. 2000. "Prospective Acquisition Correction for Head Motion with Image-Based Tracking for Real-Time fMRI." *Magnetic Resonance in Medicine* 44 (3): 457–65. doi:10.1002/1522-2594(200009)44:3<457::AID-MRM17>3.0.CO;2-R.

Tisdall, M. Dylan, Aaron T. Hess, Martin Reuter, Ernesta M. Meintjes, Bruce Fischl, and André J. W. van der Kouwe. 2012. "Volumetric Navigators for Prospective Motion Correction and Selective Reacquisition in Neuroanatomical MRI." *Magnetic Resonance in Medicine* 68 (2): 389–99. doi:10.1002/mrm.23228.

Uecker, Martin, Peng Lai, Mark J. Murphy, Patrick Virtue, Michael Elad, John M. Pauly, Shreyas S. Vasanawala, and Michael Lustig. 2014. "ESPIRiT—an Eigenvalue Approach to Autocalibrating Parallel MRI: Where SENSE Meets GRAPPA." *Magnetic Resonance in Medicine* 71 (3): 990–1001. doi:10.1002/mrm.24751.

Umeyama, Shinji. 1991. "Least-Squares Estimation of Transform Parameters Between Two Point Patterns" 13 (4): 376–80.

Van de Moortele, Pierre-François, Josef Pfeuffer, Gary H. Glover, Kamil Ugurbil, and Xiaoping Hu. 2002. "Respiration-Induced B0 Fluctuations and Their Spatial Distribution in the Human Brain at 7 Tesla." *Magnetic Resonance in Medicine* 47 (5): 888–95. doi:10.1002/mrm.10145.

Van der Kouwe, André J.W., Thomas Benner, and Anders M. Dale. 2006. "Real-Time Rigid Body Motion Correction and Shimming Using Cloverleaf Navigators." *Magnetic Resonance in Medicine* 56 (5): 1019–32. doi:10.1002/mrm.21038.

Vannesjo, Signe J., Maximilan Haeberlin, Lars Kasper, Matteo Pavan, Bertram J. Wilm, Christoph Barmet, and Klaas P. Pruessmann. 2013. "Gradient System Characterization by Impulse Response Measurements with a Dynamic Field Camera." *Magnetic Resonance in Medicine* 69 (2): 583–93. doi:10.1002/mrm.24263.

Vannesjo, Signe Johanna, Christoph Barmet, Yolanda Duerst, Simon Gross, David Brunner, and Klaas P. Pruessmann. 2012. "Higher-Order Monitoring of Physiological Field Fluctuations in Brain MRI at 7T." In *Proceedings of the 20th Scientific Meeting, International Society for Magnetic Resonance in Medicine, Melbourne, Australia*, 216. Melbourne, Australia.

Vannesjo, Signe Johanna, Benjamin E. Dietrich, Christoph Barmet, Bertram J. Wilm, David O. Brunner, and Klaas P. Pruessmann. 2012. "Measurement and Pre-Emphasis of Shim Responses Using Frequency Sweeps." In *Proceedings of the 20th Scientific Meeting, International Society for Magnetic Resonance in Medicine, Melbourne, Australia*, 142.

Vannesjo, S. Johanna, Benjamin E. Dietrich, Matteo Pavan, David O. Brunner, Bertram J. Wilm, Christoph Barmet, and Klaas P. Pruessmann. 2014. "Field Camera Measurements of Gradient and Shim Impulse Responses Using Frequency Sweeps: Gradient and Shim Characterization Using Frequency Sweeps." *Magnetic Resonance in Medicine* 72 (2): 570–83. doi:10.1002/mrm.24934.

Vannesjo, S. Johanna, Bertram J. Wilm, Yolanda Duerst, Simon Gross, David O. Brunner, Benjamin E. Dietrich, Thomas Schmid, Christoph Barmet, and Klaas P. Pruessmann. 2014. "Retrospective Correction of Physiological Field Fluctuations in High-Field Brain MRI Using Concurrent Field Monitoring." *Magnetic Resonance in Medicine*, June, n/a – n/a. doi:10.1002/mrm.25303.

Versluis, M.J., J.M. Peeters, S. van Rooden, J. van der Grond, M.A. van Buchem, A.G. Webb, and M.J.P. van Osch. 2010. "Origin and Reduction of Motion and f0 Artifacts in High Resolution T2*-Weighted Magnetic Resonance Imaging: Application in Alzheimer's Disease Patients." *NeuroImage* 51 (3): 1082–88. doi:10.1016/j.neuroimage.2010.03.048.

Welch, E. B., A. Manduca, R. C. Grimm, H. A. Ward, and C. R. Jack Jr. 2001. "Spherical Navigator Echoes for Full 3D Rigid Body Motion Measurement in MRI." *Magnetic Resonance in Medicine* 47 (1): 32–41.

White, Nathan, Cooper Roddey, Ajit Shankaranarayanan, Eric Han, Dan Rettmann, Juan Santos, Josh Kuperman, and Anders Dale. 2010. "PROMO: Real-Time Prospective Motion Correction in MRI Using Image-Based Tracking." *Magnetic Resonance in Medicine* 63 (1): 91–105. doi:10.1002/mrm.22176.

Wilm, Bertram J., Christoph Barmet, Matteo Pavan, and Klaas P. Pruessmann. 2011. "Higher Order Reconstruction for MRI in the Presence of Spatiotemporal Field Perturbations." *Magnetic Resonance in Medicine* 65 (6): 1690–1701. doi:10.1002/mrm.22767.

Wilm, Bertram J., Yolanda Duerst, Benjamin E. Dietrich, Michael Wyss, S. Johanna Vannesjo, Thomas Schmid, David O. Brunner, Christoph Barmet, and Klaas P. Pruessmann. 2014. "Feedback Field Control Improves Linewidths in in Vivo Magnetic Resonance Spectroscopy." *Magnetic Resonance in Medicine* 71 (5): 1657–62. doi:10.1002/mrm.24836.

Yarach, Uten, Chaiya Luengviriya, Appu Danishad, Daniel Stucht, Frank Godenschweger, Peter Schulze, and Oliver Speck. 2014. "Correction of Gradient Nonlinearity Artifacts in

Prospective Motion Correction for 7T MRI." *Magnetic Resonance in Medicine*, April, n/a – n/a. doi:10.1002/mrm.25283.

Ying, Leslie, and Jinhua Sheng. 2007. "Joint Image Reconstruction and Sensitivity Estimation in SENSE (JSENSE)." *Magnetic Resonance in Medicine* 57 (6): 1196–1202. doi:10.1002/mrm.21245.

Zaitsev, M., C. Dold, G. Sakas, J. Hennig, and O. Speck. 2006. "Magnetic Resonance Imaging of Freely Moving Objects: Prospective Real-Time Motion Correction Using an External Optical Motion Tracking System." *NeuroImage* 31 (3): 1038–50. doi:10.1016/j.neuroimage.2006.01.039.

Zaitsev, M., J. Hennig, and O. Speck. 2004. "Point Spread Function Mapping with Parallel Imaging Techniques and High Acceleration Factors: Fast, Robust, and Flexible Method for Echo-Planar Imaging Distortion Correction." *Magnetic Resonance in Medicine* 52 (5): 1156–66. doi:10.1002/mrm.20261.

Acknowledgements

This thesis is the result of six years of research at the Institute of Biomedical Engineering at ETH Zurich. In this unique period of my life, many people have supported me. My thanks go to:

Prof. Dr. Klaas Pruessmann for his committed supervision, his mentorship and guidance, and for creating a unique research environment full of scientific vision, rigor, freedom and a balancing amount of fun diversion. I'm particularly indebted to him for letting me shift the focus of my thesis to motion correction, which had not been intended in the beginning.

Prof. Dr. Oliver Speck for co-refereeing this thesis.

Dr. Christoph Barmet for his enthusiastic introduction to MRI, and many good laughs. He guided me during my first steps in MRI and it was him who sparked my love for this subject. He was heavily involved in getting the motion correction running and designed the field probes that enabled it all. He has influenced my thinking not only on MR but also on many other aspects of life.

My two closest collaborators, Dr. S. Johanna Vannesjo and Dr. Lars Kasper. Starting our PhDs 'concurrently' made it really exciting to tackle the first problems that came along. I learned a lot from both of them in countless discussions on MR image reconstruction, field monitoring, physics, medicine, neuroscience, and life. Over an extended period of my PhD, Lars was a great comrade during long, tedious scan sessions with an unparalleled, long, and hard sense of humor, and a unique wit and talent for comedy. Johanna was a solid reference for many of my various questions on medicine, biology, and life. She set a good example on how to manage a thesis project.

Dr. David Brunner and Dr. Bertram Wilm. Bertram was heavily involved in getting the field monitoring projects going in the beginning. I particularly benefitted from his exceptional pulse programming and image reconstruction skills. David devised the original idea of using gradient tones that focused my thesis to what has been written down in here.

Simon Gross and Benjamin Dietrich. They developed much of the hardware that enabled all experiments and were always very helpful when fixes were necessary. I have also spent many great moments with them joking and drinking.

The PhD students at IBT with whom I shared so many great moments in the past six years.

The students whose Master's Theses I supervised: George Batsios, Jonathan Richner, and Sascha Aranovitch. Sascha's project was particularly fruitful and culminated in one of the chapters of this thesis.

Matthieu Guerquin-Kern, my NCCBI fellow and friend from EPF Lausanne. We had a fruitful collaboration and many discussions on image reconstruction. He is the only one I've ever scanned with who insisted on combining that with wine and cheese dinners.

The IBT staff that enable very good working conditions: Marianne Berg and Bruno Willi.

Stephen Wheeler for his expert support on building the head setups and other mechanical parts I needed for the experiments.

Giel Mens for his sharing his pulse programming expertise that greatly sped up the technological development.

My parents, for their unconditional support throughout my entire life. Together with my brothers they are my family and provide me the stability I draw everything from in my life.

Susana. You mean everything to me.

List of Publications

Peer-reviewed Journal Articles

1. S.J. Vannesjo, M. Haeberlin, L. Kasper, M. Pavan, B.J. Wilm, C. Barmet and K.P. Pruessmann (2013). Gradient system characterization by impulse response measurements with a dynamic field camera. Magnetic Resonance in Medicine 69(2):583-93.

2. D. Giese, M. Haeberlin, Ch. Barmet, K.P. Pruessmann, T. Schaeffter, and S. Kozerke (2012). Analysis and Correction of Background Velocity Offsets in Phase-Contrast Flow Measurements Using Magnetic Field Monitoring. Magnetic Resonance in Medicine 67(5):1294-302.

3. M. Guerquin-Kern, M. Häberlin, K.P. Pruessmann, M. Unser (2011). A Fast Wavelet-Based Reconstruction Method for Magnetic Resonance Imaging. IEEE Transactions on Medical Imaging, vol. 30, no. 9, pp. 1649-1660.

4. M. Haeberlin, L. Kasper, C. Barmet, D. O. Brunner, B. E. Dietrich, S. Gross, B. J. Wilm, S. Kozerke, K. P. Pruessmann. Real-time motion correction using gradient tones and head-mounted NMR field probes. Magn Reson Med. doi: 10.1002/mrm.25432.

5. Kasper, L., Bollmann, S., Vannesjo, S. J., Gross, S., Haeberlin, M., Dietrich, B. E. and Pruessmann, K. P. (2014), Monitoring, analysis, and correction of magnetic field fluctuations in echo planar imaging time series. Magn Reson Med. doi: 10.1002/mrm.25407

Abstracts/Conference Proceedings

1. S.J. Vannesjoe, M. Haeberlin, L. Kasper, C. Barmet and K.P. Pruessmann, Measurement of gradient impulse response functions using a 3rd-order dynamic field camera. Proceedings ESMRMB, Antalya (2009).

2. S.J. Vannesjoe, M. Haeberlin, L. Kasper, C. Barmet and K.P. Pruessmann, A method for characterizing the magnetic field response of a gradient system. Proceedings ISMRM, Stockholm (2010).

3. D. Giese, M. Haeberlin, C. Barmet, T. Schaeffter and K. P. Pruessmann and S. Kozerke, Analysis and correction of background velocity offsets in cine phase-contrast imaging using magnetic field monitoring. Proceedings ISMRM, Stockholm (2010).

4. L. Kasper, S.J. Vannesjoe, M. Haeberlin, C. Barmet, K. E. Stephan and K. P. Pruessmann, Non-uniform density EPI acquisition improves the SNR of smoothed MR images. Proceedings ISMRM, Stockholm (2010).

5. M. Haeberlin, B. Wilm, C. Barmet, S. Kozerke, G. Katsikatsos and K.P. Pruessmann, Sinusoidal Perturbations Improve the Noise Behavior of Parallel EPI. Proceedings ISMRM, Stockholm (2010).

6. M. Haeberlin, L. Kasper, C. Barmet, S.J. Vannesjö, S. Kozerke and K.P. Pruessmann, Combined Real-Time Prospective Motion Correction and Concurrent Field Monitoring. Proceedings ISMRM Montreal (2011).

7. L. Kasper, M. Haeberlin, C. Barmet, B. J. Wilm, C. C. Ruff, K. E. Stephan and K.P. Prüssmann, Matched Filter EPI Increases BOLD-Sensitivity in Human Functional MRIProceedings ISMRM Montreal (2011).

8. B. J. Wilm, C. Barmet, M. Guerquin-Kern, M. Haeberlin and K. P. Pruessmann, Single-Shot Partial-Fourier Spiral Imaging. Proceedings ISMRM Montreal (2011).

9. M. Haeberlin, D.O. Brunner, L. Kasper, Ch. Barmet and K.P.Pruessmann, Continuous Motion Tracking and Correction Using NMR Probes and Gradient Tones. Proceedings ISMRM Melbourne (2012).

10. L. Kasper, M. Haeberlin, B.J. Wilm, K.E. Stephan, K.P. Pruessmann, 2D Matched Filter Acquisition for Improved SNR in Routine Brain Imaging. Proceedings ISMRM Melbourne (2012).

11. B.J. Wilm, Ch. Barmet, L. Kasper, M. Haeberlin, B.E. Dietrich, K.P. Pruessmann, Partial Fourier Accelerated Spiral SENSE Imaging Using Magnetic Field Monitoring, Proceedings ISMRM Melbourne (2012).

12. Lars Kasper, Maximilian Haeberlin, Benjamin E. Dietrich, Simon Gross, Christoph Barmet, Christian C. Ruff, Klaas E. Stephan, and Klaas P. Pruessmann, Analysis of BOLD Sensitivity in Matched Filter fMRI. Proceedings ISMRM Salt Lake City (2013).

13. Field Decoupling for Real-Time Prospective Motion Correction Using Gradient Tones and Concurrent Field Monitoring, Haeberlin, Maximilian; Kasper, Lars; Barmet, Christoph; Brunner, David Otto; Pruessmann, Klaas P., Proceedings ISMRM Salt Lake City (2013).

14. Motion Correction of EPI sequences using their intrinsic high-frequency content, Haeberlin, Maximilian; Aranovitch, Alexander ; Kasper, Lars; Barmet, Christoph; Pruessmann, Klaas P., Proceedings ISMRM Milan (2014).

15. Correction of fast motion by field monitoring in the head frame of reference, Aranovitch, Alexander; Haeberlin, Maximilian; Kasper, Lars; Barmet, Christoph; Pruessmann, Klaas P., Proceedings ISMRM Milan (2014).

16. Physiological and system-induced field fluctuations in EPI time series in vivo, Klein , Saskia; Kasper, Lars; Vannesjoe, Johanna; Gross, Simon; Dietrich, Benjamin; Barmet, Christoph; Haeberlin, Maximilian; Brunner, David; Wilm, Bertram; Pruessmann, Klaas P., Proceedings ISMRM Milan (2014).

Curriculum Vitae

Maximilian Rudolf Gottfried Häberlin, born April 5, 1983.

2008 – 2014   Scientific Assistant and PhD Candidate
Institute for Biomedical Engineering, University of Zurich and ETH Zurich.
Advisor: Prof. Dr. Klaas P. Pruessmann.

October 2008   Master's Degree (MSc. ITET ETH) at ETH Zurich.

2007 – 2008   Master's Thesis
Department of Radiology, Stanford University, Palo Alto, California.
Advisor: Prof. Dr. Roland Bammer.
Thesis Title: *Matrix Representation and Tikhonov Regularization of HYPR Reconstruction.*

2002 – 2007   Studies in Information Technology and Electrical Engineering at ETH Zurich.
Focus in Biomedical Engineering.

1998 – 2002   High School in Kreuzlingen. Major subject: Italian.

1996 – 1998   Secondary School in Kreuzlingen.